UNIVERSITY OF CALIFORNIA
SANTA CRUZ

THE EFFECT OF BAROCLINIC PROCESSES ON MARINE PRIMARY PRODUCTION

A dissertation submitted in partial satisfaction of the
requirements for the degree of

DOCTOR OF PHILOSOPHY

in

OCEAN SCIENCES

by

Jasen Robert Jacobsen

December 2024

The Dissertation of Jasen Robert Jacobsen
is approved:

Christopher A. Edwards, Chair

Brian S. Powell

Jerome Fiechter

John A. Colosi

Peter F. Biehl
Vice Provost and Dean of Graduate Studies

Table of Contents

List of Figures

List of Tables

Abstract

The Effect of Baroclinic Processes on Marine Primary Production

by

Jasen Robert Jacobsen

The base of the marine ecosystem is supported by marine microalgae known as phytoplankton. Phytoplankton rely on the combination of light and nutrients to survive. Plankton and nutrients move with water parcels, and fluid motion dictates the light environment essential to most primary production. In geophysical systems, fluid motion is often described as barotropic or baroclinic. Barotropic motion corresponds to the depth-averaged flow, and is largely independent of stratification. When lateral changes in density occur in a stratified fluid, motion deviates from the depth depth-averaged flow and is referred to as baroclinic motion. Many different types of baroclinic processes exist in the ocean, each one affecting light and nutrient availability for primary production. This dissertation uses idealized numerical models to explore three different baroclinic systems and how each affects light and nutrient availability for primary production in the ocean.

Chapter One investigates the primary production response to the generation of internal tides by fluctuating tidal flow over varying bathymetry. This process concentrates baroclinic wave energy into a coherent structure known as a tidal beam. The tidal beam leads to a large displacement of phytoplankton through a light field that varies exponentially with depth, leading to more light available for primary production.

At the same time, the tidal beam elevates the average position of isopycnal surfaces, carrying nutrients and phytoplankton into the euphotic zone. Analysis of Lagrangian parcels that move with ocean currents and representing phytoplankton shows that the effect on nutrient availability enhances primary production more than the increase in light.

Chapter Two turns to a different type of baroclinic wave known as an Island Trapped Wave (ITW). ITWs are analogous to coastal trapped waves where an island acts as a waveguide boundary. In the case considered here, an ITW that travels around the island in a 24-hour period is excited as a resonant response to a land-sea breeze with a 24-hour period. As part of the resonant response, ITWs affect light and nutrient availability for primary production. Nonlinear processes associated with the ITW increase nutrient concentrations in the euphotic zone through elevated advective and diffusive flux divergences. With regard to light availability, a diel light cycle causes a dipole structure of primary production across the island with the largest enhancement of primary production occurring where the upwelling phase of the ITW arrives at noon. To quantify this effect, phytoplankton biomass, nutrient, and light are decomposed into their mean states and fluctuations around their means. Primary production associated with the mean state is the larger, indicating that the enhancement of primary production occurs due to state adjustment of the nutrient field rather than light fluctuations. However, the correlation of light and nutrient fluctuations further increases this enhancement by an additional 30%.

Chapter Three considers yet another baroclinic process, wind-driven coastal

upwelling, and compares the primary production response in two- and three-dimensional idealized numerical models. Coastal upwelling is driven by offshore surface Ekman transport which removes surface water from the coast and replaces it with nutrient-rich waters from below, often causing large phytoplankton blooms. The depth of the upwelled water determines the nutrient content, with deeper waters having higher nutrient concentrations. The geometry of the continental shelf affects the upwelling source depth and thus magnitude of the primary production response. Two-dimensional upwelling theory and numerical modeling studies predict that steeper shelves source water from deeper depths compared to wider shelves. In three-dimensions, changes in alongshore shelf width also adjust upwelling source depth. Deeper, higher nutrient water is transported cross-shelf with the bottom boundary when a shelf widens in the downwind direction. Results from this chapter show that the primary production response is laterally displaced downstream from bottom boundary layer transport by alongshore transport. Primary production is elevated up to 100 km downwind of the change in shelf width after ten days of upwelling. Conversely, where the shelf narrows in the direction of the wind, the reduced transport along the bottom boundary causes less nutrients to be delivered to the euphotic zone and lower levels of primary production. In both cases, changes in shelf width in the alongshore direction locally affect upwelling source depth, and the resulting elevated or diminished nutrient concentrations are then delivered to the euphotic zone downwind of the change in shelf width.

In summary, this dissertation examines how baroclinic processes affect light and nutrient availability differently depending on the context of the generating mecha-

nism. These baroclinic processes primarily affect phytoplankton growth through vertical nutrient transport; however, some processes can affect light availability as well, highlighting the diversity of biological responses to baroclinic motion.

This thesis is dedicated to my grandfather,

Robert F. Hornbeck.

Thank you for inspiring me to be always curious about the natural world.

Acknowledgments

I want to thank my committee, who provided invaluable insight throughout my time a UC Santa Cruz.

I also want to thank my collaborators Žarko Kovač, Hrvoje Mihanović, and Zrinka Ljubešić for their guidance and support.

Chapter 1

Introduction

In every ecosystem, whether terrestrial or marine, the level of primary production establishes the baseline growth level that supports all other organisms within that ecosystem. In the ocean, marine microalgae, or phytoplankton, perform primary production by harvesting light and nutrients to synthesize energy in order to maintain their cellular processes, grow, and reproduce. In marine environments, photosynthetic primary production by phytoplankton only occurs in the well-lit region near the ocean's surface, known as the euphotic zone. However, due to the abundance of light, phytoplankton readily deplete nutrients to levels where nutrients limit phytoplankton growth. Because most phytoplankton cannot adjust their position in the water column, physical processes determine their vertical position, controlling the levels of light and nutrients available for survival and growth. This dissertation uses idealized numerical simulations to study physical processes that affect photosynthetic primary production by adjusting light and nutrient availability to phytoplankton within the euphotic zone.

In the ocean, the scales of physical processes range from global circulation patterns, that occur from thousand-year time scales to millimeter-scale turbulence with time scales of less than a second. In order to resolve the connection between resource availability and primary production, the physical process scale must align with the biological scale. Phytoplankton have doubling times on the order of hours to days, depending on their size and type as well as their associated nutrient and light harvesting rates. Aiming to study how physical processes in the ocean affect phytoplankton growth, this work focuses on processes with time scales on the order of hours to several days with spatial scales between tens of meters and less than one hundred kilometers.

Processes that control light and nutrient availability vary widely throughout the ocean. In the Atlantic subtropical gyre, the depth and duration of winter mixing determine the primary production level in the following spring [107, 113]. Stronger winter mixing elevates the amount of nutrients in the upper water column, and then as the season transitions into spring and light no longer limits primary production, large phytoplankton blooms occur [81]. In the subpolar gyre, where the season transitions from months without sun in winter, to sustained sunlight in summer, primary production follows suit with large phytoplankton blooms beginning in spring, peaking during maximum insolation, and a complete cessation of primary production in winter [100]. Near the equator, persistent eastward winds drive vertical motion in the underlying ocean which supplies a low, but consistent supply of nutrients, supporting year-round primary production. However, changes in the strength of equatorial winds can affect nutrient delivery, leading to variations in primary production levels [40].

On smaller spatial scales, horizontal convergences and divergences near the ocaen surface result in vertical motion that can move nutrients into or out-of the well-lit euphotic zone where primary production can occur [89]. Some examples of these features include fronts, where two or more water masses converge, and rotational features like slightly dissipative eddies [17, 51]. In each of these cases, vertical velocities adjust light and nutrient availability for phytoplankton, changing the local level of primary production.

Chlorophyll-a measurements are commonly used to approximate the distribution of phytoplankton, but it can be challenging to determine whether changes in fluorescence reflect changes in phytoplankton biomass or an adjustment of the amount of chlorophyll pigment within each cell [22]. In the vertical direction, observations show that the largest chlorophyll-a measurements are not found at the surface, but rather reach a maximum value between 50 m and 125 m depth, depending on location and time of year [20]. This phenomenon is a global feature known as the Deep Chlorophyll Maxima (DCM). The mechanisms which support the formation and maintenance of the DCM vary widely throughout the global ocean [22]. In a recent synthesis of global observations, Cornec et al., (2021) examined available data to establish the seasonality and spatial distribution of DCM [20]. As part of their work, they defined locations where the DCM comprised changes in biomass or changes in pigment. They discovered that locations where the DCM was associated with elevated pigment were regions where nutrient supply was low. In contrast, they found that where the DCM was associated increases in biomass, both light and nutrients were favorable for primary production,

leading to the open question: what environmental drivers create favorable light and nutrient conditions that support elevated biomass within the DCM?

Several studies have examined potential mechanisms that support primary production within the DCM. The vertical displacement of phytoplankton through the exponentially varying light field enhance light availability for primary production [20, 22, 30, 37, 44, 59]. One example is a study by Evans et al., (2008) who used field experiments and mathematical models to show that light variability, whether from changes in surface irradiance or displacement through the water column, results in up to 200% enhancement of primary production. More recently, Freilich and Mahadevan (2019) investigated mechanisms that carry nutrients into the euphotic zone [33]. Their idea was to decompose nutrient transport into a supply by isopycnals experiencing uplift or via nutrient transport along isopycnal surfaces. They found that uplift supplies the majority of nutrients to the upper ocean while along isopycnal flux contributes between 10% and 25% of nutrient delivery. However, along isopycnal nutrient flux becomes increasingly important for smaller horizontal scales. This dissertation aims to add to these examples by studying specific physical processes that lead to a favorable combination of light and nutrients which support increases in phytoplankton biomass.

Depending on the tools and measurements used, there are many ways to define primary production. The numerical simulations discussed in this work use a nitrogen-based ecosystem model which, in an Eulerian reference frame, defines primary production as,

$$PP = P(t)\frac{V_m N(t)}{K_s + N(t)}\frac{I(t)}{I_0}e^{k_{ext}z} \tag{1.1}$$

where the parameters V_m, K_s, and k_{ext} are the maximum uptake rate, the half-saturation constant, and the light attenuation coefficient, respectively. The variable $P(t)$ is phytoplankton biomass and the variable $N(t)$ is nutrient concentration. The depth, z, and the surface light intensity, $I(t)$, normalized by daily average light I_0, control light availability for primary production. In this form, primary production is in units of millimoles of nitrogen per cubic meter fixed into biomass per day, and changes in primary production are due to variability of biomass, nutrients, and light.

When considering how physical processes affect primary production, it is often useful to consider how the fluid shapes an individual phytoplankter's light and nutrient environment. For a Lagrangian algal cell that follows the current, primary production in equation 1.1 can be normalized by biomass to express it as simply as a rate per unit phytoplankton,

$$\frac{PP}{P} = \underbrace{\frac{V_m N(t)}{K_s + N(t)}}_{\text{Nutrient Control}}\ \underbrace{\frac{I(t)}{I_0}e^{k_{ext}z(t)}}_{\text{Light Control}}. \tag{1.2}$$

Light availability is now a function of time-varying depth, $z(t)$, which can be affected by fluid motion. In this form, the physical process that controls nutrient availability, $N(t)$ is a diffusive flux divergence, and the phytoplankter's vertical position, combined with surface irradiance, determines the primary production level.

Vertical motion governs the availability of light and nutrients for primary pro-

duction. Geophysical flows are often described as barotropic or baroclinic. Barotropic motion occurs when the pressure remains constant on surfaces of constant density. In this scenario, flow throughout the water column remains coupled to the depth-averaged current. In contrast, baroclinic motion arises when stratification and horizontal variations in density are present. This leads to a situation where horizontal pressure is no longer constant on surfaces of constant density, resulting in horizontal pressure gradients that change with depth. Consequently, horizontal motions deviate from their depth-average. As an example, consider a two-dimensional fluid system that is stratified into two layers separated by an interface between rarer (less dense) fluid overlaying higher density fluid. In the case of barotropic motion, the movement is unrelated to the interface between the upper and lower layers, meaning the motion does not affect the position of the interface. For baroclinic motion, horizontal variations in the pressure gradient with depth cause motion in the upper and lower layers to move separately from one another and from the depth-averaged current. In this scenario, the position of the interface can change in time, resulting in a dynamic adjustment of the thickness of the upper and lower layers.

For an algal particle, barotropic and baroclinic motions adjust the availability of light and nutrients for primary production in different ways. Excluding the stationary case, barotropic motion affects the vertical position of an algal particle in the water column, moving it up and down through a light field that changes exponentially with depth, leading to increases the average amount of light available for primary production without net vertical transport. However, this movement occurs only by a very small

amount related to fluctuations of the free surface. Furthermore, net vertical movement of nutrients only results from diffusion. As a result, barotropic motion has a minimal effect on both light and nutrient availability for primary production.

In the case of baroclinic motion, upper and lower layers move separately, often affecting both nutrient and light availability for primary production. For instance, upwelling of the lower layer moves nutrients vertically upward, increasing their concentration in the euphotic zone and typically enhancing primary production. Conversely, downwelling of the lower layer and the associated expansion of the upper layer can transport algal particles and typically low nutrient concentrations into deeper waters. This process reduces light and nutrient availability and can decrease primary production. Baroclinic processes adjust both the availability of light and nutrients, which can act to either enhance or suppress primary production. However, a wide range of baroclinic processes exist in the ocean. The generating mechanism and structure of the baroclinicity influence how a process affects the nutrient field and how an algal cell experiences the light environment. To that end, investigating the relationship between baroclinic processes and primary production requires individual attention to the nature of the process and subsequent adjustment of resource availability for primary production.

We can improve predictions on how relatively small-scale processes affect global-scale primary production by investigating relationships between baroclinic motion and primary production in idealized settings. With the improved understanding of the relationship between resource availability for primary production and the physical environment presented in this work, we have a clearer understanding of the processes that

control the background level of marine primary production that is often unresolved by course-resolution global climate simulations. The insights presented here may lay the groundwork to improve our predictions of how marine ecosystems will respond to a rapidly warming world.

This dissertation uses idealized numerical models to examine how specific baroclinic processes affect nutrient and light availability for primary production. Chapter 2 examines how the generation of internal tides by flow over sloping bathymetry increases primary production in the overlaying waters. Chapter 3 looks at a different baroclinic wave known as an island trapped waves and diagnoses how it modulates primary production through adjustments of the light and nutrient fields. Then, Chapter 4 turns to a third baroclinic process, coastal upwelling, and compares how nutrient sources to the euphotic zone are affected by wind-driven flow around a submarine bank. Finally, this dissertation concludes with a brief summary and discussion of possible future research directions for each chapter.

Chapter 2

Nutricline Adjustment by Internal Tidal Beam Generation Enhances Primary Production in Idealized Numerical Models

2.1 Abstract

When the barotropic tide encounters variable bathymetry, fluctuating flow along a topographic slope generates baroclinic tides, or internal tides. There is growing evidence that these internal tides can affect primary production in the euphotic zone, though the dominant mechanisms are unclear. Internal tides move passive phytoplankton through an exponentially varying light field, enhancing primary production near the base of the euphotic zone. In addition internal tides also increase primary production through

vertical nutrient advection into the euphotic zone. Topographically generated internal tides can be separated into two regimes: 1) the often highly nonlinear near-field regime where tidal beams are observed and 2) the more linear far-field regime. This study examines the primary production response to these internal tide processes using the Regional Ocean Modeling System (ROMS) coupled to a simple Nutrient, Phytoplankton, Zooplankton, Detritus (NPZD) model. These idealized simulations generate internal tide beams with an oscillating, horizontal body force at the M_2 tidal frequency that is applied to domains with a bathymetric step and uniform stratification. Sensitivity of the primary production response to the energy content of the tidal beam is obtained by adjusting the height and slope of the bathymetric step. Simulation results reveal that primary production intensifies along tidal beams due to nonlinear enhancement of parcel vertical displacement (light effect) and nutrient advective flux divergence (nutrient effect). In the near-field regime across the range of step heights and slopes in this study, the nutrient effect is an order of magnitude larger and explains 92% of the variance in primary production versus only 14% for the light effect. The nutrient effect on primary production is determined by the energy content of the beam set by the geometry of the generating feature. The light effect is limited in the euphotic zone across all domains due to the constraint of reduced vertical displacement imposed by the surface boundary. Therefore, where tidal beams exist in the ocean, this work predicts enhanced primary production with the deep chlorophyll maximum primarily due to vertical nutrient transport.

2.2 Introduction

Internal waves are ubiquitous throughout the global ocean and, near their generation sites, affect primary production by two mechanisms. As internal waves propagate, they displace passive phytoplankton vertically through the water column, increasing the irradiance available for primary production [59, 45, 30, 37]. Internal waves may also affect primary production by enhancing the vertical supply of nutrients to the euphotic zone [2, 43, 39, 102, 103, 72, 110, 117, 116]. However, the relative contributions of the light and nutrient effects of internal waves on primary production are not clearly defined. By diagnosing the governing mechanism through which internal waves affect primary production, we gain insight into how the baseline primary production is controlled in areas above sloping bathymetry.

Some of the largest internal waves in the world are associated with internal tide generation at bathymetric features by barotropic tides (e. g. Luzon Straight: [55, 90], Hawaii: [101, 18], and Tasmania: [119]). By a variety of mechanisms internal tides can be formed (critical slopes, lee waves, etc.) and in many cases the initial character of the wave is a beam with directed energy propagation (group velocity) at an angle (θ_{Cg}) determined by the stratification ($N^2 = -\frac{g}{\rho_0}\frac{\partial \rho}{\partial z}$), the frequency of the wave (ω), and the inertial frequency (f). The ray theory relation is given by [23] as

$$\tan(\theta_{Cg}) = \sqrt{\frac{\omega^2 - f^2}{N^2 - \omega^2}}. \tag{2.1}$$

In addition, the beam can also be interpreted as a superposition of many normal modes

at the frequency ω with different eigenwavenumbers [19]. Observations indicate that the beam structure of the internal tide rarely survives one or two reflections off the ocean surface or bottom, after which the field takes on a simpler structure associated with one or two of the lowest order normal modes [2, 18, 101, 98].

The energy of the internal tide is determined by the strength of the cross-isobath tidal flow, the stratification, and the geometry of the bathymetric feature [24, 95, 35]. Regarding geometry, eqn. 2.1 is helpful since it shows the important dependence on wave frequency (ω). For typical deep ocean bathymetry and mid-latitude values of N and f, the internal tide propagation angle is small, between two and eight degrees relative to the horizontal. If the bathymetric slope is slightly larger than the internal tide propagation angle, this is considered a *supercritical* regime where barotropic tidal flows result in particularly energetic internal tide generation. Here, upward propagating tidal beams are readily observed. On the other hand, if the bottom slope is less than internal tide propagation angle (*subcritical* generation), weaker or no beam generation is observed [5]. Lastly for slopes appreciably larger than the internal tide propagation angle upward propagating energy is blocked and only down-slope moving energy survives [94, 78, 56, 67, 61, 14].

If a tidal beam is generated, the beam can change its direction by two mechaisms: 1) refraction due to variable stratification and currents and 2) nonlinear interactions generating tidal harmonics with different propagation angles (Eqn. 2.1; [35, 36, 58]). The tidal beam can also lose energy due to instability/mixing processes, surface/bottom reflection losses, as well as beam divergence [86, 75, 96, 74]. Energy loss is possible

through wave-current interactions but this case has not been well studied [54, 25]. As a tidal beam loses energy the higher order normal modes decay more rapidly causing the beam to change direction to propagate horizontally, maintaining the lower order mode structure that can persist across ocean basins [1].

Away from generation regions, internal tides directly influence primary production by displacing passive plankton through a light field that varies as an exponential function in the vertical direction. In this region, the biological response depends on the average depth of the plankton. Theoretical studies of the photosynthesis-irradiance curve suggest that its negative curvature creates a *crossover depth*. Above this depth, internal waves move plankton into depths where photoinhibition suppresses primary production. Below the crossover depth, internal waves increase depth-integrated primary production by deepening the compensation depth (the depth above which average primary production equals respiration; [59, 45]). These competing factors result in an optimum depth for primary production enhancement by internal waves based on the crossover depth.

Another factor that influences light availability for primary production is the amplitude of internal wave oscillation. Positive vertical displacement by internal waves enhance light availability for primary production more than the reduction during its negative displacement. Using a simple model of irradiance (I) for a parcel experiencing an internal wave with frequency ω relative to that at its central depth (z_0) yields an expression for the irradiance anomaly relative to an undisturbed parcel

$$I'(t) = e^{(k_{ext}(Asin(\omega t)+z_0))} - e^{(k_{ext}z_0)}. \tag{2.2}$$

It is clear that this asymmetry grows with internal wave amplitude (A). In this model, k_{ext} is the light extinction coefficient and t represents time. For example, an internal wave with a central depth of 50 m and an amplitude of 10 m experiences a 3% increase in average light relative to the light at the central depth, whereas if the amplitude is 40 m, the average light gain due to displacement increases to 55%. The net effect of internal waves on light availability for primary production is that the optimum depth for primary production enhancement is further modulated by the amplitude of the internal wave. The degree to which the light effect influences primary production will be addressed in this paper.

Internal tides may also stimulate primary production by modifying background nutrient concentrations. Observations and modeling from coastal regions suggest that breaking internal tides contribute to nutrient fluxes and higher rates of primary production [102, 57, 72, 117, 121, 124]. Observations by Tuerena et al., 2019 over the mid-Atlantic ridge suggest that the generation of internal tides contribute to the diapycnal nitrate flux [116]. These authors find that over the ridge, a large vertical nutrient gradient and higher diffusivity rates increased the diapycnal nitrate flux into the deep chlorophyll maxima by an order of magnitude relative to the adjacent abyssal ocean. Using a global tidal dissipation model, they estimate that tidal dissipation over ridges and seamounts supplies up to 62% of tidally generated nitrate flux. In each of these studies, internal tides enhance the vertical mixing of nutrients into the euphotic zone

fueling primary production.

In this study, I examine the relative influence of light and nutrient effects of the generation of internal tides on primary production using a numerical circulation model coupled to a simple biogeochemical model. Our goal in this study is twofold. First, I evaluate the primary production response to the generation of internal tide beams. Specifically, I consider how the magnitude of primary production responds to a range of bottom geometries by adjusting the height and width of bathymetric steps to create a range of step slopes. Then, to diagnose the driver of the enhanced primary production within tidal beams, I compare the relative contributions of light and nutrient availability to phytoplankton growth. I present the details of the physical and biological model in section 2.3. In section 2.4, I investigate a subcritical step to illustrate how internal tide beams affect primary production before discussing how the mechanism generalizes to a range of step heights and slopes. I then place the biological result into a physical context by discussing the role of energy conversion in modifying the nutrient environment and conclude with a brief summary in section 2.5.

2.3 Methods

2.3.1 Physical Model Configuration

This study uses the Regional Ocean Modeling System (ROMS; [105, 106]) to simulate the generation of internal tides at an idealized bathymetric step. ROMS solves the Boussinesq, hydrostatic equations of motion on a regular horizontal grid with terrain

following s-coordinates in the vertical direction.

I consider a rectangular basin subject to lateral tidal forcing to isolate energy conversion from the barotropic tide to the baroclinic internal tide following [24]. By prescribing a free-slip condition with no bottom drag and setting the Coriolis parameter to zero, energy is not lost due to interactions with the boundaries. I set the buoyancy frequency to be constant ($N^2 = 2 \cdot 10^{-3}$ s^{-1}) by using the linear equation of state and prescribing a constant salinity of 34 and a temperature profile that decreases linearly from a surface value of 12.95°C to 8.5°C near the bottom. To reduce energy loss throughout the domain there is no explicit horizontal mixing, and vertical mixing is achieved using constant viscosity and diffusivity coefficients set to 10^{-6} and 10^{-5} m^2 s^{-1}, respectively. In sensitivity experiments, I tested the impact of more complex mixing parameterization such as k-ϵ [118] and KPP [60], and found little impact of these changes from our base configuration, a result that will discussed in section 2.5.1.

Additionally, I test the sensitivity of the biological response to tidal beams using different numerical advection schemes. In the base configuration I use the upstream third-order/centered fourth-order (U3/C4) method [104] and compare our results to with the HSIMT method (High-order Spatial Interpolation at the Middle Temporal level; [122]). Details on the sensitivity to numerical advection scheme are discussed in section 2.4.2.4.

I vary the strength of energy conversion by running the model in eight domains that contain a bathymetric step with either subcritical slopes or supercritical slopes and in a barotropic reference domain with flat-bottom bathymetery. The angle

of supercritical slopes considered in this study allow for both upward and downward energy propagation. Each domain is a rectangular basin, 1500 km by 6 km in the x- and y-directions, respectively, with a maximum depth of 2000 m. Boundaries are set as periodic in the x-direction and closed in the y-direction. The horizontal resolution is 1.5 km. The vertical grid includes 200 terrain following levels spaced equally by 10 m in the deepest region of the domain and by 3.5 to 7 m over bathymetry, depending on the height of the step. The flat-bottom domain has a constant depth of 2000 m and serves as a reference without baroclinic motions. Within the eight experimental domains I construct a step transition in the center of the domain as a fourth-order polynomial

$$h = h_{max} \begin{cases} 0 & \text{if } x > a \\ \left(1 - \frac{x^2}{a^2}\right)^2 & \text{if } 0 < x < a \\ 1 & \text{if } x < 0 \end{cases} \tag{2.3}$$

such that the slope of the step is continuous at the top and bottom. I set the width parameter, a, to 30 km for subcritical cases and to 10 km for supercritical cases. I set the height of the step, h_{max}, to 600 m, 800 m, 1000 m, and 1300 m for both subcritical (fig. 2.1A) and supercritical cases (fig. 2.1B).

The model is integrated with a 30 second time step and is forced with an idealized barotropic tide by supplying a body force to horizontal momentum equations as $B_u(t) = \omega U_0 cos(\omega t)$ [24]. The frequency is set as the single M_2 harmonic ($\omega = 1/12.4$ hr^{-1}) with a maximum velocity (U_0) of 0.2 m s^{-1}. The analysis period is between the fourth and twelfth M_2 cycle (days 2 - 6). Limiting the analysis period to this length

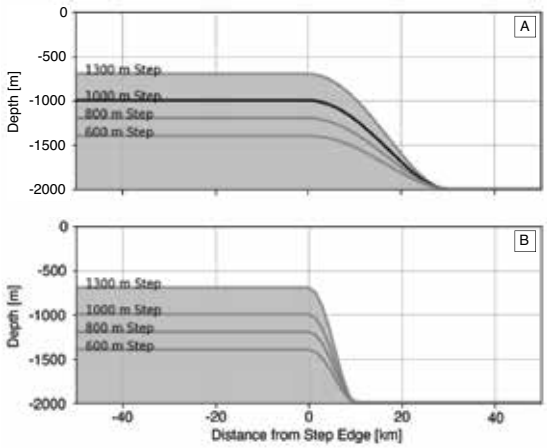

Figure 2.1: Bathymetric step heights considered in the simulation of internal tides with (A) subcritical and (B) supercritical slopes. The 1000 m subcritical step bathymetry discussed more extensively in the text is emphasized with a black line in (A)

prevents baroclinic energy from reentering the domain through the periodic boundaries.

2.3.2 Biological Model Configuration

I represent primary and secondary production with a simple, nitrogen-based nutrient, phytoplankton, zooplankton, detritus (NPZD) model adopted from [32]. The governing equations are:

$$\frac{dN}{dt} = \underbrace{-P\frac{V_m N}{k_s + N}e^{k_{ext}z}}_{\text{N uptake by P}} + \underbrace{(\beta\frac{R_m P^2}{\Lambda^2 + P^2} + M_n)Z}_{\text{Excretion by Z}} + \underbrace{rD}_{\text{D remin.}} + \underbrace{K_v\frac{d^2N}{dz^2}}_{\text{Vertical mixing of N}} \tag{2.4a}$$

$$\frac{dP}{dt} = \underbrace{P\underbrace{\frac{V_m N}{k_s + N}}_{\text{Michaelis-Menten uptake}}\underbrace{e^{k_{ext}z}}_{\text{Light function}}}_{\text{Primary production (N uptake)}} - \underbrace{\frac{R_m P^2}{\Lambda^2 + P^2}Z}_{\text{Grazing of P by Z}} - \underbrace{mP}_{\text{P mortality}} + \underbrace{K_v\frac{d^2P}{dz^2}}_{\text{Vertical mixing of P}} \tag{2.4b}$$

$$\frac{dZ}{dt} = \underbrace{(1-\gamma)\frac{R_m P^2}{\Lambda^2 + P^2}Z}_{\text{Z assimilation of P}} - \underbrace{M_n Z}_{\text{Z excretion}} - \underbrace{M_d Z}_{\text{Z mortality}} + \underbrace{K_v\frac{d^2Z}{dz^2}}_{\text{Vertical mixing of Z}} \tag{2.4c}$$

$$\frac{dD}{dt} = \underbrace{mP}_{\text{P mortality}} + \underbrace{(\gamma - \beta)\frac{R_m P^2}{\Lambda^2 + P^2}Z}_{\text{Sloppy feeding}} + \underbrace{M_d Z}_{\text{Z mortality}} - \underbrace{rD}_{\text{D remin.}} + \underbrace{K_v\frac{d^2D}{dz^2}}_{\text{Vertical mixing of D}} . \tag{2.4d}$$

In these equations, $\frac{d}{dt}$ represents a Lagrangian derivative (i.e., including advective terms). This model includes vertical diffusivity for biological tracers ($K_v = 10^{-5}$ m^2 s^{-1}) and neglects both sinking and horizontal mixing. The light function is represented as a simple exponential decay with depth and with constant amplitude. Though I have found our qualitative results to be insensitive to these parameters, I choose parameter values representing an oligotrophic ecosystem with small phytoplankton and small zooplankton. The nitrate half-saturation value (K_s) reflects naturally occurring phytoplankton in oligotrophic environments and is 0.1 mmol N m^{-3} [28, 73]. In oligotrophic environments, grazing by small zooplankton is at a similar rate to the growth of small phytoplankton, so the zooplankton maximum grazing rate (R_m) is set to 0.4 d^{-1}, and the maximum nutrient uptake rate (V_m) is 0.6 d^{-1} [112, 111]. I assume zooplankton are inefficient consumers in oligotrophic environments by setting the grazing efficiency

coefficient (γ) to 0.7 and the zooplankton excretion coefficient associated with grazing (β) to 0.15. The phytoplankton mortality rate (m), zooplankton excretion rate (M_n), and zooplankton mortality rate (M_d) are all set to 0.01 d^{-1}. Light intensity at the surface is set to one and the light attenuation coefficient (k_{ext}) is assumed to be 0.035 m^{-1}. The level of half saturated grazing (Λ) is tuned to 0.4 mmol N m^{-3}.

Before coupling to the physical model, I compute a stable, vertical profile for the NPZD model initialization based on nutrient and chlorophyll concentrations measured at station ALOHA, Hawaii. Profiles of chlorophyll-a are taken from observations at station ALOHA and are converted to mmol N by assuming a C : chl-a weight ratio of 25:1 and a C:N molar ratio of 6.6:1, resulting in a conversion factor of 3.8 mmol N chl-a^{-1} ([53, 64]). I then estimate the profile of total nitrogen ($N_T(z)$) by assuming N_T is proportional to chlorophyll-a in the upper 120 m, to average nitrate from station ALOHA between 120 m and 200 m depths, and constant below 200 m. From 65 m to 215 m depth I linearly interpolate N_T from the chlorophyll-based estimate to the nitrate-based estimate to produce a smoothly varying profile. The ROMS domain is then initialized with laterally uniform profiles as calculated above and tested for further non-steady evolution. Figure 2.2 shows the initial profiles for the NPZD model (solid lines) and the final state (dotted) after the six-day integration in the barotropic reference domain. Field changes over 6 days are small, and much smaller than changes associated with internal tides to be studied below.

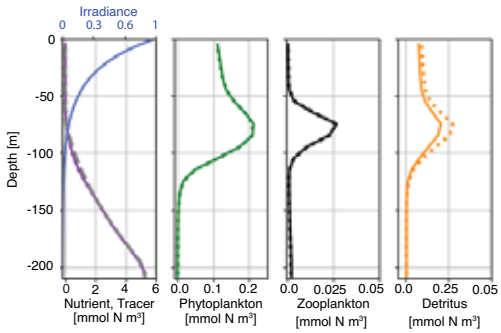

Figure 2.2: Initial (solid line) and final (t=6 days; dotted line) conditions for the nutrient, phytoplankton, zooplankton, and detritus concentrations in the internal tide simulations. The initial profile of the nutrient-like tracer is shown as the grey dashed line and the irradiance profile is shown as the blue line in leftmost panel. Note different x-axis limits between plots.

2.3.3 Passive Tracer and Lagrangian Floats

A passive tracer is used in this study to track the redistribution of nutrients by the generation of internal tides. I initialize passive tracers with a profile resembling nutrients of the NPZD model (fig. 2.2, grey dashed line). I leverage the abiotic nature of the "nutrient-like" tracer, s, to determine the physical mechanisms that drive the time evolution of nutrients within the tidal beam. The budget for s can be written as:

$$\frac{\partial s}{\partial t} = -\underbrace{\nabla \cdot (s\boldsymbol{u})}_{Advection} - \underbrace{K_v \frac{\partial^2 s}{\partial z^2}}_{Diffusion}, \tag{2.5}$$

where $\boldsymbol{u}$ is the two-dimensional (x, z) velocity vector and K_v is the vertical diffusivity coefficient. The time-rate of change of s equals the sum of the advective flux divergence of s and its vertical diffusive flux divergence. Additionally, I capture the effect of the generation of tidal beams on nutrient redistribution by considering the average anomaly ($\langle s' \rangle$) of a model simulation with a bathymetric step and internal wave generation rela-

tive to the flat bottom reference case

$$\left\langle s' \right\rangle = \langle s_{step}(x,z,t) - s_{ref}(x,z,t) \rangle \tag{2.6}$$

which is nonzero when baroclinic motions adjust the position of the nutricline relative to the barotropic reference case. A similar anomaly is computed to capture the effect of internal tide generation of primary production. In both cases, positive anomalies indicate locations where tidal beams increase the level above the barotropic reference.

Separately, Lagrangian floats track how internal tides displace water parcels containing the same NPZD model described above. Lagrangian floats are released at every horizontal grid point in each domain at the beginning of the fourth M_2 cycle at 5 m increments from 5 m to 25 m depth and at 25 m increments from 25 m to 200 m depth. These Lagrangian plankton ecosystems allow us to determine the relative contributions of light and nutrient availability to primary production. I accomplish this by separating the primary production equation, see eqn. 4.3b, into a maximum rate V_m, light factor ($e^{k_{ext}\ z}$), and nutrient factor ($(N)/(k_s+N)$). Light and nutrient factors for passive plankton displaced by the internal tide are compared to those at the average depth of the orbital. Specifically, the light effect of vertical displacement by internal oscillations on primary production is obtained by defining an internal wave light factor (Lf),

$$Lf = \langle e^{k_{ext} z(t)} \rangle - e^{k_{ext} \langle z(t) \rangle} \tag{2.7}$$

that subtracts the light level at the average orbital depth from the average amount of light a (Lagrangian) passive plankton experiences over a tidal cycle. Similarly, the effect of tidal beams on nutrient availability is computed using an internal wave nutrient factor (Nf),

$$Nf = \left\langle \frac{N(z,t)}{k_s + N(z,t)} \right\rangle - \frac{N(\langle z \rangle, t_0)}{k_s + N(\langle z \rangle, t_0)} \tag{2.8}$$

which measures the effect of internal wave displacement on nutrient availability relative to an unperturbed depth. Nf is the difference between the average nutrient concentration along an orbital trajectory ($N(z,t)$) and the initial nutrient concentration at the average depth of the orbital ($N(\langle z \rangle, t_0)$).

These light and nutrient factors are designed to compare the average level experienced by a passive plankton as it is displaced by the internal tide to the level experienced at the average depth of internal tide orbital. These metrics account for both the magnitude of displacement (height of the orbital) and any possible adjustment of the central position of the orbital. By separating the primary production equation in this way, I evaluate how internal tides affect light and nutrient availability for primary production, and I determine the sensitivity of each factor to bathymetric geometry.

2.4 Results

2.4.1 Subcritical Tidal Beams and Primary Production

2.4.1.1 Kinetic Energy and Tidal Beam Generation

Using the 1000 m subcritical step domain highlighted in figure 2.1A as an example, I illustrate tidal beams and their effect on light and nutrient availability for primary production. As the barotropic tide encounters the step transition, energy is converted to baroclinic motion that propagates away from the step oriented along θ_{Cg} in both the up- and down-range directions. Figure 2.3 shows the position of the subcritical tidal beam as regions of elevated average kinetic energy. As the beam propagates down range in the negative x direction, kinetic energy is largest where the beam reflects off surface and bottom boundaries, with the maximum of 48 Joules occurring at the first surface bounce. From the kinetic energy maximum, I determine the origin of the tidal beam by tracing a ray path downward along θ_{Cg} to the mid-point of the step transition (fig. 2.3 dashed line). At the same time, an initially downward propagating beam reflects off the bottom boundary and propagates up-range along θ_{Cg}. In this direction, the average kinetic energy is lower, reaching a maximum of 10 Joules. Tidal flow over a subcritical slope generates a spatially coherent up-slope traveling beam that I identify from the average kinetic energy maximum.

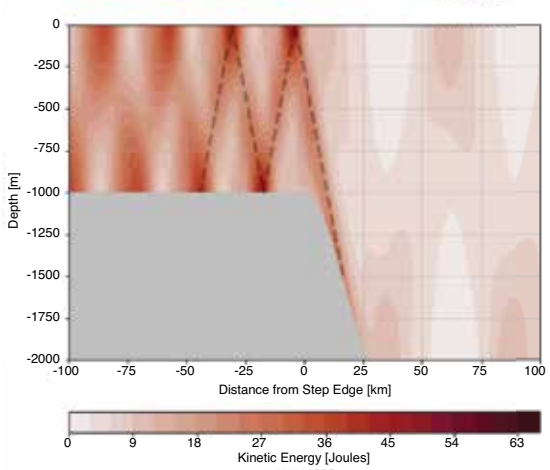

Figure 2.3: Average kinetic energy for the 1000 m subcritical step. The dashed line shows the first two bounces of the subcritical tidal beam traveling along the ray path prescribed by θ_{Cg}.

2.4.1.2 Enhanced Primary Production

The effect of the generation of tidal beams on primary production is examined by considering the average anomaly of primary production ($\langle PP' \rangle$) from the barotropic case. Similar to eqn. 2.6, $\langle PP' \rangle$ is computed by subtracting primary production in the barotropic reference case from the baroclinic experimental case such that positive values indicate locations where internal tides increase primary production. Figure 2.4A shows that primary production is enhanced above the barotropic reference case within the tidal beam ray path. For this 1000 m step example, the largest increase in primary production is subsurface, near the first surface bounce of the forward transmitted tidal beam and decreases at subsequent surface bounces. An example profile of average primary production (fig. 2.4B) outside the beam path below the red star (red line) remain qualitatively and quantitatively similar to the barotropic reference case (black dotted

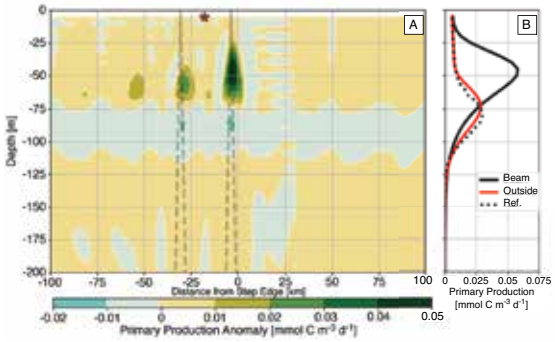

Figure 2.4: Primary production anomaly from the barotropic reference case for the 1000 m subcritical step with the first two bounces of the subcritical tidal beam ray path shown as the dashed line (A) Panel (B) shows average profiles of primary production from the reference case (dotted line), below the first surface bounce (solid black line), and outside of the tidal beam ray path (red line and star in (A)

line). Similarly, there is relatively little change in primary production in the down-slope direction (positive x). These results suggest that primary production remains largely unaltered by the generation of the internal tides outside the beam path and that primary production is enhanced particularly within the beam path. The spatial coherence of the primary production anomaly with the position of the tidal beam motivates us to investigate whether tidal beams increase the availability of light or nutrients for primary production.

2.4.1.3 Light Control of Primary Production within Tidal Beams

As an internal tide propagates, it oscillates passive phytoplankton vertically through varying light levels, controlling the total light available for primary production. If the light field changed linearly with depth, the light intensity increase on the upward portion of the orbital would equal the light intensity decrease on the downward portion

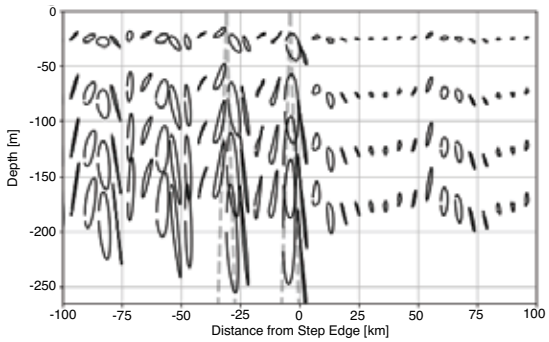

Figure 2.5: Tidally average Lagrangian trajectories for the 1000 m subcritical step with the position of the subcritical beam is shown as the dashed line.

for a symmetric orbit. However, light intensity decays exponentially with depth in the ocean (fig. 2.2, blue line). Phytoplankton experience more light on the upward portion of the orbital than the light lost on the downward portion, and the magnitude of vertical displacement increases the amount of light gained overall. Larger oscillations result in overall more light available for primary production.

To capture how tidal beams affect light availability for primary production, I represent passive plankton with Lagrangian floats. Floats are released throughout the euphotic zone and their position tracked over the analysis period (4^{th} - 12^{th} M_2 cycle). The position of each float is then averaged according to the phase of the barotropic tide to produce a representative trajectory of passive plankton over a tidal cycle (fig. 2.5). Tidally averaged trajectories show that all orbitals orient in the direction of beam propagation (dashed line), and the vertical extent of orbitals is larger within the tidal beam than outside. Because the average light experienced by the particle is proportional to the vertical displacement, eqn. 2.2, phytoplankton within the tidal beam are less light-limited than those outside.

2.4.1.4 Tidal Beams and Nutricline Adjustment

The generation of internal tide beams may also affect the availability of nutrients to primary producers within the euphotic zone. In the Lagrangian frame, internal tides move nutrients with plankton into more well-lit regions. However, in the fixed (Eularian) frame, internal tides transport nutrients from deeper in the water column. To show how nutrients are affected by the generation of tidal beams in the fixed reference frame, I employ the abiotic passive tracer with an initial profile similar to the nutrient, referred to here as the "nutrient-like" tracer, s, to evaluate this possible relationship. The average anomaly of the nutrient-like tracer from the barotropic reference case ($\langle s' \rangle$; eqn. 2.6) highlights regions where internal tides vertically redistribute nutrients (fig. 2.6A). The positive nutrient-like tracer anomaly within the ray path (fig. 2.6A dashed line) shows that tidal beams increase nutrient concentrations within the euphotic zone. The positive anomaly is largest and shallowest near the first surface bounce of the tidal beam and decreases with subsequent bounces. Profiles of the average tracer show that near the first surface bounce, tracer levels increase between approximately 30 m and 180 m depths (fig. 2.6B, black line). Furthermore, outside the tidal beam, the average nutrient-like tracer profile (fig. 2.6A red star; fig. 2.6B, red line) is quantitatively similar to the reference case (fig. 2.6B, dotted line). These results show that the effect of internal tide generation on the nutrient field is contained within the tidal beam path.

Consistent with $\langle s' \rangle$, figure 2.7A shows that the time-averaged position of the tracer-cline shoals within the tidal beam ray path (dashed line). By considering

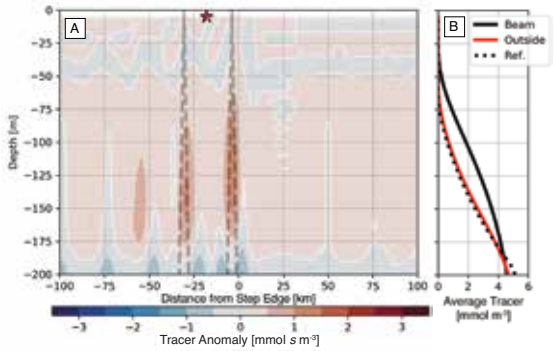

Figure 2.6: Nutrient-like tracer anomaly from the barotropic reference case for the 1000 m subcritical step shown with the position of the subcritical tidal beam (A). Panel (B) shows average profiles of the nutrient-like tracer from the reference case (dotted line), below the first surface bounce (solid black line), and outside of the tidal beam ray path (red line and star in (A).

the budget of s, eqn. 2.5, I determine the physical mechanism that drives the time evolution of the nutrients, which is controlled by either vertical mixing or advective flux divergence. The average tracer advective flux divergence (fig. 2.7B) shows that regions of persistent divergence (blue) and convergence (red) are oriented in the direction of the tidal beam. Within convergences, the upward flux of material is only partially compensated by horizontal fluxes, resulting in a net accumulation and an uplift of the nutricline (fig. 2.7A). Tidal beams adjust the position of the tracer-cline and similarly, the nutricline by creating spatially persistent regions of convergence and divergence.

The relative scales of the advective flux divergence and mixing determine the dominant mechanism that drives the evolution of nutrients within the tidal beam. I define scales based on our numerical results as follows: U = 0.1 m s^{-1}, W = 0.003 m s^{-1}, L= 5000 m, H= 350 m, and $K_v = 10^{-5}$ m^2 s^{-1}, for horizontal velocity, vertical velocity, horizontal length scale, vertical length scale, and diffusivity, respectively. Using

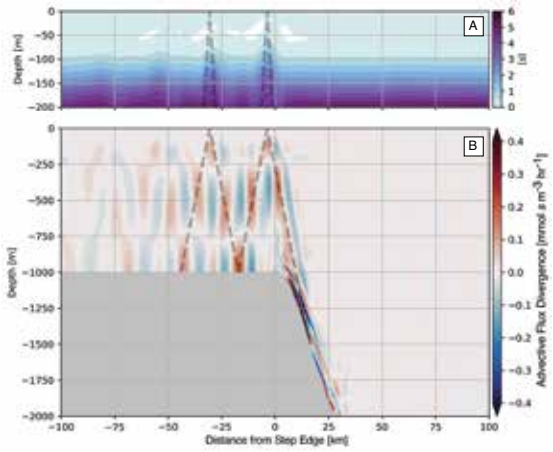

Figure 2.7: Average nutrient-like tracer over the 1000 m subcritical step (A) and the average advective flux divergence of the nutrient-like tracer (B). The position of the subcritical tidal beam is shown as the dashed line in both panels.

these values and neglecting the arbitrary amplitude of the tracer, I find that horizontal and vertical terms within the advective flux divergence are of O(10^{-5} s^{-1}; fig. 2.7B), whereas the diffusive flux divergence is O(10^{-10} s^{-1}). This scaling analysis suggests that the advective flux divergence is several orders of magnitude larger than mixing in these idealized simulations, and our diagnostics support this conclusion. As mentioned previously, the use of an advanced mixing parameterization does not alter the contribution of mixing substantially. I note that even using $K_v = 10^{-2}$ m^2 s^{-1}, which is considerably larger than typically observed near tidal beams in nature (*e. g.* [116]), yields a scale for the mixing term of O(10^{-7} s^{-1}), still small compared to the advective flux divergence found numerically in these experiments. Based on this scaling analysis, I argue that tidal beams locally increase the advective flux of nutrients, causing the nutricline to shoal, which fuels primary production near the base of the euphotic zone.

2.4.2 Sensitivity Studies

2.4.2.1 Subcritical Step Height

Adjusting the height of the subcritical step alters the kinetic energy content, depth of the nutricline, and primary production response within the tidal beam. In each of the subcritical step domains, a single forward transmitted tidal beam occurs. Near the first surface bounce of the tidal beam, average kinetic energy for the 600 m, 800 m, 1000 m, and 1300 m reaches maximum values of 25, 35, 48, and 63 Joules, respectively, indicating a linear relationship between step height (h_{max}) and maximum kinetic energy described by $KE_{max} = 0.0469\text{J m}^{-1} \cdot h_{max} (R^2 = 0.9973)$. In response, the maximum nutrient-like tracer anomaly (s'_{max}) increases with step height as 0.427, 0.854, 1.380, 1.763 mmol N m^{-3} s^{-1} resulting in the linear relationship described by $s'_{max} = 0.0013$ mmol N m^{-3} s^{-1} $\text{m}^{-1} \cdot h_{max}$; ($\text{R}^2 = 0.9775$). Similarly, the maximum primary production anomaly (PP'_{max}) increases with step height as 0.009, 0.021, 0.050, and 0.053 mmol C m^{-3} s^{-1} and results in a linear relationship described as $PP'_{max} = 4 \cdot 10^{-5}$ mmol C m^{-3} s^{-1} $\text{m}^{-1} \cdot h_{max}$ ($\text{R}^2 = 0.9253$). These linear correlations suggest that increases in subcritical step height proportionally raise the amount of kinetic energy in the system, resulting in greater uplift of the nutricline fueling higher rates of primary production.

In contrast to the nutricline adjustment, Lagrangian orbital trajectories within the euphotic zone respond less strongly to taller subcritical steps than deeper parcels, as they are constrained by near zero motion at the surface. While large amplitude

displacements in the euphotic zone ($\sim$ 50 m) can result in substantial changes to the light anomaly (eqn. 2.2) and, in turn, primary production, such displacements in the upper 100 m did not occur in our experiments. More limited displacements obtained here ($>$ 25 m) result in only weak changes in the light anomaly and thus primary production.

2.4.2.2 Supercritical Slopes and Tidal Beam Generation

Bathymetry with a supercritical slope efficiently converts incoming (barotropic) tidal energy to (baroclinic) internal tides. As a result, two tidal beams emit from the critical point. I use the average kinetic energy for the 1000 m supercritical step as an example to compare these beams (fig. 2.8A). As the tide flows over the supercritical step, an initially Upward Propagating Beam (UPB) propagates down range, and separately, an initially Downward Propagating Beam (DPB) emits from the critical point, which then reflects off the bottom boundary before reaching the surface. The average kinetic energy within UPB is greater and more spatially coherent than the DPB, a consistent feature across the four supercritical step domains.

The regions of elevated average kinetic energy within the two tidal beams that emit from a supercritical slope affect the position of the nutricline and the level of primary production. Both UPB and DPB result in positive primary production anomalies and positive nutrient-like tracer anomalies within their respective beam paths and within similar depth ranges (figs. 2.8B, 2.8C), a feature that is consistent across the four supercritical step domains. However, the main difference between the two beams

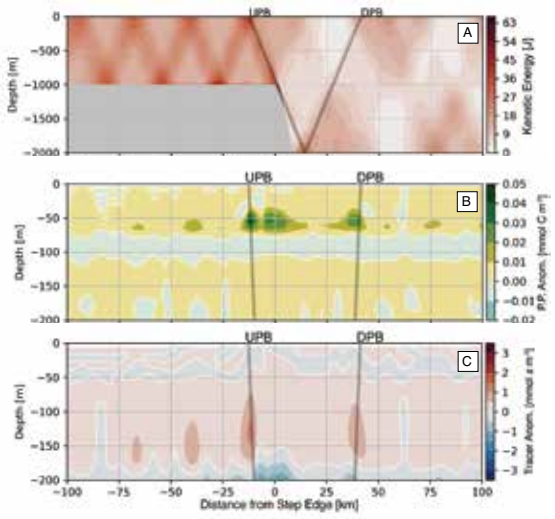

Figure 2.8: Average kinetic energy (A), average primary production anomaly (B), and average nutrient-like tracer anomaly (C) are shown for the 1000 m supercritical step. The positions of the initially Upward Propagating Beam (UPB) and the initially Downward Propagating Beam (DPB) are shown as the grey lines. Note the change in depth range between panel (A), and panels (B) and (C).

that emit from the critical slope is that UPB contains more kinetic energy, a larger nutrient-like tracer anomaly, and a shallower average depth of the nutricline compared to DPB. Coincident with these features is a larger maximum primary production anomaly within UPB compared to DPB. The third region of enhanced primary production located between UPB and DPB is discussed below.

2.4.2.3 Higher Harmonic Tidal Beams

Supercritical steps also differ from subcritical steps in the evolution of higher harmonics within the tidal beam. A clear way to visualize this is to compare the tidally averaged orbital trajectories from the subcritial case with the trajectories from the supercritical case. In the subcritical case (e.g. fig. 2.5) only the M_2 harmonic exists

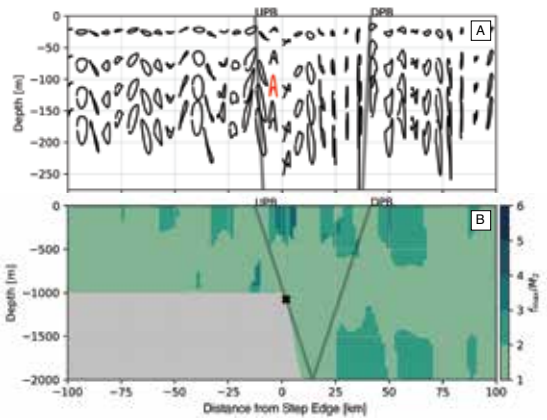

Figure 2.9: Tidally averaged Lagrangian trajectories for the 1000 m supercritical step with an example M_4 trajectory shown in red (A) and the locations of the dominant tidal harmonic shown by dividing the frequency of the peak in spectral density by the M_2 harmonic (B). The positions of the initially Upward Propagating Beam (UPB) and the initially Downward Propagating Beam (DPB) are shown as the grey lines. Note the change in depth range between panel (A) and panel (B)

and orbitals are roughly elliptical. In comparison, figure 2.9A shows tidally averaged orbital trajectories from the supercritical case where several tidal harmonics are present. Here, an example of an M_4 trajectory is highlighted in red. In this example the parcel experiencing the M_4 tidal harmonic oscillates vertically twice in the time-span of one cycle for a parcel experiencing M_2 fluctuations (by definition).

To ascertain the spatial distribution of tidal harmonics present within the critical case I shift from the Lagrangian frame (fig. 2.9A) to the fixed (Eulerian) frame (fig. 2.9B). At each grid cell I compute the power spectrum of vertical velocity (w) and identify the frequency with the largest power, the spectral peak. Figure 2.9B shows the spectral peak in each grid cell divided by the M_2 frequency; near to the surface and closer to waters directly over the step transition, spectral peaks shift from the M_2 frequency (1/12.4 hours; light green) to higher harmonics (darker greens) such as the

M_4 (1/6.2 hours), M_8 (1/3.1 hours), and higher frequencies. One major consequence of the excitation of higher tidal harmonics is that tidal beam energy propagates at a steeper θ_{Cg} (eqn. 2.1). The presence of several tidal harmonics greater than M_2 in figure 2.9B suggests that tidal beam energy is distributed over a broader region between the critical point and the first surface bounce of the M_2 tidal beam.

The energy transfer to higher harmonics affects primary production by altering orbital trajectories and the position of the nutricline near the step transition. Regarding light availability, more frequent oscillations result in a smaller vertical displacement and thus less of a change in the average light experienced; however, the average light experienced may increase due to a shift in the average depth of an parcel. Regarding the nutricline position, the redirection of energy by the evolution of higher tidal harmonics affects the locations where the nutricline is adjusted. Figure 2.8C shows a small positive anomaly of the average nutrient-like tracer over the step transition indicating that the nutricline shifts to a shallower position in the same region where higher tidal harmonics are present. The net result of the redirection of energy is an increase in primary production in a broad lateral region between the critical point and the first surface bounce of the M_2 tidal beam (fig. 2.8B).

2.4.2.4 Sensitivity to Numerical Advection Scheme

The quantitative biological transport is sensitive to the choice of the numerical advection scheme. A comparison between upstream third order/centered fourth order (U3/C4; [104]) and the HSIMT (High-order Spatial Interpolation at the Middle Tem-

poral level; [122]) advection schemes for tracers shows a quantitative difference in tracer concentration and level of primary production. One artifact of the U3/C4 advection scheme is that advection can cause tracer concentrations to become negative (fig. 2.6, white regions). In practice, negative concentrations are small and kept small owing to very small imposed reallocations within this ROMS/NPZD implementation of nitrogen from the largest biological state variable to the previously negative pool. The HSIMT scheme avoids this problem because it is positive-definite. Higher harmonic tidal beams simulated with the HSIMT scheme increase nutrient advection and subsequent primary production response relative to the more standard and widely used U3/C4 method. This result indicates uncertainty in the magnitude of the response, although both advection schemes produce the same qualitative result of increased primary production in the tidal beam paths.

2.4.3 Relative Control of Light and Nutrients on Primary Production within Tidal Beams

I assess the relative control internal tides place on the availability of light and nutrients for primary production across the range of bathymetric step heights and slopes. In each domain, I compute primary production, the internal wave light factor (eqn. 2.7), and the internal wave nutrient factor (eqn. 2.8) for passive phytoplankton represented by Lagrangian floats initially released at 50 m depth within 50 km of the top of the step transition to focus on the first two bounces of the forward propagating tidal beam.

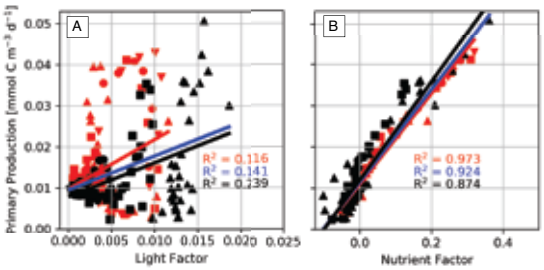

Figure 2.10: Internal wave Light (A) and Nutrient (B) Factors regressed against primary production for Lagrangian floats released in domains with a 600 m step (downward triangles), 800 m step (circles), 1000 m step (squares), and the 1300 m step (upward triangles). Red lines and symbols are regressions for supercritical step domains, black lines and symbols are for subcritical step domains, and the blue line is the regression for the combined data set.

The Light Factor, *Lf*, shows that displacement through the light field results in a 2% change in primary production. The small contribution of *Lf* to primary production indicates that the integral of the light available over a tidal cycle changes slowly with increasing displacement caused by a more intense tidal beam. Furthermore, linear regressions show that the light factor accounts for 11.6% of the variance of primary production for supercritical steps (fig. 2.10A; red symbols, line), 23.9% for subcritical steps (fig. 2.10A; black symbols, line), and 14.1% for the combined data sets (fig. 2.10A; blue line). Each regression has a different slope and intercept, indicating that the relationship between primary production and *Lf* is sensitive to the bathymetric slope. In addition, regressions for individual domains have a wide range in slope and intercept, showing *Lf* is sensitive to bathymetric height. These results indicate that the change in light availability by tidal beam propagation explains a small portion of primary production and that the primary production response is decoupled from the characteristics of the tidal beam determined by the geometry of the generating

bathymetry.

In contrast, the relationship between the Nutrient Factor, *Nf*, and primary production shows that changes in nutrient availability result in a maximum increase in primary production by up to 38.5%. Moreover, linear regressions between the nutrient factor and primary production reveal a tight coupling between *Nf* and primary production (fig. 2.10B). *Nf* accounts for 97.3% of the variance in primary production for supercritical steps (fig. 2.10B; red symbols, red line), 87.4% for subcritical steps (fig. 2.10B; black symbols, lines), and 92.4% for the combined data sets (fig. 2.10B; blue line). The consistent slope and intercept between the three regressions suggest that the nutrient control on primary production is robust against bathymetric step height and slope. As the geometry of the bathymetry changes, so does the intensity of the tidal beam. In response, the nutrient advective flux divergence scales with w, and thus, the nutrient factor is sensitively dependent on w and tidal beam intensity.

2.5 Discussion

2.5.1 Energy Conversion and the Nutricline

The primary production response to tidal beam generation results from two processes (fig. 2.11A). First, barotropic tidal energy is converted into baroclinic energy as the tide is forced over the bathymetric step locally displacing isopycnals vertically. The constraint on the direction of baroclinic energy propagation causes kinetic energy to localize into a tidal beam that propagates in the direction of θ_{Cg} away from the step

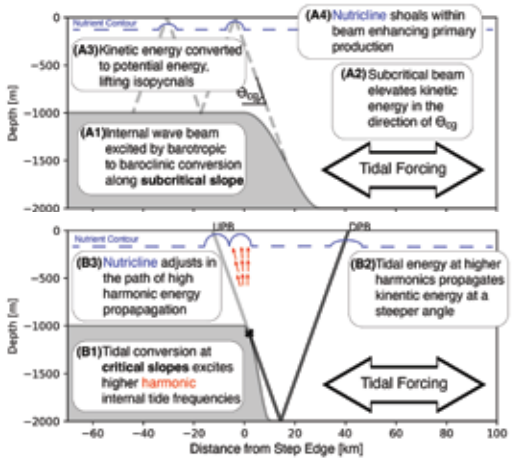

Figure 2.11: Conceptual models showing the processes that connect tidal beam generation to nutricline uplift over a subcritical step (A) and how multiple tidal beams affect the nutricline over topography with a critical slope (B).

transition. The limited spatial extent of the tidal beam, combined with vertical changes in density, result in a local advective flux divergence and a net uplift of isopycnal surfaces. In the upper region of the water column, isopycnal shoaling also carries nutrients and results in a locally shallower nutricline. Transport of nutrients vertically stimulates primary production within the tidal beam ray path.

The net advective flux divergence connects the position and strength of the tidal beam to the primary production response by causing the nutricline to shoal (figs. 2.11A, 2.11B). This mechanism explains the large correlation between the nutrient factor and primary production (fig. 2.10). The kinetic energy within the tidal beam depends on the height and slope of the bathymetric step through the tidal conversion process. Therefore, the tidal conversion determines the amount of kinetic energy available for the advective flux divergence, the subsequent vertical displacement of nutrients, and the

magnitude of the primary production response. The relationship between the energy content of the tidal beam and the primary production response is robust across step height and slope, indicating that nutrient enhancement is the larger effect on primary production within tidal beams.

Previous work on the response of primary production to the internal waves light effect suggests that the displacement of phytoplankton through the exponentially varying light field deepens the compensation depth, increasing integrated water column productivity [59, 45, 30]. The light factor presented here confirms that displacement through the light field increases primary production, but its effect is relatively small compared to the nutrient factor. In these experiments, the nutrient factor ranged from -5% to nearly 40%. A negative nutrient factor means that the displacement by internal waves reduced nutrient availability relative to a stationary position. In contrast, the light factor varied by 2%. With the bathymetric geometries test here, primary production is nearly linearly dependent on the nutrient factor. In contrast, the light factor exhibited considerable scatter about a line, with low predictive skill and more considerable variability. I note that the light factor may be the dominant effect far from the generation region where the nutrient factor is negligible.

Observational and modeling studies that consider the effect of internal waves on primary production suggest that internal tides increase nutrients in the euphotic zone by elevating mixing to levels near $O(10^{-4})$ [43, 39, 102, 103, 72, 110, 117, 116]. In the work reported here, I assumed constant vertical diffusivity of 10^{-5} m^2 s^{-1}. However, tests with realistic subgridscale mixing parameterizations did not show in these exper-

iments substantial changes to the mixing-induced fluxes or large quantitative changes to overall primary production. Instead, tidal beams drive convergences in the nutrient field, increasing nutrient concentrations in the euphotic zone and stimulating primary production. Of course, divergences are also present; in these experiments divergences occur deeper in the water column or at locations adjacent to the convergences. The divergence effect is modest due to the nutricline structure and it is clear that the dominant factor in controlling the position of the nutricline is due to convergence.

2.5.2 Global Context

One critical difference between our experiments and observations in the field is that tidal beams in nature do appear to be present beyond the first surface bounce [2, 18, 101]. I suspect that the dissipation of the tidal beam is related to surface interactions, possibly also influenced by variable stratification in the upper ocean and near the surface. As a result, implications from this study beyond the first surface bounce should be viewed as most likely a result of the numerical configuration.

Global simulations of barotropic-baroclinic tidal conversion show that it is common throughout the world ocean, though some locations are more efficient at generating tidal beams than others [108]. For example, observations over the Mid-Atlantic Ridge suggest that the tidal supply of nitrate is sufficient to sustain phytoplankton growth in the deep chlorophyll maximum in the oligotrophic gyre [116]. In our experiments, both subcritical and supercritical slope configurations enhanced primary production relative to the reference case. Generally, taller step heights with greater associated energy con-

version stimulated the largest primary production response. Based on our results, tidal beams generated by a range of bottom slopes in nature likely support ranges of primary production enhancements through aiding nutrient supply to the euphotic zone above by increasing the advective flux divergence within the nutricline.

2.5.3 Summary

This study examines the primary production response to the generation of tidal beams over a range of bathymetric step heights and slopes. Larger orbital trajectories of passive plankton within tidal beams reduce subsurface light limitation, leading to higher rates of primary production. However, correlations between light enhancement and primary production in the Lagrangian reference frame suggest this is a relatively small effect. A nutrient flux convergence within tidal beams increases nutrient availability in the euphotic zone near tidal beam generation locations, fueling higher rates of primary production. Correlations between the nutrient factor and primary production indicate that nutrient supply is the larger effect of tidal beams on primary production. Because a body force generates tidal beams, they represent a mechanism that will persistently fuel primary production within the deep chlorophyll maxima, thereby contributing to the baseline level of primary production near ridges, seamounts, and escarpments throughout the global ocean.

Chapter 3

Island Trapped Waves Enhance Primary Production in Idealized Numerical Models

3.1 Abstract

An Island trapped wave (ITW) is a special case of coastal trapped waves where a resonant interaction with forcing causes baroclinic energy to become confined around an island. Developing evidence indicates that ITWs affect primary production. To investigate, I conduct numerical experiments configured with the Regional Ocean Modeling System (ROMS) coupled with a simple nutrient, phytoplankton, zooplankton, detritus (NPZD) model. I examine ecosystem responses to ITWs under different surface light and wind stress conditions. Simulations reveal that the ITW propagates as a nonlinear wave with a sharp downwelling wavefront preceded by a broad upwelling region. The

base configuration, forced by homogeneous clockwise rotational wind stress, showed elevated nutrients result in a 16.5% increase in average primary production within the ITW influence zone. Increasing wind stress led to a 27.4% primary production enhancement, highlighting a dependency on wind stress magnitude. I examine primary production through a metric dependent on correlations between phytoplankton biomass, nutrient levels, and light availability. In experiments with constant surface light, this metric indicates that the magnitude of the primary production response results from a correlation between phytoplankton biomass and nutrient levels. Simulations with a diel light cycle result in an asymmetric enhancement of primary production around the island due to an elevated correlation between light and nutrient fluctuations. The largest primary production occurs where the ITW upwelling phase occurs with maximum light intensity, emphasizing the ITWs' role in modulating ecosystems around islands.

3.2 Introduction

Coastal trapped waves readily occur throughout the global ocean where the rotation of the planet causes low frequency barotropic and baroclinic waves to propagate with the coast to the right in the northern hemisphere and to the left in the southern hemisphere [9, 21, 47, 99]. In the case of an island with a continuous coastal boundary, waves can propagate around it in resonance with wind forcing, generating an Island Trapped Wave (ITW) [69, 70, 42, 7]. Wave displacements are amplified in the vicinity of an island and they have been observed to coincide with local increases in net primary

production and elevated nutrient availability [66, 76]. However, the mechanism through which the ITW enhances primary production remains unclear and is the focus of this paper.

Baroclinic motions such as internal waves and ITWs can influence primary production by altering the amount of light and nutrients available to phytoplankton. Light availability for primary production increases when phytoplankton are displaced vertically through an exponentially varying light field, exposing them to higher average light levels [44, 85]. Similarly, baroclinic motions may also increase nutrient availability for primary production by either enhancing mixing or by creating local nutrient flux convergences [30, 45, 49, 72, 102, 121]. For ITWs, I aim to determine whether changes in light or nutrient availability control the primary production response.

The mechanism that leads to the trapping of wave energy around islands is nearly identical for barotropic and baroclinic cases [123]. As such, I will briefly introduce the theoretical description for the barotropic ITW before discussing the baroclinic case. The differential equation describing the evolution of surface elevation, ζ, for long waves trapped around a cylinder in a rotating system is:

$$\left(\nabla^2 + \frac{\sigma^2 - f^2}{gh}\right)\zeta = 0, \tag{3.1}$$

where ∇^2 is the horizontal Laplacian, σ is the frequency of the wave, f is the Coriolis frequency, g is gravitational acceleration, and h is a uniform bottom depth. Following Longuet-Higgins (1969), for subinertial waves with frequencies lower than f, the solution to equation 3.1 in polar coordinates is:

$$\zeta = K_n(\kappa r)e^{i(n\theta-\sigma t)}, \tag{3.2}$$

where K_n is a modified Bessel function, r is the radial position, n is the azimuthal mode number, and θ is the azimuthal position [70]. Lastly, κ is the wavenumber given by the dispersion relation:

$$\kappa^2 = \frac{f^2 - \sigma^2}{gh}. \tag{3.3}$$

Rearranging the dispersion relation (eqn. 3.3) illustrates that the natural frequency of the system, σ_n, is set by $\sqrt{f^2 - \kappa^2 gh}$. When forcing by the wind or tide is near the system's natural frequency, ITW results as a resonant response.

Two primary differences exist between barotropic ITWs described above and the baroclinic case considered below. The first difference is that the effective ocean depth, h_n:

$$h_n = \frac{N^2 h^2}{g(n\pi)^2}, \tag{3.4}$$

is used in place of the real ocean depth. Here N is the buoyancy frequency and n is the integer mode number [123]. The second is that the wave speed is controlled by reduced gravity, g':

$$g' = g\frac{\Delta\rho}{\rho_0}, \tag{3.5}$$

where ρ_0 is the reference density and $\Delta\rho$ is the density difference between the upper

and lower layers of a stably stratified fluid [9, 7, 42, 84]. Mihanovic et al. (2014) showed that the resonant period for baroclinic ITWs depends on $\Delta\rho$ and the depth of the thermocline [84]. In the example considered in our study, resonance at 24-hours occurs for an island with a radius of 5250 m when the pycnocline is at 23 m and $\Delta\rho$ is 2.0×10^{-3} kg m^{-3} [84]. Other combinations of pycnocline depth and $\Delta\rho$ are of course also possible.

Observations of ITWs show that they occur with a range of resonant periods. For example, in response to a synoptic scale wind forcing, ITWs with 59-hour, 56.9-hour, and 54-hour periods were observed around the island of Hawai'i [77], Balearic Islands in Mediterranean Sea [52], and Island of Gotland, Baltic Sea [91], respectively. ITWs are also excited by shorter period wind forcing, such as around Sado Island, Japan, with a period of 48 hours [48], and around the island of Bermuda with a 26.1-hour period [123, 42, 7]. ITWs with a 24-hour period are excited by the diel land-sea breeze around the Island of Lastovo in the Adriatic Sea [83, 84, 88]. The final example motivates this study because ITWs with a 24-hour period may interact with the diel light cycle, further enhancing the biological response.

In this study, I use an idealized numerical model coupled with a simple ecosystem model to examine how an ITW affects light and nutrient availability for primary production. I present the details of the numerical models in section 3.3 and describe the physical characteristics of the ITW in section 3.4.1. In section 3.4.2, the relative contributions of light and nutrients is diagnosed by considering a case with constant surface irradiance. I then compare the constant light case to simulations with a diel

light cycle in section 3.4.4 before discussing the sensitivity to forcing scenario in section 3.4.5. Finally, section 3.5 includes a brief discussion and summary.

3.3 Methods

3.3.1 Physical Model Configuration

This study uses the Regional Ocean Modeling System (ROMS) to simulate baroclinic waves trapped around an island. ROMS solves the Boussinesq, hydrostatic equations of motion on a rectangular grid. In the vertical direction, ROMS uses terrain following s-coordinates. For a more detailed description of ROMS see [106].

This model is configured in a rectangular basin on an f-plane with an idealized cylindrical island with a radius of 5250 m placed in the center. The model domain has horizontal dimensions of 200 km by 240 km with a 0.5 km resolution in both directions. In the vertical direction, the domain has a constant depth of 100 m with a resolution of one meter. The model uses Smagorinsky-like horizontal mixing of momentum and tracers and Mellor-Yamada 2.5 vertical mixing through s-levels. Sensitivity experiments with alternate subgridscale mixing parameterizations, such as such as k-ϵ [118] and KPP [60], reveal little influence on the base configuration discussed below. At the boundaries the amount of reflected baroclinic wave energy is reduced by using radiative boundary conditions and applying a sponge layer over the outer ten kilometers. This layer linearly increases viscosity and diffusivity by a factor of 5000 at the boundary. In addition, state variables are weakly nudged over this same region back to the initial conditions with a

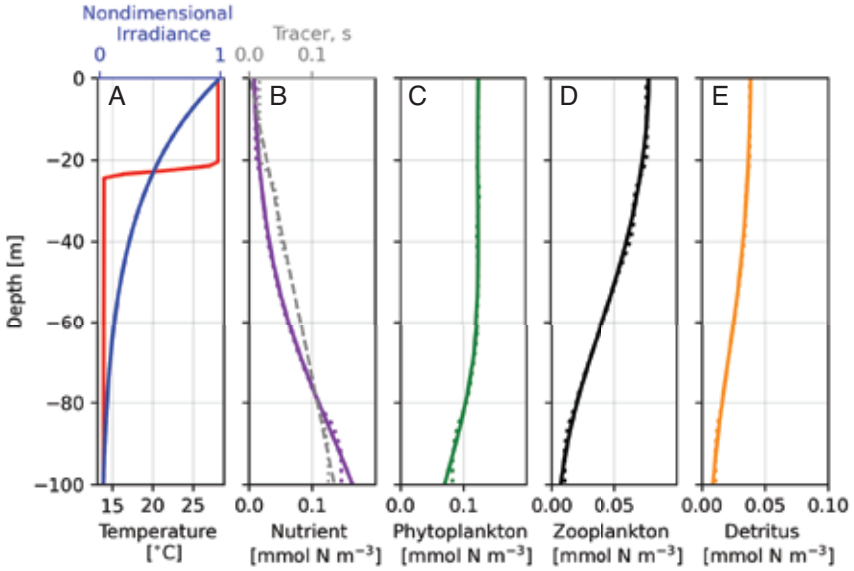

Figure 3.1: Initial conditions of temperature (A; red line), nutrient (B; purple line), passive tracer (B; grey dashed line), phytoplankton (C; green line), zooplankton (D; black line), and detritus (E; gold line). The final conditions for a case with out an island are shown for the biological variables and passive tracer as dotted lines in plots B-E. The exponentially varying light profile is shown as the blue line in A.

four-day nudging period.

Following [84], I set the system's natural frequency by initializing the physical model with a sharp thermocline centered at 23 m depth (Fig. 3.1A). Using the linear equation of state with a constant salinity of 38 and prescribing a temperature profile that transitions from the surface temperature of 28°C to 14°C between 21.5 m and 24.5 m depth, I create the necessary density change of 2.0 $\times 10^{-3}$ kg m^{-3}. To ensure water column stability, temperature decreases linearly by 0.1°C corresponding to a density change of 2.0 $\times 10^{-5}$ kg m^{-3} between the pycnocline and ocean bottom. With this configuration and an island of this size, the natural frequency of the system is set to a period of 24 hours by the dispersion relation (eqn. 3.3).

3.3.2 Biological Model Configuration

I represent the ecosystem with a simple nitrogen-based nutrient, phytoplankton, zooplankton, detritus (NPZD) model adapted from [32]. In this model, the governing equations are written as:

$$\frac{dN}{dt} = \underbrace{-P\frac{V_m N}{k_s+N}\frac{I}{I_0}e^{k_{ext}z}}_{\text{N uptake by P}} + \underbrace{(\beta\frac{R_m P^2}{\Lambda^2+P^2} + M_n)Z}_{\text{Excretion by Z}} + \underbrace{rD}_{\text{D remin.}}$$
$$+ \underbrace{K_H\nabla^2 N}_{\text{Horizontal mixing}} + \underbrace{K_V\frac{d^2N}{dz^2}}_{\text{Vertical mixing}}, \tag{3.6a}$$

$$\frac{dP}{dt} = \underbrace{P \quad \underbrace{\frac{V_m N}{k_s+N}}_{\text{Michaelis-Menten}} \quad \underbrace{\frac{I}{I_0}}_{\text{Surface Light}} \quad \underbrace{e^{k_{ext}z}}_{\text{Light function}}}_{\text{Primary production (N uptake)}}$$
$$- \underbrace{\frac{R_m P^2}{\Lambda^2+P^2}Z}_{\text{Grazing of P by Z}} - \underbrace{mP}_{\text{P mortality}} + \underbrace{K_H\nabla^2 P}_{\text{Horizontal mixing}} + \underbrace{K_V\frac{d^2P}{dz^2}}_{\text{Vertical mixing}}, \tag{3.6b}$$

$$\frac{dZ}{dt} = \underbrace{(1-\gamma)\frac{R_m P^2}{\Lambda^2+P^2}Z}_{\text{Z assimilation of P}} - \underbrace{M_n Z}_{\text{Z excretion}} - \underbrace{M_d Z}_{\text{Z mortality}}$$
$$+ \underbrace{K_H\nabla^2 Z}_{\text{Horizontal mixing}} \underbrace{K_V\frac{d^2Z}{dz^2}}_{\text{Vertical mixing}}, \tag{3.6c}$$

$$\frac{dD}{dt} = \underbrace{mP}_{\text{P mortality}} + \underbrace{(\gamma-\beta)\frac{R_m P^2}{\Lambda^2+P^2}Z}_{\text{Sloppy feeding}} + \underbrace{M_d Z}_{\text{Z mortality}} - \underbrace{rD}_{\text{D remin.}}$$
$$+ \underbrace{K_H\nabla^2 D}_{\text{Horizontal mixing}} + \underbrace{K_V\frac{d^2D}{dz^2}}_{\text{Vertical mixing}}. \tag{3.6d}$$

Here, the time derivatives of the nutrient (N, eqn. 3.6a), phytoplankton (P, eqn. 3.6b),

zooplankton (Z, eqn. 3.6c), and detritus (D, eqn. 3.6d) are expressed as total derivatives in the Lagrangian reference frame such that they are subject to advection. There is no sinking, and biological tracers are subjected to horizontal and vertical mixing.

I consider the ecosystem response to island trapped waves under constant and diel light cases. Surface irradaince is implemented by multiplying primary production (first term in eqn. 3.6b) by a nondimensional light factor, $I(t)/I_0$, where $I(t)$ is the time varying surface irradiance and I_0 is the average daily surface light intensity. In experiments with constant light, $I(t)$ equals I_0. Whereas for diel light cases (Fig. 3.3A, blue line), the 24-hour average equal to one so that the total incoming shortwave radiation is equivalent to a constant light case (Fig 3.3A, blue dash-dot line). Vertically, light is expressed nondimensionally, decaying exponentially from a maximum value of one at the surface due to a constant attenuation coefficient, k_{ext}, set to 0.035 m^{-1} (Fig. 3.1A, blue line).

The base configuration of the model is set to represent an oligotrophic ecosystem with small phytoplankton and zooplankton. A summary of parameter definitions and values used in this study is given in Table 4.1. Phytoplankton parameters such as the maximum uptake rate, V_m, and the half-saturation constant, k_s, are set to 0.6 day^{-1} and 0.1 mmol N m^{-3}, respectively, and the phytoplankton mortality rate is 0.1 day^{-1} [28]. Zooplankton maximum grazing rate (R_m) is set to 0.6 d^{-1}, and the level of half saturated grazing (Λ) is tuned to 0.4 mmol N m^{-3} such that zooplankton and phytoplankton grow at similar rates [112, 111]. Zooplankton excretion rate (M_n), and zooplankton mortality rate (M_d) are both set to 0.01 d^{-1}. In oligotrophic environments,

Table 3.1: List of definitions, symbols, and values for oligotrophic and copiotrophic parameterizations of the ecosystem model used in the island trapped wave simulations.

Parameter	Symbol	Oligo.	Copio.	Unit
Light Att.	k_{ext}	0.035	0.035	m^{-1}
Max. N. Uptake	V_m	0.6	2.0	day^{-1}
P. Mort.	m	0.01	0.05	day^{-1}
P. Half-sat.	K_s	0.1	0.1	N^{-1}
Max. Z. Gr.	R_m	0.4	1.2	day^{-1}
Z. Gr. Eff.	γ	0.6	0.9	unitless
Z. Mort.	M_d	0.01	0.05	day^{-1}
Z. Excr. Coeff.	β	0.15	0.05	unitless
Z. Gr. Sat.	Λ	0.4	0.4	N
Z. Excr. Rate	M_n	0.15	0.05	day^{-1}
Remin. Rate	r	0.1	0.1	day^{-1}
Diff. Const.	K_v	10^{-6}	10^{-6}	$m^2\ s^{-1}$

I assume zooplankton are inefficient consumers, so I set the grazing inefficiency coefficient (γ) to 0.6 and the zooplankton excretion coefficient associated with grazing (β) to 0.15. Lastly, I assume detritus will remineralize to inorganic nutrients at a rate, r, of 0.1 day^{-1}. Additionally, I test the sensitivity of the biological response to island trapped waves by running additional simulations with parameters that represent copiotrophic ecosystems; however, I found negligible qualitative sensitivity to parameter choice.

Before coupling the NPZD model to the larger three-dimensional model I gen-

erate stable initial conditions in a one-dimensional (depth) case for both oligotrophic and copiotrophic parameter sets. Plankton and detritus fields are first allowed to reach steady state subject to an enforced nutrient field that increases linearly with depth. Then all four state variables are allowed to reach equilibrium. Figure 3.1 B-E shows the initial profiles for the NPZD model (solid lines) along with the final state (dotted lines) after a seven day integration in a domain without an island. Total nitrogen, N_T, defined as the sum of NPZD fields, is held constant with depth so that the ecosystem responds to a redistribution of components rather than to an adjustment of N_T. By configuring the biological initial conditions in this way, any perturbation from this state in numerical simulations can be attributed to the imposed physical processes.

3.3.3 Forcing

To generate an island trapped wave (ITW), the model is forced at the system's natural frequency with a range of wind stress configurations, all with a 24-hour period (Table 3.2). In each simulation, wind stress is linearly increased from zero to a maximum over the first inertial period ($2\pi/f \approx 17.6$ hours). In the base experiment with constant light (Exp. 1), spatially homogeneous wind stress rotates clockwise around the island with a 24-hour period such that the ITW is continually forced throughout the simulation (Fig. 3.2A). In this scenario, the maximum wind stress is equivalent to a five-meter-per-second wind ten meters above sea level, which corresponds to the wind stress observed by [88]. Experiment 2 retains this forcing, but includes a diel light cycle. Experiments 3 through 6 examine the sensitivity of the ITW and subsequent biological responses

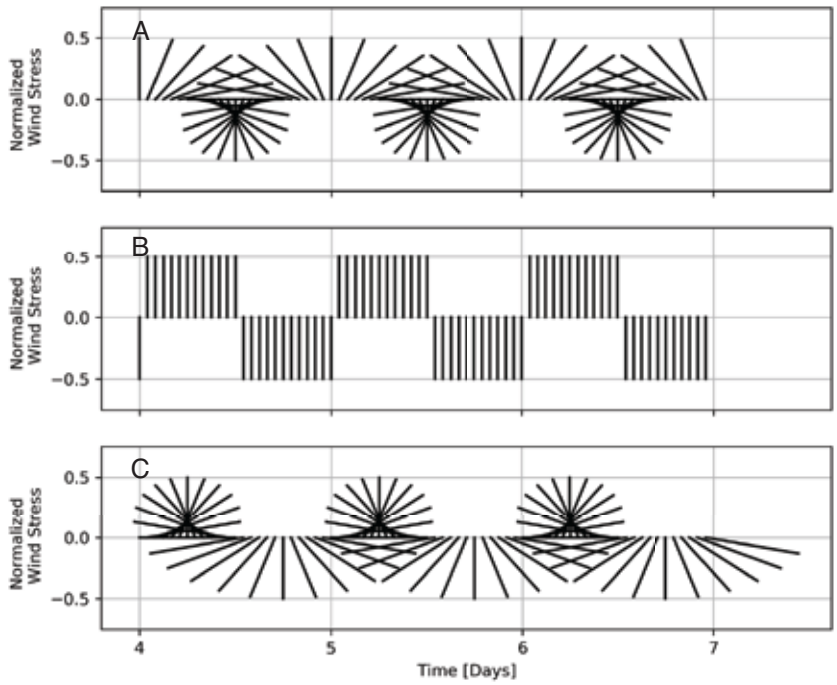

Figure 3.2: Examples of normalized homogeneous wind stress vectors scaled to a maximum amplitude of 0.5 considered in the study: the base configuration with clockwise rotational wind (A), unidirectional land-sea breeze (B), and counterclockwise rotational wind stress (C).

by scaling the amplitude of rotational wind stress by factors of 0.1, 0.2, 0.5, and 1.5, respectively. Additionally, I simulate a polarized land-sea breeze by adjusting the forcing structure to unidirectional wind stress oriented in the u-direction with zero stress in the $v-$direction (Fig. 3.2B). In such a land-sea breeze case, wind stress sustains its peak value for ten hours, which then reverses direction over four hours, resulting in a period of 24-hours. In the final experiment, rotational wind stress is applied in the counterclockwise direction, opposite to the direction of the propagation of the ITW (Fig. 3.2C). Each numerical experiment is integrated for six days, with days four through six as the analysis period.

Table 3.2: List of forcing and light scenarios considered in the island trapped wave study. Wind amplitudes are reported as wind speed at ten meters above sea level. Each experiment is conducted in a domain with an island and reference domain without an island.

Experiment	Wind Structure	Wind Amplitude	Light Scenario
Exp. 1 (Base)	Clockwise Rotational	5 [m s^{-1}]	Constant
Exp. 2	Clockwise Rotational	5 [m s^{-1}]	Diel
Exp. 3	Clockwise Rotational	0.5 [m s^{-1}]	Diel
Exp. 4	Clockwise Rotational	1.0 [m s^{-1}]	Diel
Exp. 5	Clockwise Rotational	2.5 [m s^{-1}]	Diel
Exp. 6	Clockwise Rotational	7.5 [m s^{-1}]	Diel
Exp. 7	Land-Sea Breeze	5 [m s^{-1}]	Diel
Exp. 8	Counterclockwise Rotational	5 [m s^{-1}]	Diel

3.3.4 Model Diagnostics

3.3.4.1 Biological Tracer Fields

To identify the effect of the ITW on biological fields, I compare tracers fields as a percent difference (d) from a reference location far from the influence of the ITW,

$$d = \frac{b_{ITW} - b_{ref}}{b_{ref}} \cdot 100\% \tag{3.7}$$

where b_{ITW} is the state of any biological tracer b near the island, where the amplitude of the ITW is largest. The reference value, b_{ref}, is taken 15 km northeast of island coast, far from the influence of the ITW. This approach highlights how biological fields change relative to a reference evolving with wind forcing away from the island rather than from the initial state.

3.3.4.2 Passive Tracer

In this study I include a passive tracer, s, to track how ITWs redistribute biological fields. I choose to initialize s with a similar profile to the nutrient field, but with a constant slope so that variations in the vertical distribution result from the velocity field, and not variations in the tracer gradient. Figure 3.1B shows the initial condition (grey dashed line) and final state (grey dotted line) of the passive tracer from the reference run without an ITW. The budget for s is constructed as:

$$\underbrace{\frac{\partial s}{\partial t}}_{s_{Rate}} = \underbrace{-\nabla \cdot (s\boldsymbol{u})}_{s_{AFD}} + \underbrace{\underbrace{K_V \frac{\partial^2 s}{\partial z^2}}_{\text{Vertical mixing}} + \underbrace{K_H \nabla^2 s}_{\text{Horizontal mixing}}}_{s_{Diff}}, \tag{3.8}$$

where u is the three dimensional velocity vector, and K_V and K_H are the vertical and horizontal diffusivity constants, respectively. Because s is unaffected by biological processes, exact budgets are constructed from the online model diagnostic output to evaluate the relative roles of advection or diffusion responsible for tracer redistribution.

Online diagnostic variables in ROMS track the exact values for the terms in equation 3.8. The term on the left hand side of equation 3.8 is the time rate of change, or s_{Rate}. The first term on the right hand side is the advective flux divergence, s_{AFD}, the sum of the last two terms are the diffusive flux divergence, s_{Diff}. Where imbalances between s_{AFD} and s_{Diff} exist, s_{Rate} is non-zero, indicating a net gain or loss at particular depths. With the diagnostic variables I can represent the tracer at any time as

$$s(t_j) = s(t_0) + \sum_{i=1}^{j} (s_{rate,j}(t_i)\Delta t), \tag{3.9}$$

where $s(t_j)$ is the value of tracer s at time j, $s(t_0)$ is the initial value, and Δt is the time step. From this, it will be convenient to characterize the average tracer deviation from start of the analysis, given by

$$\langle s(t_j)\rangle - s(t_0) = \underbrace{\frac{1}{m}\sum_{j=1}^{m}\underbrace{\sum_{i=1}^{j}(s_{rate,j}(t_i,m)\Delta t)}_{\text{Time integration}}}_{\text{Spatial average}} \tag{3.10}$$

where the right hand side is the average of the cumulative sum of the diagnostic variable over locations m. This value averages over high frequency changes of the tracer field at all points in time.

3.3.4.3 Primary Production Decomposition

In the ecosystem model used in this study, primary production (first term on the right hand side of eqn. 3.6b) is a function of phytoplankton biomass (P), nutrient level (N), and light availability (I). The combination of these three fields controls the primary production response. Relative contributions of these drivers are diagnosed by decomposing the components contributing to primary production into average and fluctuating terms:

$$P = \underbrace{\langle P\rangle}_{\text{Time mean}} + \underbrace{P'}_{\text{Fluctuation}} \tag{3.11a}$$

$$N = \langle N\rangle + N' \tag{3.11b}$$

$$I = \langle I\rangle + I' \tag{3.11c}$$

where the angled brackets indicate the time-mean and the prime notation indicates the fluctuation or deviation from the mean. Individually, the average of a fluctuating term

is identically zero. However, the product of two or more fluctuating terms may not be zero due to the correlation in the values. Inserting terms in equations 3.11 into the primary production equation (first term in eqn. 3.6b) yields:

$$\langle PP \rangle = \left\langle \frac{V_m}{I_0} e^{k_{ext} z} (\langle P \rangle + P') \frac{(\langle N \rangle + N')}{k_s + (\langle N \rangle + N')} (\langle I \rangle + I') \right\rangle. \tag{3.12}$$

In the experiments considered here, the amplitude of N' is two orders of magnitude less than the average N, allowing us to neglect the fluctuating term in the denominator of the uptake term and to group constant terms as

$$\alpha = \frac{V_m}{I_0 (k_s + \langle N \rangle)} e^{k_{ext} z}. \tag{3.13}$$

With this approximation, average primary production simplifies to:

$$\langle PP \rangle = \left\langle \underbrace{\left\langle \alpha \langle N \rangle \langle P \rangle \langle I \rangle \right\rangle}_{PP|_{\langle N \rangle, \langle P \rangle}} + \underbrace{\left\langle \alpha (\langle P \rangle N' I' \rangle + \langle P' \langle N \rangle I' \rangle + \langle P' N' \langle I \rangle \rangle + \langle P' N' I' \rangle \right\rangle}_{PP|_{N', P', I'}} \right\rangle \tag{3.14}$$

which expresses average primary production as the sum of two average quantities. The first average, $PP|_{\langle N \rangle, \langle P \rangle}$, is the primary production that would occur for the time-averaged concentrations of P, N, and I. This term specifically excludes the effect of phasing with the diel light cycle because the average surface irradiance, $\langle I \rangle$, is equal to the daily surface light average, I_0.

The second average in equation 3.14, $PP|_{N', P', I'}$, represents primary production due to the correlated fluctuating terms N', P', and I', with four governing terms.

Terms that contain an average, such as $\langle\langle P\rangle N'I'\rangle$, represent the adjustment of primary production by the correlation between two fluctuating variables, here, nutrient fluctuations, N', and surface irradiance fluctuations, I'. The last component, $\langle P'N'I'\rangle$, represents the combined triple correlation between fluctuations of all three variables.

3.4 Results

3.4.1 Physical Characteristics of an Island Trapped Wave

In the base configuration (Exp. 1) with homogeneous wind forcing that rotates clockwise with a 24-hour period (Fig. 3.2A), the resonant response of the system generates an Island Trapped Wave (ITW). In order for the wave to remain in resonance, stratification must also remain reasonably unchanged over the six day integration period (eqns. 3.3 and 3.4). To track the evolution of stratification over time, I examine the maximum buoyancy frequency, N^2, (Fig. 3.3A, black dashed line) at the western wall of the island adjacent to the red star in Figure 3.3B. The maximum N^2 fluctuates as the wave moves past this location, but there is no clear trend, indicating that the wave remains in resonance throughout the analysis time period.

The ITW propagates as a nonlinear wave with a large temperature front extending away from the island. Figure 3.3B shows a snapshot of temperature at the 23 m depth level on 12 noon on model day four, the first day of the analysis period. At this time, the west side of the island experiences anomalously low temperatures with higher temperatures on the east of the island. In time, this pattern rotates around the

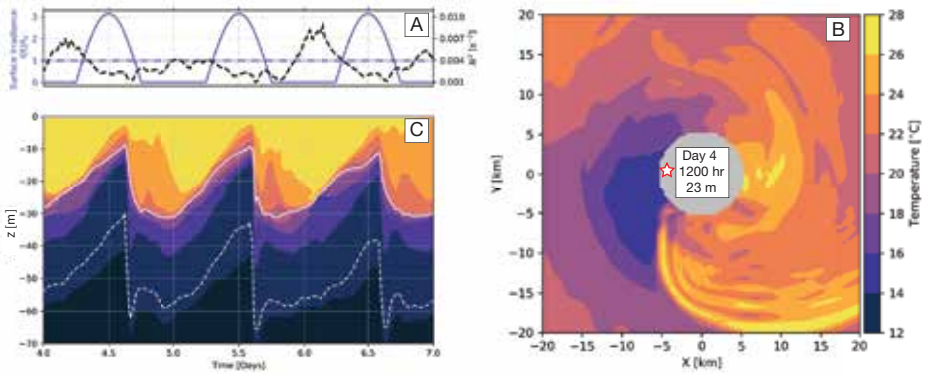

Figure 3.3: Time series of constant light (A, blue dash-dot line) and diurnal light (A, blue line) are shown over the analysis period, model day four through day six, along with Buoyancy Frequency, N^2 (black line). The spatial characteristics of the island trapped wave are shown as a snapshot of temperature at 23 m depth on 1200 hrs of first day of the analysis period (B), and a time series of temperature with the depths of the 21.0°C (solid line) and 14.2° (dashed line) isotherms (C) adjacent to the red star in B.

island in a clockwise sense with a 24-hour period. Figure 3.3C shows how temperature evolves over the analysis period at the western wall of the island adjacent to the red star in Figure 3.3B. The white contours highlight the uneven phase distribution of the wave around the island by showing a time series of the thermocline core depth, 21.0°C (solid line), and thermocline base, 14.2°C (dashed line). From this perspective, isotherms gradually shoal over approximately 12 hours before rapidly deepening over a 30 minute window.

3.4.2 Constant Light and Phytoplankton Response to an Island Trapped Wave

Figure 3.4 shows the average percent difference of the nutrient, phytoplankton biomass, and primary production under constant light relative to the reference location

15 km northeast of the island coast. At 23 m, the initial depth of the thermocline core, the ITW increases nutrients, phytoplankton biomass, and primary production above the reference case. Spatially averaged deviations from the reference location (eqn. 3.7), show that the ITW causes an increase of nutrients by 6.1%, phytoplankton biomass by 0.8%, and primary production by 5.4% (Fig. 3.4A-C). At depths below the thermocline the magnitude of the response is larger. At 40 m depth, the ITW causes an average increase of nutrients by 20.5%, phytoplankton biomass by 1.6%, and primary production by 15.9% (Fig. 3.4D-F). Under constant light, the ITW increases nutrient availability, increasing phytoplankton biomass and enhancing primary production, an effect in our experiment that is more substantial below the thermocline than within it.

The spatial patterns in Figure 3.4 suggest the possible mechanism leading to greater levels of primary production. The ITW causes an approximately uniform increase of nutrients, phytoplankton biomass, and primary production around the island, which is confined to approximately 5 km from the island coast at both 23 m and 40 m depth. Coefficients of determination (R^2) between the percent difference of nutrients and primary production are 0.998 and 0.997 at 23 m and 40 m depth, respectively. In contrast, R^2 between phytoplankton biomass and primary production are 0.720 and 0.668 at 23 m and 40 m depth, respectively.

In order to attribute a mechanism through which the ITW affects primary production under constant light, I apply the primary production decomposition metric (eqn. 3.14). Figure 3.5A shows a cross-section west of the island of the time-average primary production, $\langle PP \rangle$. Figure 3.5B shows $PP_{\langle N \rangle, \langle P \rangle}$, the level of primary production

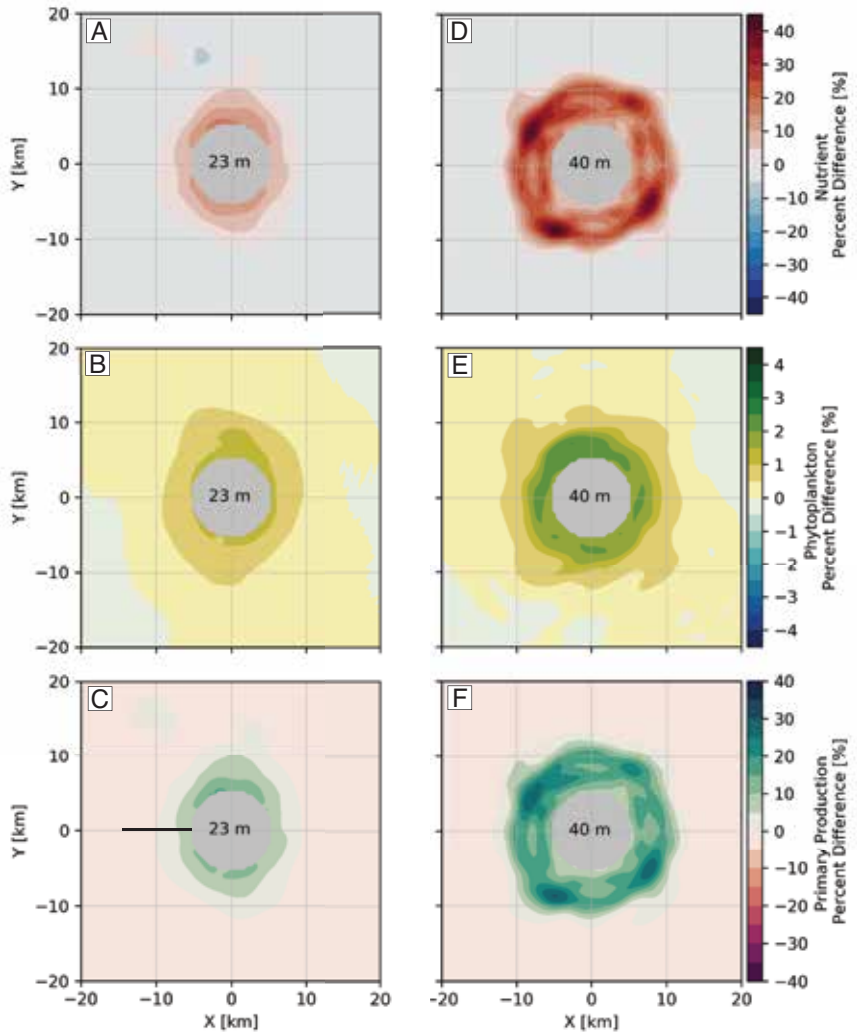

Figure 3.4: Time-averaged percent differences relative to a reference location 20 km from the island center of the nutrient, phytoplankton biomass, and primary production at at 23 m depth (A-C; left column) and 40 m depth (E-F; right column). Horizontal line in C shows the location of the transect of primary production in the discussed in the text.

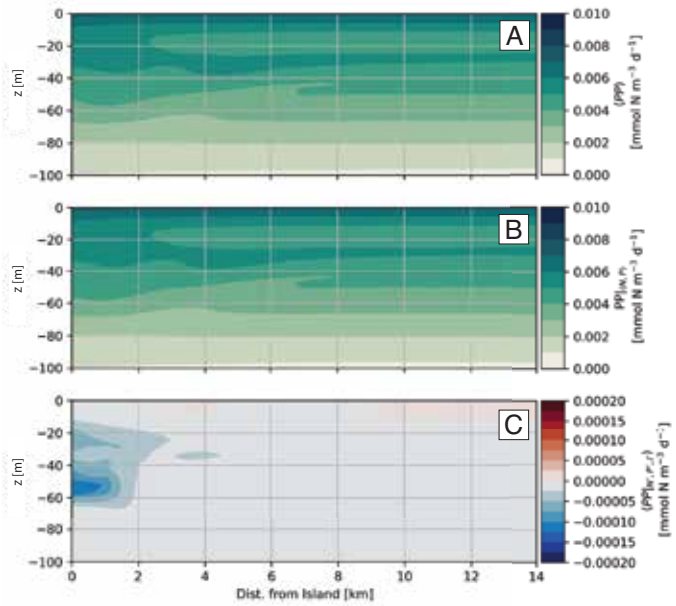

Figure 3.5: Average primary production in the constant light case (A) decomposed into the primary production at the average nutrient and phytoplankton concentrations (B), and the primary production driven by correlated fluctuations of nutrients and phytoplankton biomass (C).

that would occur for time-averaged nutrient and phytoplankton biomass concentrations, which specifically excludes light availability. In this case, $\langle PP \rangle$ is roughly equivalent $PP|_{\langle N \rangle, \langle P \rangle}$. Figure 3.5C shows $\langle PP|_{N',P',I'} \rangle$ is small and negative indicating that correlations between fluctuating nutrient and phytoplankton biomass have a negligible effect on average primary production. These results show that under constant light conditions, the ITW enhances primary production by adjusting the average nutrient and phytoplankton biomass levels.

3.4.3 Diagnostic Tracer Budget

The ITW redistributes nutrients through a combination of advective and diffusive flux divergences, which can be assessed with diagnostic fields of a passive tracer unaffected by biological processes. The passive tracer in this study is initialized with a linear profile at the start of the run to begin with a constant $\frac{ds}{dz}$. Figure 3.6 shows diagnostic budget profiles calculated according to equation 3.10 for two regions: (A) the reference location 20 km from the island center and (B) spatially averaged azimuthally around the island and radially within 5 km from the coast. At both locations, the diagnostic tracer budget is integrated from the beginning of the run such that $s(t_0)$ in equation 3.9 is the initial condition, and the temporal average is then calculated over the three-day analysis period.

Far from the island where tracer fields are unaffected by the ITW (Fig. 3.6A), the advective flux divergence, s_{AFD}, is near zero at all depths such that the diffusive flux divergence, s_{Diff} (red dashed line), governs the tendency, s_{Rate} (black line). In the upper 10 m of the water column, elevated s_{Diff} leads to a gain of tracer sourced from losses near the thermocline top, between 10 m and 23 m depth. A net gain of tracer near the thermocline base extends to 35 m depth, which diffuses from both above and below. At deeper depths, non-zero s_{Diff} results from diffusive flux near the bottom, presumably due to bottom stress.

In contrast, near the island where the ITW is active, Figure 3.6B shows that both advective and diffusive terms are substantial. I note that s_{Diff} results entirely from

vertical diffusion, whereas s_{AFD} results from both horizontal and vertical transfers. Diffusion is largely responsible for supplying and redistributing material above 10 m depth. Deeper in the water column is a complicated exchange of both positive and negative diffusive and advective divergences, though with positive net sum (s_{Rate}) down to 85 m depth and indicating an accumulation of s in time at these depths. Near bottom, vertical diffusion redistributes material up into the water column. The vertical integral of s_{Rate} crosses zero at about 40 m depth (Fig. 3.6C), and remains positive above this depth, indicating that s supplied from near bottom is exhausted at about this depth and additional supply of s above must derive from the horizontal advective flux divergence, then redistributed vertically by both vertical advective and diffusive processes.

3.4.4 Diel Light and the Phytoplankton Response to an Island Trapped Wave

Experiment 2 includes a diel light cycle, which modifies the ecosystem response due to the phasing of the upwelling signature of the ITW and the light cycle. Spatially averaged deviations from the reference location (eqn. 3.7), show that within the thermocline core the ITW causes relative increases of 6.2% for nutrients, 0.8% for phytoplankton biomass, and 5.4% for primary production (Fig. 3.7A-C). Below the thermocline at 40 m depth the average increases in nutrients, phytoplankton biomass, and primary production are 20.5%, 1.6%, and 16.5%, respectively (Fig. 3.7D-F). The average enhancement is similar between constant and diel light cases suggesting that the controlling mechanism is not predominantly determined by the light cycle.

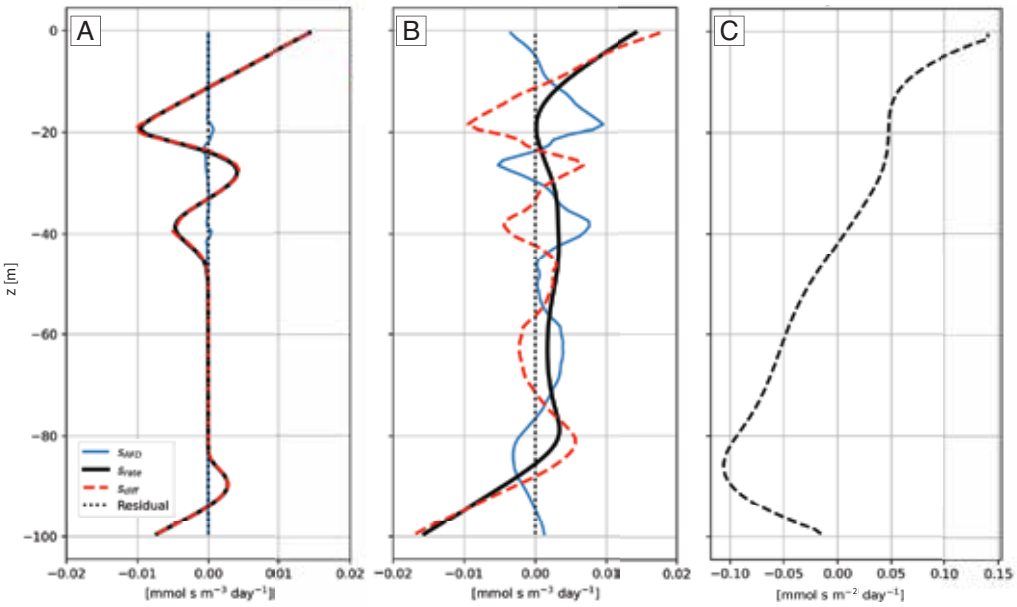

Figure 3.6: Diagnostic tracer budget at the reference location 20 km from the island (A) and spatially averaged budget within 5 km of the island coast (B) showing the sum of vertical and horizontal advective flux divergence (s_{AFD}, blue line), the sum of vertical and horizontal diffusion (s_{Diff}, red dashed line), the time rate of change (s_{Rate}, black line). The residual of the flux and diffusive terms from the rate is shown as the dotted line. Cumulative vertical integral of s_{Rate} is shown as the black dashed line in (C).

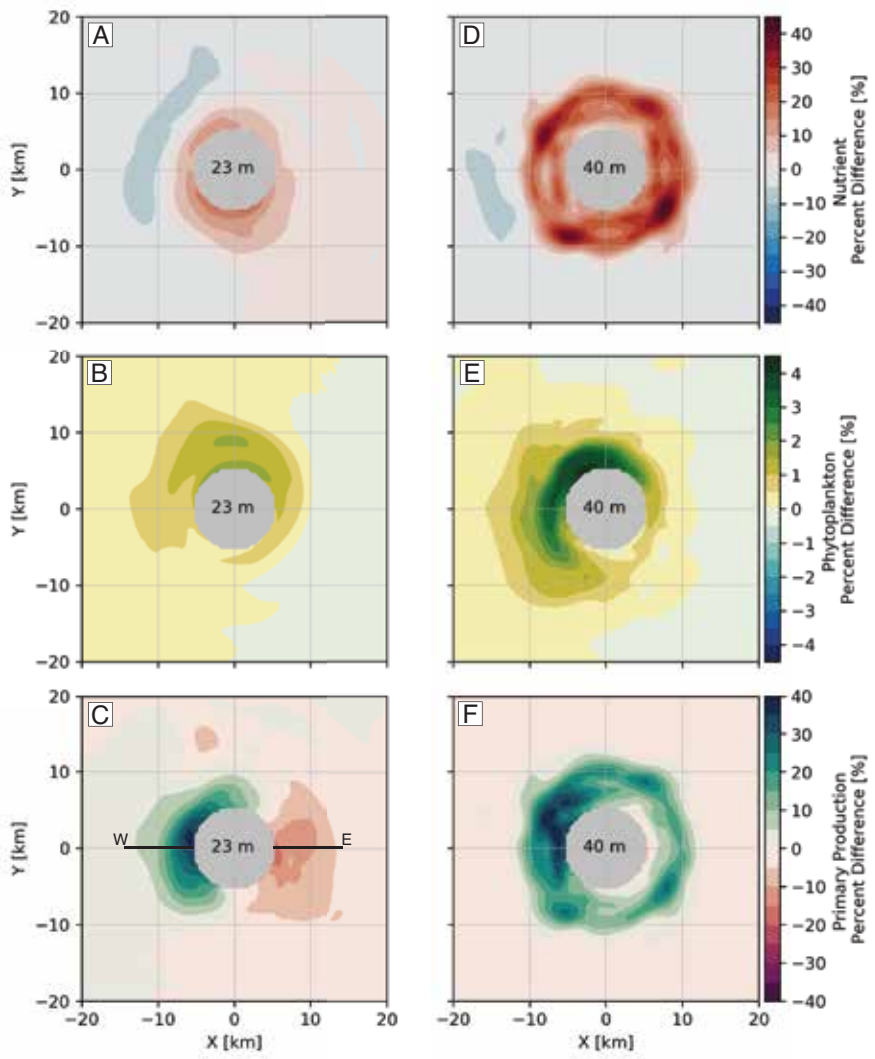

Figure 3.7: Time-averaged percent differences from a reference location 20 km from the island center at 23 m depth (left column) and 40 m depth (right column) for the nutrient (A, D), phytoplankton (B, E), and zooplankton (C, F) for the diel light scenario. Blank lines in C show the location of east and west primary production transects discussed in the text.

The most noteworthy effect of the diel light cycle is on the spatial distribution of phytoplankton biomass and primary production anomalies from the reference location. The diel light cycle increases the range and spatial pattern of anomalies. At 23 m depth in the constant light case maximum phytoplankton biomass and primary production anomalies are 1.3% and 16.5%, respectively, whereas these values are near double for the diurnal light case, reaching 2.1% and 36.5%, respectively. Similarly, minimum anomalies are reduced in the diel light case. At 23 m depth, the largest reduction of primary production is -1.5% in the constant light case, while in the diel case the maximum reduction is -19.8%. Spatially, the larger range of anomalies manifests as an uneven distribution of phytoplankton biomass and primary production anomalies. At both 23 m and 40 m depth large positive anomalies occur on the western side of the island where the diel light cycle is in-phase with the ITW, meaning that light intensity is largest where the pycnocline and accompanying nutrient values are shallow. Negative, or small positive anomalies occur on the eastern side of the island where the diel light cycle is out-of-phase with the ITW (Fig. 3.7). By including diel light, total range of phytoplankton biomass and primary production anomalies from the reference cases become larger, leading to asymmetries in productivity around the island.

To identify the factors influencing primary production in the diel light case, I apply the primary production decomposition metric (eqn. 3.14). Figure 3.8A shows a transect of $\langle PP|_{N',P',I'}\rangle$ on the eastern side of the island, where the nutrient upwelling associated with the ITW is out-of-phase with the diel light cycle. Here, the negative $\langle PP'\rangle$ is related to the phasing of the ITW and light cycle, which suppresses

the time-average primary production. The relative magnitudes of the components of $\langle PP' \rangle$ show that the correlation between nutrient and light fluctuations, $\langle \langle P \rangle N' I' \rangle$, drives this response. In contrast, Figure 3.8B shows a transect on the western side of the island where the diel light cycle is in-phase with the upwelling associated with the ITW. Here, the positive values of $\langle PP' \rangle$ indicate that correlations between phytoplankton biomass, nutrient levels, and light availability combine to enhance primary production. In this case, $\langle \langle P \rangle N' I' \rangle$ is a large positive, acting to enhance average primary production showing that spatial patterns of primary production are driven by the correlation in fluctuating light and nutrient fields. This correlation suppresses primary production on the eastern side of the island and enhances primary production on the western side. The phasing of the diel light cycle with the nutrient upwelling associated with the ITW drives the asymmetry of the primary production response.

Figure 3.8B shows the region where the ITW enhances primary production due to correlation between nutrient and light fluctuations. The most considerable enhancements are within three kilometers from the island coast and between 10 and 50 m depth. At depths shallower than 10 meters, primary production enhancement is restricted by small nutrient fluctuations, $N'(t)$ from equation 3.11B. At depths deeper than 50 m, primary production enhancement is restricted by small light fluctuations due to exponential light attenuation. Between these depths, there are two peaks of primary production enhancement near the island coast: a shallow maximum near 23 m depth and a deeper maximum near 40 m depth. At 40 m depth, primary production is light limited, and growth here is enhanced by the light cycle, $I'(t)$. At 23 m, growth is

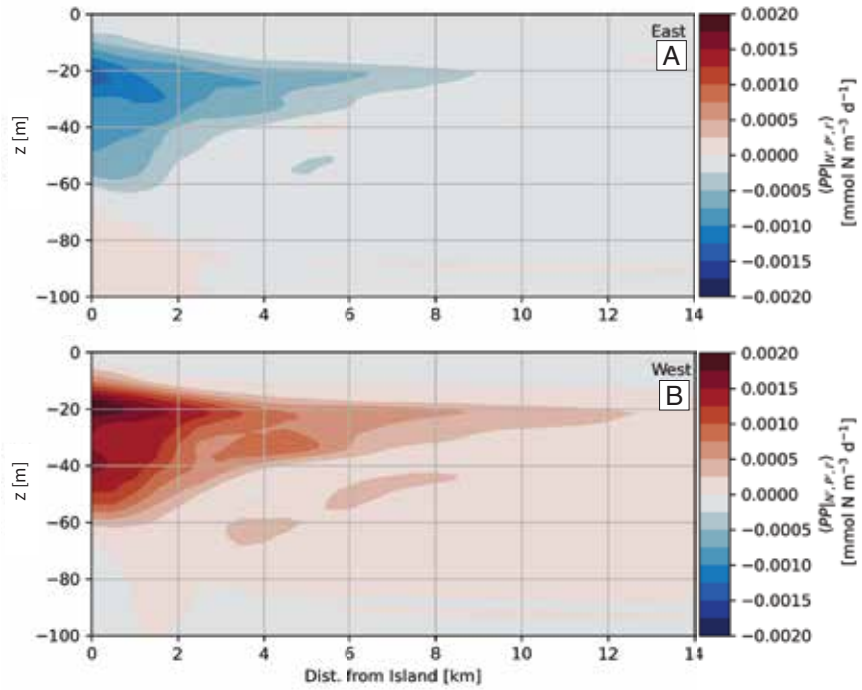

Figure 3.8: Primary production through correlated fluctuations of light, nutrient, and phytoplankton concentrations for the diel light scenario. The cross section east of the island (A) is at a location where the upwelling associated with the island trapped wave is out-of-phase with the diel light cycle. The cross section west of the island (B) is a location where the upwelling associated with the island trapped wave is in-phase with the light cycle.

nutrient-limited, making primary production enhancements more sensitive to changes in N'. However, at all depths, regardless of whether growth is limited by light or nutrients, primary production is enhanced where $I'(t)$ is in phase with changes of $N'(t)$ driven by the ITW propagation.

3.4.5 Sensitivity Experiments

3.4.5.1 Wind Forcing Magnitude

I assess the effect of wind stress magnitude on the ITW and the subsequent ecosystem response by scaling the magnitude of rotational wind stress in the base configuration presented above. The magnitude of rotational wind stress in Figure 3.2A is scaled by factors of 0.1, 0.2, 0.5, and 1.5, Experiments 3 through 6, respectively. Figure 3.9A shows the depth of the thermocline core, 21.0°C, for each case of wind stress at the western wall of the island adjacent to the red star in Figure 3.3B. As the magnitude of wind stress increases, so does the amplitude of displacement of the thermocline core. At the lowest level of wind stress, the ITW propagates approximately as a linear, near sinusoidal wave. As wind stress increases, the ITW becomes nonlinear, with a sawtooth-like pattern and a sharp downwelling wavefront as described above.

A diel light cycle was included in each sensitivity study, allowing us to examine the combined effects of the ITW propagation and the light cycle. Figure 3.9B shows that the nutrient concentration on the 21°C isotherm oscillates in each forcing scenario due to the light cycle. However, the amplitude of the nutrient oscillation becomes larger in scenarios with higher wind stress, indicating that advective and diffusive divergences that elevate nutrients near the island at these depths increase with ITW amplitude. At the thermocline base, flux divergences result in a linear decline in the depth of the 14.2°C isotherm across all forcing scenarios (Fig. 3.9C). Figure 3.9D shows that the nutrient level on the 14.2°C is sensitive to magnitude of wind stress. At the two highest wind

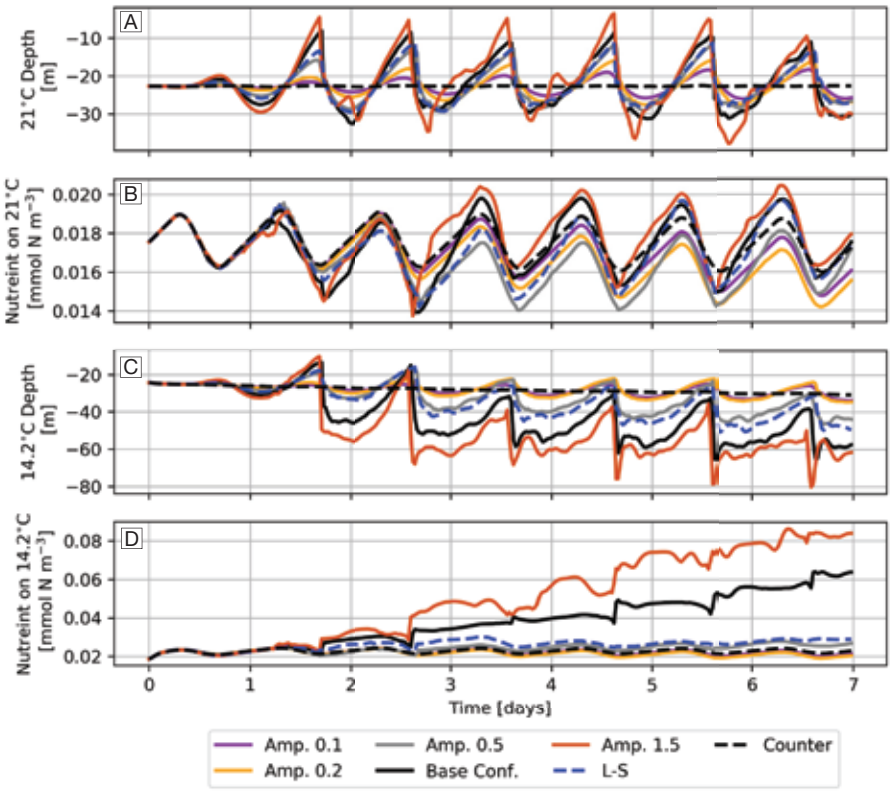

Figure 3.9: Time series of the 21°C isotherm depth (A), nutrient concentration on the 21°C isotherm (B), 14.2°C isotherm depth (C), and nutrient concentration of the 14.2°C isotherm (D). Each example includes diel light. Each panel includes the base configuration (black) and sensitivity studies with rotational wind stress scaled by 0.1 amplitude (purple), 0.2 amplitude (gold), 0.5 amplitude (grey), and an amplitude of 1.5 (red). The land-sea breeze (L-S) case is shown as the dashed blue line and the counterclockwise rotational wind case is shown as the dashed black line.

stress scenarios, the sharp deepening of isotherms by the passing wavefront is associated with a bolus of nutrients. In scenarios with lesser wind stress, nutrient oscillations are driven primarily by biological exchanges associated with the diel light cycle. The largest potential primary production enhancement occurs where the nutrient delivery by the ITW is in-phase with the light cycle.

3.4.5.2 Structure of Wind Forcing

The temporal characteristics of the wind-forcing structure can affect the ITW response. All results shown thus far consider the base configuration with homogeneous rotational wind stress (Fig. 3.2A). An alternative is a larger scale, unidirectional land-sea breeze resulting from a nearby coast (e.g., Croatia), modeled as a modified sine wave a 24-hour period, reversing direction over four hours and reaching a maximum sustained amplitude equivalent to that in Experiment 1 (Fig. 3.2B). This wind structure does support the generation of an ITW, with the amplitude of isotherm displacement smaller than the base configuration for both the 21°C and 14.2°C isotherms (Fig. 3.9A, C). In particular, the maximum depth of the 14.2°C isotherm is shallower for the unidirectional land-sea breeze forcing scenario (blue dashed line) compared to the base configuration (black line), causing less nutrient mixing into the base of the thermocline (Fig. 3.9D). The magnitude of the ITW response is smaller in the unidirectional land-sea breeze case than in the base configuration because the integrated wind's projection onto the wave's phase propagation direction is less. The idealized rotational wind perfectly reinforces the ITW throughout the 24-hour period. In the case of a unidirectional land-sea breeze,

perfect reinforcement occurs only twice in this period as it changes direction. These experiments show that a unidirectional land-sea breeze supports ITW generation, indicating that it is the forcing period, not the combination of wind components, that is essential.

There is one exception where a 24-hour forcing period does *not* produce an ITW. Experiment 8 is a scenario where homogeneous wind rotates counter to the direction of the ITW propagation, as a result no ITW is formed. Figure 3.9A shows that the depth of the 21°C isotherm is constant for this simulation (black dashed line). Similarly, the thermocline base does not oscillate and that it declines linearly due to weak vertical mixing (Fig. 3.9C). Although advective and diffusive processes cause a linear decline in the 14.2° depth, it is less substantial than in cases where an ITW exists. Nutrient levels on the 21.0°C and 14.2°C isotherms oscillate despite no ITW, confirming the variability is due to biological processes associated with the diel light cycle. The absence of the ITW in response to counter-rotating wind illustrates a particular example of how the structure of wind forcing can affect ITW formation.

3.4.5.3 Statistical Summary of Biological Responses to Island Trapped Waves

Figure 3.10 summarizes the biological response to different light and wind forcing scenarios explored in this study with box plots of average anomalies of nutrients, phytoplankton biomass, and primary production. By comparing the constant light case (1^{st} box plot) to the diel light cycle case (2^{nd} box plot), I see variable light has little effect on nutrient (Fig. 3.10A, D) though it increases the range of phytoplankton biomass

(Fig. 3.10B, E) and primary production (Fig. 3.10C, F) at both 23 m and 40 m depth. When the magnitude of rotational wind stress increases by a factor of 1.5 (3^{rd} box plot), average anomalies increase for nutrients, phytoplankton biomass, and primary production at 23 m. A similar enhancement of nutrients occurs at 40 m depth, but to a lesser extent for phytoplankton biomass and primary production. As the magnitude of rotational wind stress decreases (4^{th}-6^{th} box plot), the average percent difference between the experimental and reference runs becomes small, indicating that there may be a minimum threshold of wind stress needed to excite a meaningful biological response. The land-sea breeze case (7^{th} box plot) shows more enhancement at 40 m depth than at 23 m depth. The counter rotational wind case (8^{th} box plot) shows very little difference between experimental and reference runs, highlighting that there is no ITW in this case.

3.5 Discussion

Baroclinic waves, such as island trapped waves (ITW), simultaneously affect nutrient and light availability for primary production. Baroclinic waves alter nutrient levels through convergences and divergences in advective and diffusive fluxes. I find that horizontal advective fluxes enhance nutrient levels near the island that are then redistributed vertically by both advective and diffusive processes. In addition, baroclinic waves move water parcels, and thus phytoplankton, through a light field that varies exponentially in the vertical, exposing them to higher average levels of light [49]. By identifying the relative contributions ITWs make to light and nutrient availability

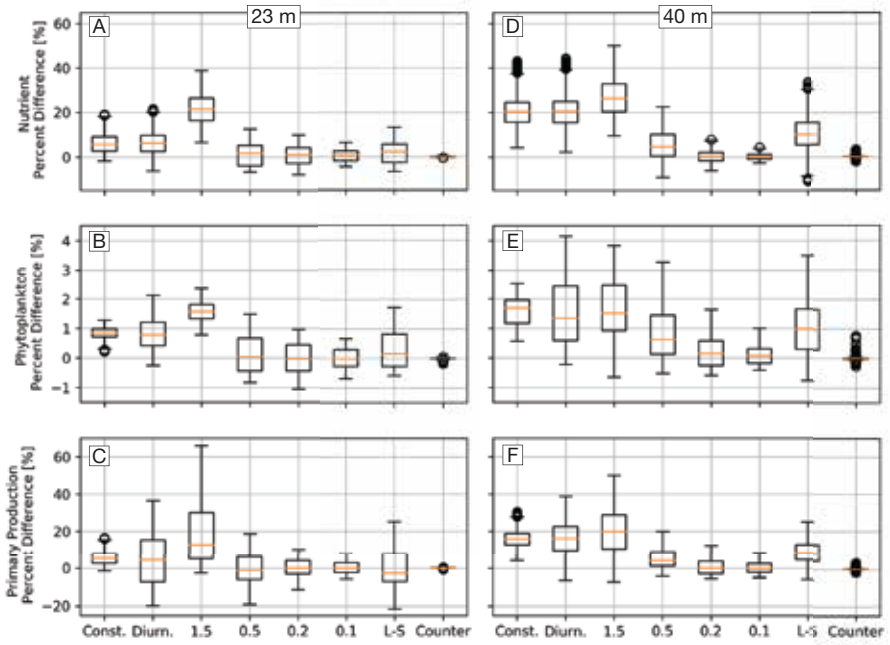

Figure 3.10: Box plots summarizing percent differences between the ITW region and the reference location at 23 m depth for the nutrient (A), phytoplankton biomass (B), and primary production (C). Panels D-F are for the same values at 40 m depth. Experiments include rotational wind with constant light (Const.) and diel light (Diurn.). Experiments with amplitude adjustment by a factors of 1.5, 0.5, 0,2, and 0.1, the land-sea breeze (L-S) case, and the counterclockwise rotational wind (Counter) case all include the diel light cycle.

in idealized models, I have defined and quantified how these waves support the local baseline of marine ecosystems at locations where they occur. The degree to which the ITW increases nutrients determines the magnitude of the primary production response, while the phasing of the ITW with the light cycle controls the spatial pattern.

In real systems, such as the Island of Lastovo in the Adriatic Sea, ITWs occur when seasonal stratification causes the system's natural frequency to match the 24-hour cycle of the land-sea breeze [88, 66]. In nature, radiative fluxes varying with the diel light cycle drive the land-sea breeze. Because the orientation of the land-sea breeze in relation to the island is fixed, the phase-locked nature of the forcing with the ITW response should lead to a consistent location of enhanced primary production during times when ITWs are present. This example and our study consider a system with exactly a 24-hour period. For islands with slightly longer periods, such as Bermuda with a 26.1-hour natural period [123, 42, 7], the ITW will increase nutrient delivery, but the phasing with the light cycle should cause the location of enhanced primary production to precess around the island. In the case of ITWs that resonate at much longer periods than 24 hours, such as the island of Hawai'i with a 59-hour period [77], the ecosystem may respond to elevated nutrient levels, but the phasing with the light cycle will likely have a minimal effect.

It is worth noting that in the biological model used in this study, the response of primary production to light amplitude at all depths is linear, while the response to nutrient concentration is a saturating functional response (first term in eqn. 3.6b). Increases in nutrient levels do not necessarily translate to a proportional response of

primary production because the response depends on the nutrient level relative to the half-saturation value, k_s. On the other hand, increases in light availability, whether due to vertical motion or the diel light cycle, will always lead to an increase in primary production, as there is no saturating response to light. If a nonlinear photosynthesis-irradiance function were to be used in place of a linear one, the strength of the primary production response would depend also on the light level relative to the saturation parameter.

3.5.1 Summary: Island Trapped Waves Enhance Primary Production

Wind-driven island trapped waves increase phytoplankton biomass and primary production through net horizontal and vertical flux divergences of nutrients near the island. Experiments with constant light show a high level of coherence between elevated nutrients and enhanced primary production at all locations around an idealized island (fig. 3.4). Though nutrients become elevated in time by the ITW over most depths, the primary production response is larger in our experiments below the initial depth of the thermocline than within it because of a combination of ITW-induced supply and background levels (figs. 3.1; 3.4; 3.7;3.6). Experiments with a diel light cycle create an uneven spatial distribution of primary production and phytoplankton biomass around the island, with the largest enhancement occurring where the upwelling phase of the ITW occurs during daylight hours (figs. 3.3; 3.7). The magnitude of the biological response is sensitive to the amplitude of wind forcing; simulations with weak wind stress do not cause a sufficiently large advective flux divergence to stimulate a

substantial primary production response, and a larger amplitude response occurs with larger ITW fluctuations, as stimulated by stronger winds.

Chapter 4

Nutrient Sources and Primary Production in Wind-driven Upwelling Systems: Comparison of two- and three-dimensional Idealized Simulations

Relative to their surface area, wind-driven coastal upwelling systems are some of the most productive ecosystems in the global ocean due to the delivery of nutrient-rich waters to the euphotic zone, supporting high levels of primary production [68, 80, 79]. Coastal upwelling is driven by the offshore transport of surface waters due to a balance between wind stress and Coriolis acceleration. Deeper waters from below replenish displaced surface waters, delivering nutrient-rich waters to the coast. The magnitude of coastal upwelling is often expressed in terms of lateral surface Ekman Transport:

$$U_E^s = \frac{\tau_s^y}{\rho_0 f} \tag{4.1}$$

which is function of alongshore wind stress, τ_s^y, and the Coriolis parameter, f, and ρ_0 is a reference density. From this relationship, stronger wind stress results in greater offshore transport, and latitudinal variations of wind stress are often used to explain along-shelf variations in primary production [13, 34]. However, the source depth of upwelled waters, is crucial in determining the nutrient content of waters supplied to the euphotic zone. The depth of water that is delivered to the coast depends on shelf geometry in both the cross-shelf [50, 62] and the along-shelf directions [93]. In this work, I aim to connect the influence of cross-shelf and along-shelf geometry to the delivery of nutrient-rich waters to the euphotic zone to better understand the drivers of primary production in wind-driven upwelling systems.

In order to evaluate how shelf geometry affects primary production, it is important to distinguish between the efficiency of nutrient delivery from the physical upwelling of water. I define the efficiency of nutrient delivery as the quantity of nutrients supplied to the euphotic zone for a given wind stress and it is related to the structure of the nutricline. Because nutrients typically increase with depth, deeper source depth for a given wind stress, results in a greater efficiency of nutrient delivery. In contrast, the physical upwelling of water is related to cross-shelf transport by the bottom slope that also influences the position of the upwelling front and the source depth. To analyze this, I follow others by partitioning the upwelling system into four regions: the surface mixed layer, the bottom boundary layer (BBL), geostrophic interior, and the inner shelf.

The upwelling front is the location where cool, recently upwelled waters meet warmer surface waters that existed prior to upwelling. The inner shelf is formed where the surface mixed layer and BBL meet such that the water column is well-mixed [3, 9, 63]. Deeper source depths result from steep slopes and weak stratification [50]. One parameter that embodies key parameters and influences upwelling transport pathways is the topographic Burger Number (S):

$$S = \alpha \frac{N}{f}. \tag{4.2}$$

Here, α is the slope of the continental shelf, N is the buoyancy frequency, and f is the Coriolis parameter. Upwelling over narrow shelves where α and S are relatively large (for a given N and f), results in a greater proportion of BBL water supplied to the euphotic zone. A steep slope also results in a relatively thin BBL, causing the inner shelf and the upwelling front to be located close to shore. In contrast, upwelling over wide shelves, where α and S are relatively small, a greater proportion of water is sourced from the shallower interior and the BBL is relatively thick causing the inner shelf and upwelling front to extend farther from shore [9, 62]. Jacox and Edwards (2011) also showed that high stratification ($N = 0.020$ s^{-1}) results in a relatively shallow source depth, largely insensitive to bottom slope. With weak stratification ($N = 0.004$ s^{-1}), the source depth increases notably with bottom slope.

In three-dimensions, changes in shelf width in the alongshore direction adjust the transport of waters within the BBL and throughout the water column. Pringle, (2002) used a linear, barotropic model to study how wind-driven upwelling is modified

by alongshore variations in shelf width [93]. He found that changes in shelf width only adjust flow in the direction of coastal trapped wave propagation (upwind) over a frictional length scale on the order of 100 km. Flow decelerates where a shelf widens in the direction of upwelling favorable wind. In addition, an imbalance between the offshore surface Ekman transport and the bottom Ekman layer transport intensifies cross-shore transport in the BBL, enhancing nutrient delivery on the shelf. However, Pringle, (2002) specifically noted that there must be some additional mechanism to carry these nutrients into the euphotic zone for the topographically enhanced upwelling to affect primary production. In this work, I connect the adjustment of BBL flow due to changes in alongshore shelf width to the primary production response in the overlying surface waters.

This study considers nutrient supply and the primary production response in two- and three-dimensional numerical simulations of wind-driven coastal upwelling. In section 4.1, I introduce the numerical experiments, ecosystem model, and model diagnostics. Section 4.2.1 describes the physical mechanisms and biological response in two-dimensional simulations of upwelling over a narrow and wide shelf, which sets the context for the three-dimensional simulation presented in section 4.2.2. After outlining the processes that occur over a widening shelf in section 4.2.2.1 and over a narrowing shelf in section 4.2.2.2, I consider how the origins of upwelled water affects primary production downstream in section 4.2.3. Finally, I conclude with a brief discussion that connects predictions by two- and three-dimensional theory in the context of shelf geometry and nutrient supply to the euphotic zone in coastal upwelling systems.

4.1 Methods

4.1.1 Physical Model Configuration

This study conducts numerical experiments using the Regional Ocean Modeling System (ROMS) to simulate wind-driven upwelling in domains configured in two- and three-dimensions. ROMS solves the Boussinesq hydrostatic equations of motion on a regular horizontal grid. Vertically, the ROMS operates on terrain-following $s-$coordinates. In this application, ROMS is configured on an f-plane with a linear equation of motion such that there is no advection of momentum and employs linear drag at the surface and bottom boundaries. I use Mellor-Yamada 2.5 vertical mixing. For further details on ROMS see [106]. Our model configuration is an idealized version of the U. S. West Coast, with a coordinate system (x,y,z) corresponding to (east, west, upward).

4.1.1.1 Forcing

In each numerical model described below, coastal upwelling is driven by north-to-south alongshore wind stress (i.e., directed in the negative y-direction) that is uniform throughout the domain, with zero wind stress curl. I increase wind stress to a maximum of 0.1 Pascals over two days using the first quarter-period of a sine function. After the ramp-up, maximum wind stress is sustained for eight days, with a total simulation duration of ten days. I assess each simulation's physical and biological state on the final day of the simulation.

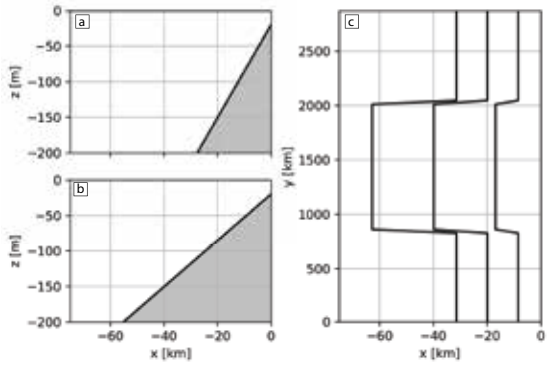

Figure 4.1: Examples of narrow shelf (a), wide shelf (b) in two- and three-dimensional cases. Panel c shows a top-down view of three-dimensional domain with 75 m, 150 m, and 225 m isobaths shown as black lines (right to left).

4.1.1.2 Two- and Three-dimensional Domains

Each model has a resolution of 0.65 km in the cross-shelf direction and 1.0 km in the along-shelf direction. Boundary conditions are periodic along the northern and southern boundaries and are closed on the eastern and western boundaries. In every configuration, a linear shelf slope without a shelf break is constructed along the eastern wall with a minimum depth of 20 m and a maximum depth that varies based on shelf slope configuration (see below). The grid contains 100 vertical levels, which result in a vertical resolution that changes from 8 m over the deepest parts of the domain to 0.2 m near the coastal boundary.

This study considers coastal upwelling in two- and three-dimensional domains. Figure 4.1 shows the two, two-dimensional domains constructed with (a) narrow and (b) wide shelf slope without a shelf break. The wide shelf has a constant slope of 3.2 $\times 10^{-3}$ with a maximum depth of 260 m and the narrow shelf case has a constant slope of 6.4 $\times 10^{-3}$ with a maximum depth of 500 m. Both two-dimensional domains extend

10 km uniformly in the along-shelf direction and 74 km in the cross-shelf direction. Simulations in these two domains serve as a reference to highlight the effect of changing shelf width on source water in the the three-dimensional domain.

The three-dimensional domain is 74 km in the cross-shore direction and 2870 km in the along-shelf direction (Fig. 4.1c). From north to south, the shelf width linearly transitions from a narrow shelf to a wide shelf over a 15 km transition. Then, 1200 km south of where the widening shelf reaches its maximum width, the shelf slope transitions back to the narrow shelf width over a 15 km transition region. Shelf slopes outside of these transition regions are identical to the two-dimensional domains described above. In both the two- and three-dimensional configurations, I prescribe a linear temperature decrease of $2.36°C$ from 20 m to 1000 m depth (Fig. 4.2a, red line), with a constant salinity of 35. This vertical temperature gradient is smaller than typical in nature, and sensitivity studies to stratification will be discussed below. The resulting buoyancy frequency, N, is constant with depth equaling 4.0×10^{-3} s^{-1}, producing a Burger Number of 0.13 over the wide shelf and a Burger Number of 0.26 over the narrow shelf (eqn. 4.2).

4.1.2 Ecosystem Model Configuration

I represent ecosystem dynamics using a simple, nutrient, phytoplankton, zooplankton, detritus (NPZD) model adapted from [32]. This model uses a nitrogen-based currency, with the governing equations written as:

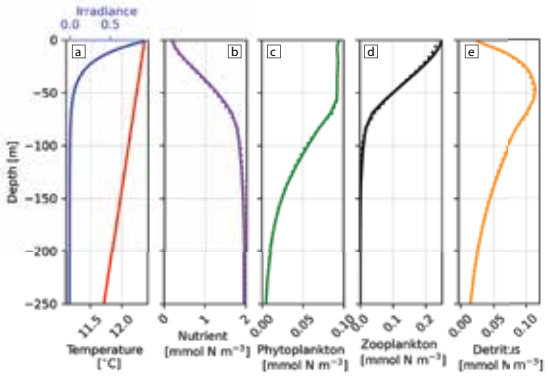

Figure 4.2: Initial conditions of temperature (a; red line), nutrient (b; purple line), phytoplankton (c; green line), zooplankton (d; black line), and detritus (e; gold line). The final conditions for the one-dimensional case is shown for the biological variables and passive tracer as dotted lines in plots b-e. The exponentially varying light profile is shown as the blue line in a.

$$\frac{dN}{dt} = \underbrace{-P\frac{V_m N}{k_s + N}e^{k_{ext}z}}_{\text{N Uptake by P}} + \underbrace{(\beta\frac{R_m P^2}{\Lambda^2 + P^2} + M_n)Z}_{\text{Excretion by Z}} + \underbrace{rD}_{\text{D remin.}} + \underbrace{K_v\frac{d^2N}{dz^2}}_{\text{Vertical Mixing of N}} \tag{4.3a}$$

$$\frac{dP}{dt} = \underbrace{P\underbrace{\frac{V_m N}{k_s + N}}_{\text{Michaelis-Menten Uptake}}\underbrace{e^{k_{ext}z}}_{\text{Light function}}}_{\text{Primary Production (N uptake)}} - \underbrace{\frac{R_m P^2}{\Lambda^2 + P^2}Z}_{\text{Grazing of P by Z}} - \underbrace{mP}_{\text{P Mortality}} + \underbrace{K_v\frac{d^2P}{dz^2}}_{\text{Vertical Mixing of P}} \tag{4.3b}$$

$$\frac{dZ}{dt} = \underbrace{(1-\gamma)\frac{R_m P^2}{\Lambda^2 + P^2}Z}_{\text{Z Assimilation of P}} - \underbrace{M_n Z}_{\text{Z Excretion}} - \underbrace{M_d Z}_{\text{Z Mortality}} + \underbrace{K_v\frac{d^2Z}{dz^2}}_{\text{Vertical Mixing of Z}} \tag{4.3c}$$

$$\frac{dD}{dt} = \underbrace{mP}_{\text{P Mortality}} + \underbrace{(\gamma-\beta)\frac{R_m P^2}{\Lambda^2 + P^2}Z}_{\text{sloppy feeding}} + \underbrace{M_d Z}_{\text{Z Mortality}} - \underbrace{rD}_{\text{D Remin.}} + \underbrace{K_v\frac{d^2D}{dz^2}}_{\text{Vertical Mixing of D}} - \underbrace{\mathrm{w}D}_{\text{Sinking}}. \tag{4.3d}$$

In this form, the left-hand-sides express the rate of change of the nutrient (eqn. 4.3a), phytoplankton (eqn. 4.3b), zooplankton (eqn. 4.3c), and detritus (eqn. 4.3d) as total

derivatives where each field is subject to advection in the Lagrangian reference frame.

I parameterize this model to reflect coastal upwelling systems that typically consist of macrozooplankton grazing on diatoms. Light decays vertically with an attenuation coefficient, k_{ext}, 0.06 m^{-1} (Fig. 4.2a, blue line). Nutrient uptake by diatoms is governed by Michaelis-Menten kinetics with maximum uptake, V_m, set to 2.0 d^{-1} and half-saturation, k_s, set to 0.5 mmol N m^{-3}. Phytoplankton mortality is linear and set to 0.05 d^{-1}. In upwelling systems, I assume zooplankton biomass is largely greater than phytoplankton biomass [115]. I achieve this by setting the maximum zooplankton grazing rate, R_m, to 3.5 d^{-1} with a level of half saturated grazing, Λ, set to 0.4 mmol N m^{-3}, and an efficiency, γ, of 0.15. In addition, I control zooplankton losses by setting the excretion rate, M_n, excretion coefficient, β, and mortality, M_d, to 0.01 d^{-1}, 0.05, and 0.05 d^{-1}, respectively. Detritus remineralizes at a rate, r, of 0.025 d^{-1}, and sinks at a rate, w, set to 2.5 m d^{-1}. A summary of the parameter values, definitions, and units can be found in Table 4.1.

I generate initial conditions for the ecosystem model by first integrating in a one-dimensional (vertical) model for 800 days until a steady state is reached. This is accomplished by initializing profiles of phytoplankton, zooplankton, and detritus with constant values of 0.06 mmol N m^{-3}, 0.08 mmol N m^{-3}, and 0.04 mmol N m^{-3}, respectively, while the initial nutrient profile increases linearly with depth with a slope of 0.02 mmol N $m^{-3}m^{-1}$. By initializing the experimental models with these conditions, any perturbation from this state is due to the imposed physical process rather than a purely biological adjustment of the dynamical system.

Table 4.1: List of definitions, symbols, and values for parameterizations of the ecosystem model.

Parameter	Symbol	Value	Unit
Light Att.	k_{ext}	0.06	m^{-1}
Max. N. Uptake	V_m	2.0	day^{-1}
P. Mort.	m	0.05	day^{-1}
P. Half-sat.	K_s	0.5	N
Max. Z. Gr.	R_m	3.5	day^{-1}
Z. Gr. Eff.	γ	0.15	unitless
Z. Mort.	M_d	0.05	day^{-1}
Z. Excr. Coeff.	β	0.05	unitless
Z. Gr. Sat.	Λ	0.4	N
Z. Excr. Rate	M_n	0.01	day^{-1}
Remin. Rate	r	0.025	day^{-1}
D. Sinking Rate	w	2.5	m day^{-1}

4.1.3 Model Diagnostics

One of the primary goals of this work is to quantify how changes in shelf width affect the source waters delivered to the nearshore region by wind-driven upwelling. Following Cervantes et al., (2003), I approximate the source of upwelled waters from Eulerian fields by initializing three passive tracers with values corresponding to their initial grid position, X(x, y, z, t_0), Y(x, y, z, t_0), Z(x, y, z, t_0) [12]. These tracers are then transported by physical processes in the model, providing an approximation of each parcel's starting location (i.e., source location) at the final time step. It is important to note that this technique gives the approximate source location because these tracers are subjected to diffusion that varies spatially and temporally, and leads generally to an underestimation of source location. However, in their realistic modeling study off of Duck, North Carolina, Cervantes et al., (2003) showed that the passive tracer approach led to a coherent response compared to an explicit Lagrangian tracer approach. I use these passive tracers to reasonably approximate the source depth and location of upwelled waters recognizing that it may underestimate the source depth [12].

Online diagnostic variables in ROMS explicitly compute terms in the momentum equation. I identify the primary momentum balances from the depth-averaged momentum budget and quantify the bottom Ekman Transport. Of particular interest is the cross-isobath bottom Ekman Transport,

$$U_E^b = \frac{\tau_b^{y*}}{\rho_0 f} \tag{4.4}$$

which is similar to equation 4.1, except the bottom stress from the ROMS diagnostic file, τ_b^y*, is used in place of surface stress. τ_b^y* represents the locally along-isobath bottom stress, computed from the eastward and northward components of diagnostic bottom stress, τ_b^x, and τ_b^y, to rotate bottom stress into the local along-isobath direction, τ_b^y*.

Finally, I capture the biological response to upwelling as the change in primary production from the initial condition to the value after ten days of upwelling favorable wind stress, ΔPP. By then vertically integrating ΔPP,

$$\int_{-h}^{0} \Delta PP dz, \tag{4.5}$$

at all positions in the three-dimensional domain I quantify the spatial variability of primary production.

4.2 Results

4.2.1 Two-dimensional Upwelling with a Linear Model

The two-dimensional response of coastal waters to upwelling-favorable wind stress is illustrated by the streamlines (white contour lines) in Figure 4.3 define by $\Psi_z = u$ and $\Psi_x = -w$. Here, the offshore motion of surface waters (a,b; blue contours) is balanced by the onshore motion of deeper waters (a,b; red contours). This dynamic is evident in both the narrow (Fig. 4.3, left) and wide (Fig. 4.3, right) shelf cases, where water moves along the bottom, through the Inner Shelf, then offshore near the surface. The upwelling zone is bounded onshore by the Inner Shelf, defined below, and offshore

by the location of the upwelling front.

The upwelling front is located where the cool, recently upwelled waters, meet the warmer surface waters that existed prior to upwelling. At the upwelling front, a noticeable deepening streamlines indicates a sizable reduction in offshore velocity. After 10 days of upwelling favorable wind stress, a substantial difference in the position of upwelling front exists between the narrow and wide shelf cases. Over the narrow shelf, the upwelling front is positioned between 10 and 17 km from shore and extends to a maximum depth of 45 m (Fig. 4.3a). In contrast, Figure 4.3b shows that the upwelling front over the wide shelf is between 20 and 25 km from shore and reaches 30 m deep. The offshore extent of the upwelling front is thus narrower and located farther from shore over wide shelves compared to narrow shelves.

The Inner Shelf is generally defined as the region where the surface mixed later (SML) and bottom boundary layer (BBL) intersect such that mixing extends from the surface to the bottom. This region can be seen in cross-sections of diffusivity (Fig. 4.3c, d). I note that in the model, streamlines of the flow (white contours) upwell from bottom to surface boundary layers in this region where vertical diffusivity is elevated and fairly constant with depth. This region thus also coincides with the location where flow transitions from onshore along the bottom to offshore near the surface. Figure 4.3c shows the offshore extent of the Inner Shelf is 4 km from shore for the narrow shelf case while it is 10 km from shore in the wide shelf case (Fig. 4.3d). The Inner Shelf covers a smaller lateral region and is closer to shore in the narrow shelf case compared to the wide shelf configuration.

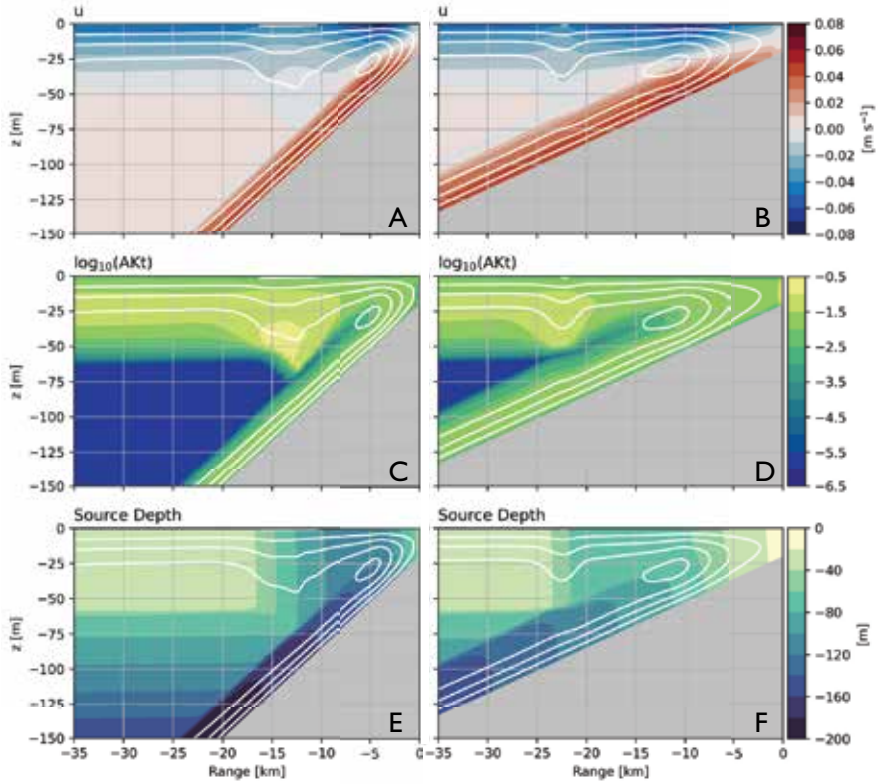

Figure 4.3: Cross-shelf velocity (a, b), log-10 transformed diffusivity (c, d) and source depth (e, f) for the narrow and wide shelf two-dimensional simulations, respectively. Results are shown after ten days of upwelling with streamlines shown as while lines in each subplot.

The source depth of water supplied to the upwelling zone determines its nutrient content. I quantify the depth of source water with a passive tracer initialized with values equivalent to the initial grid cell depth. In the narrow shelf case, water with a source depth of 90 m is found within 15 km from the coast (Fig. 4.3e). In contrast, Figure 4.3f shows that the upwelling source depth over a wide shelf is from 50 m deep and is present at the surface 22 km from the coast.

I separate the effect of upwelling on nutrient transport from biological processing by implementing a passive tracer that is initialized with the identical profile as the nutrient. Figure 4.4 shows the distribution of the tracer after ten days of upwelling in the (a) narrow and (b) wide shelf scenarios. Because the nutrient profile used here becomes nearly constant with depth below 70 m, water sourced from deeper depths contains a similar amount of nutrients and tracer. I define the tracer and nutrient inventory by integrating 70 m to the surface and inshore of 30 km. On model-day 10, the inventory of the tracer is 14.2% larger over the narrow shelf compared to the wide shelf scenario. Similarly, for the nutrient involved in biological processes, the inventory is 15.3% larger over the narrow shelf compared to the wide shelf (Fig. 4.4d). Narrower shelves are more efficient at delivering high levels of nutrients to the coast compared to wider shelves.

By subtracting the nutrient from the tracer, I recover the amount of utilized nutrients that have been upwelled and biologically processed out of the nutrient pool and into other ecosystem components, referred to here as *excess* nutrients. Figure 4.4e, f shows the distribution of excess nutrients in the narrow and wide shelf scenarios,

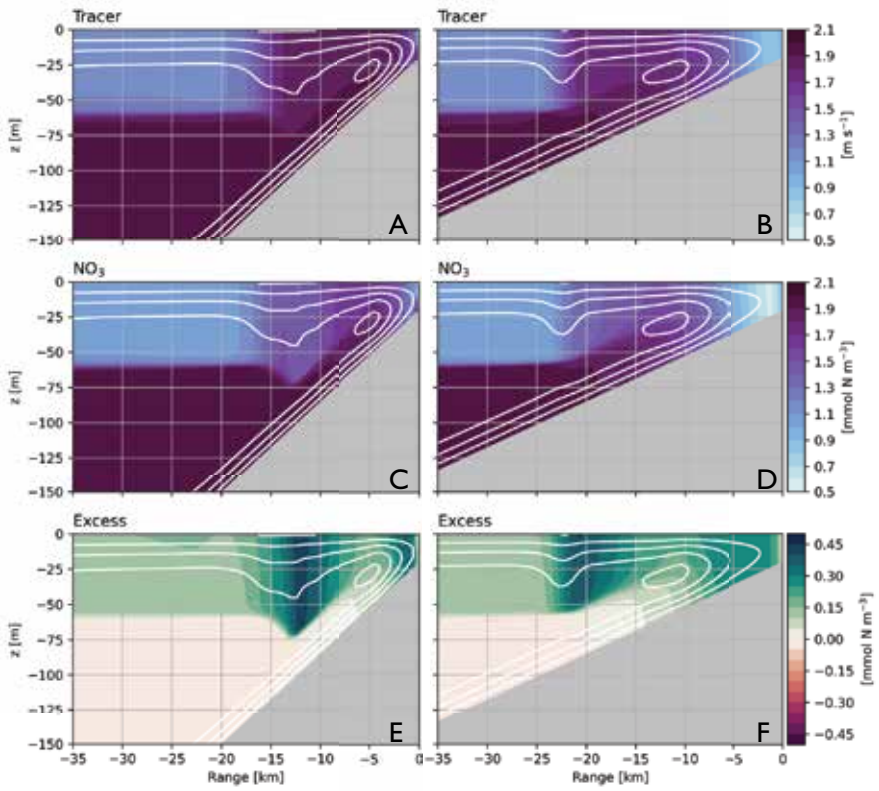

Figure 4.4: Concentrations of a passive tracer with an initial profile identical to the nutrient after 10 days of upwelling over two-dimensional narrow shelf (a) and wide shelf (b). Panels (c) and (d) show the same for nitrate. The difference between the tracer and nutrient shows the amount of excess nutrient not utilized by phytoplankton over the narrow (e) and wide (f) shelf scenarios.

respectively. The largest amount of excess nutrients in both cases occurs at or near the upwelling front and is positive throughout the upper 60 m of the water column. These are locations where phytoplankton biomass reaches cross-shelf maxima (not shown). The inventories of excess nutrients is merely 4.3% larger in the narrow shelf relative to the wide shelf, indicating that nutrient uptake is at or near saturation for this biological parameter set.

Figure 4.5 shows the change in primary production (ΔPP) over the (a) narrow

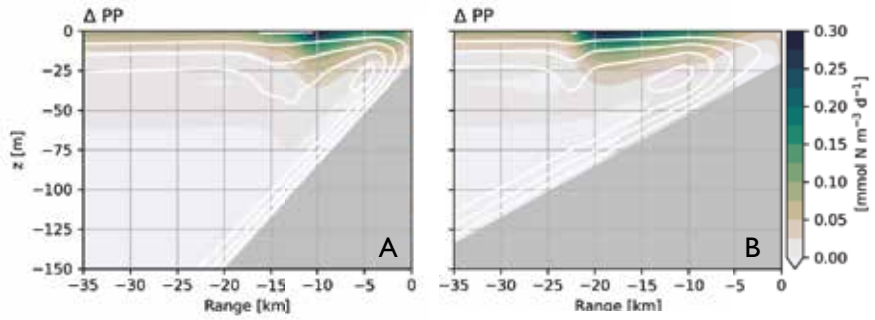

Figure 4.5: Change in primary production from the initial value to model-dat 10 over the narrow shelf (a) and over the wide shelf (b). Streamlines shown as white contours.

shelf and (b) wide shelf after 10 days of upwelling. The smaller upwelling zone over the narrow shelf results in a region of elevated ΔPP confined to the same location between 5 and 15 km from the coast. In contrast, the upwelling zone over the wide shelf is more extensive, resulting in a region of elevated Δ PP between 10 and 22 km from the coast, with an area 59% larger than the narrow shelf case. In both two-dimensional cases, the largest enhancement of primary production occurs in the region between the upwelling front and the Inner Shelf.

Integrating ΔPP with respect to depth and cross-shore position, reveals that there is a very small net increase (2.1%) in primary production over the wide shelf compared to the narrow shelf. In the narrow shelf case, more nutrients are supplied from a deeper depth, but the supply to the euphotic zone occurs over a smaller lateral extent. In the wide shelf case, lower nutrient concentrations are sourced to the euphotic zone but are supplied over a larger spatial extent compared to the narrow shelf case. The level of nutrients supplied to the euphotic zone in both cases with an initial nutrient profile (Fig. 4.2b) causes the Michaelis-Menten nutrient uptake term (eqn. 4.3b) to be

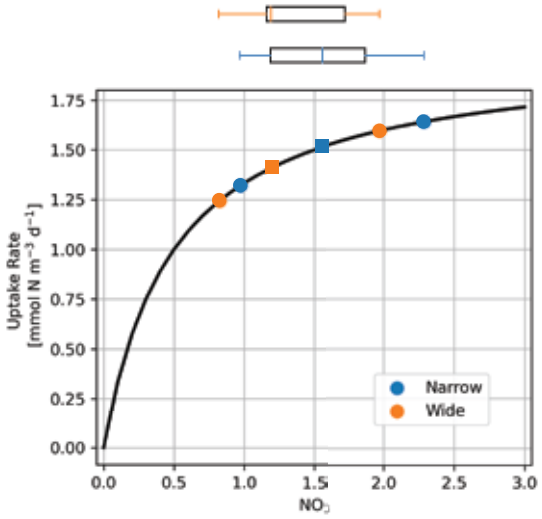

Figure 4.6: Box plots and Michaelis-Menten curve (black line) with the range (circles) and median (squares) of nutrient-like tracer concentrations from the narrow shelf (blue) and wide shelf (orange) taken from locations where there are excess nutrients (see text).

7.4% higher in the narrow shelf case, but is relevant over a smaller lateral zone (Fig. 4.6). As a result, the overall, net integrated change in primary production is similar in both scenarios.

4.2.2 Three-dimensional Upwelling with a Linear Model

In the vicinity of changes in shelf width, substantial deviations from the patterns described above occur. In particular, the transition between the different upwelling regimes cause the two patterns to combine to either enhance or suppress nutrient supply to the euphotic zone. As a result, primary production levels are elevated downwind of a widening shelf and inhibited downwind of a narrowing shelf.

4.2.2.1 Widening Shelf

Figure 4.7a shows the depth average current, **U**, averaged over the inner 26 km of the shelf. Up-wind of the shelf width transition, the along-isobath component of **U** increases in magnitude from -0.43 m s^{-1} to -0.48 m s^{-1} between $y = 2100$ km and $y = 2050$ km. As the shelf begins to widen, the magnitude of along-isobath velocity reaches a maximum of -0.51 m s^{-1}. Then, as the shelf transitions to its full width at $y = 2020$ km, the along-isobath component of **U** declines in magnitude to -0.30 m s^{-1}. In the cross-isobath direction, **U** is near zero indicating a balance between onshore and offshore transport. However, as the shelf begins to widen the balance becomes positive, favoring larger onshore transport as water move across isobaths.

The contours in Figure 4.7b show the cross-isobath bottom Ekman transport (eqn. 4.4) over the widening shelf. As predicted by Pringle, (2002), at the location where the shelf initially increases width near $y = 2050$ km, cross-isobath bottom Ekman transport increases to a local maximum greater than the narrow shelf upwind and the wide shelf downwind. The strength of elevated bottom Ekman transport declines as the shelf continues to widen between $y = 2050$ km and $y = 2020$ km, which then returns to a spatially uniform value when the shelf reaches its widest width.

Figure 4.7c shows that in response to the enhanced Ekman transport, the deepest source waters are located where the shelf widens. Waters originating from as deep as 180 m are present at the surface and located between the 50 m and 100 m isobaths over the shelf width transition. Moreover, waters originating from at least 100

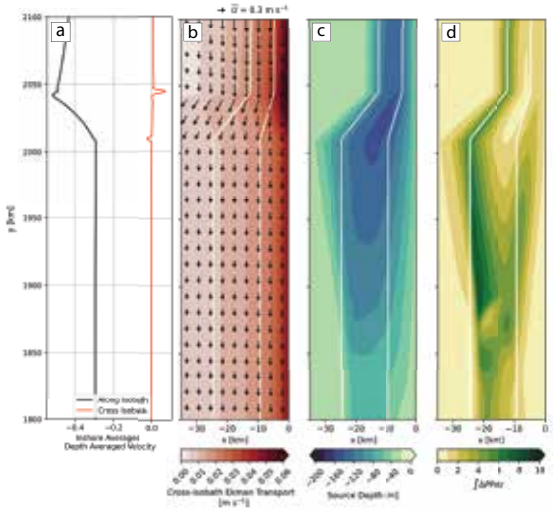

Figure 4.7: Wind driven upwelling over a widening shelf driving depth averaged velocity averaged inshore of x = -26 km in the along-isobath (black line) and cross-isobath (red) directions in panel (a). Panel (b) shows cross-isobath Ekman transport as color contours, with depth averaged velocity (vectors). For reference, the velocity key in the upper right of panel (b) show a vector with a value of 0.3 m s^{-1}. Source depth at the surface is shown in panel (c), and depth integrated primary production is show in panel (d). In panels (b) through (d) the position of the 100 m and 50 m isobaths are shown for reference.

m depth are present at the surface 150 km downwind of the shelf width transition. The presence of these deep waters far south of the shelf transition indicates an accompanying supply of nutrient-rich water over the wide region of the shelf.

Associated with the upwelling-driven nutrient supply, elevated depth-integrated ΔPP occurs over a broad region over the wide shelf (Fig. 4.7d). Similar to the two-dimensional simulations, upwind of the shelf transition an enhancement of primary production occurs between 10 and 15 km from shore. In the alongshore direction, the largest enhancement in primary production occurs between 50 km and 125 km downwind of the shelf transition, between $y = 1970$ km and $y = 1920$ km, where a large proportion of the shelf experiences elevated primary production.

The deep source water that eventually fuels downstream primary production is initially upwelled where the shelf widens. At this location, upwelling transports deep waters with low phytoplankton biomass to the surface, causing a local minimum in primary production directly over the upwelling center (Fig. 4.7d). Figure 4.8a shows cross-isobath bottom velocity is at a maximum of 0.14 m s^{-1} where the initially shelf widens. Near this same location, along-shelf velocity reaches a local maximum in magnitude of -0.6 m s^{-1} and decelerates to -0.3 m s^{-1} once the shelf reaches its full width (Fig. 4.8b). As bottom water flows into the shelf width transition, it slows down and is forced across isobaths, creating a upwelling center where BBL waters move into shallower waters.

To illustrate how this alongshelf distance is related to the alongshore current, Figure 4.9 shows a time series of source depth at the surface from model day 5 through

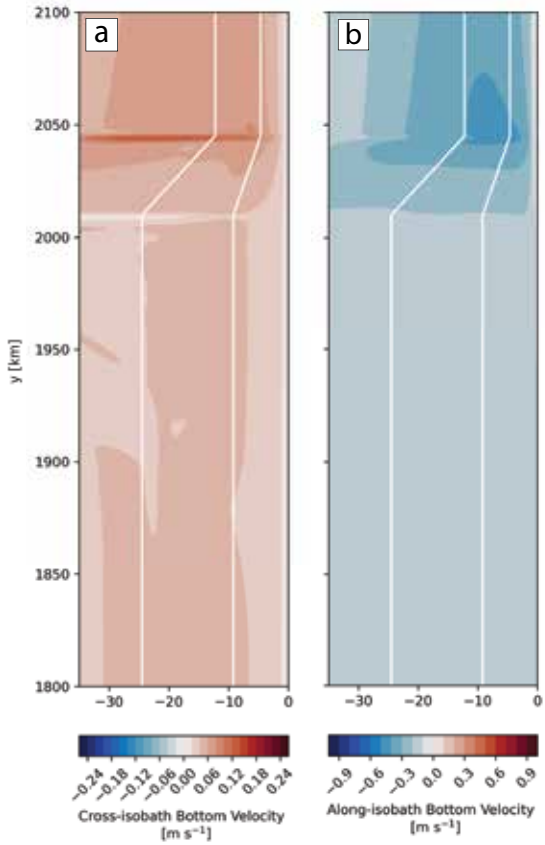

Figure 4.8: Cross-isobath (a) and along-isobath (b) bottom velocity shown over the widening shelf.

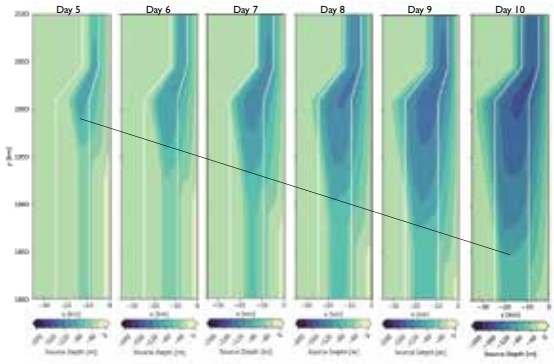

Figure 4.9: Time series of the source depth of upwelled water over the widening shelf from model day 5 to 10. The reference line corresponds to the rate of the alongshore surface current, 0.32 m s^{-1}.

day 10. The reference line corresponds to a rate of 0.32 m s^{-1}, which is the rate of the alongshore surface current over the wide shelf (not shown). Water initially brought to the surface at the shelf width transition will travel at this rate 165 km south over the final 6 days of model integration. The spatial scale of the downstream affect of the shelf transition is set by the alongshore fluid velocity.

4.2.2.2 Narrowing Shelf

The efficiency of nutrient upwelling into the euphotic zone is reduced when the shelf width transitions from a wide to a narrow shelf. Figure 4.10a shows that the depth average current, **U** increases in magnitude as the shelf narrows between $y = 850$ km and 820 km. Over this region, the along-isobath component of **U** averaged over the inner 26 km of the shelf increases from -0.19 m s^{-1} to -0.24 m s^{-1}. At the same time, the cross-isobath component deviates from zero to -0.001 m s^{-1} as the shelf narrows, briefly becoming a small positive of 0.025 m s^{-1} at $y = 825$. The adjustment in cross-isobath depth-average velocity occurs rapidly over the shelf transition.

In response to the reduced Ekman transport over the narrowing shelf (Fig. 4.10b), upwelled water in this region is sourced from shallower depths. At the surface, the passive tracer that indicates source depth shows that upwelled water originates near 60 m depth (Fig. 4.10c). The region of shallow source water extends both upwind and downwind of the narrowing shelf by 50 km. The lateral extent of reduced upwelling suggests that locations where the shelf width narrows should be regions of lower nutrient delivery.

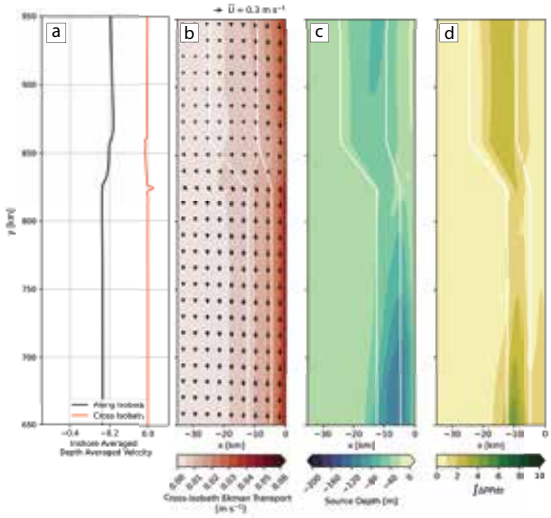

Figure 4.10: Wind driven upwelling over a narrowing shelf driving depth averaged velocity averaged inshore of x = -26 km in the along-isobath (black line) and cross-isobath (red) directions in panel (a). Panel (b) shows cross-isobath Ekman transport as color contours, with depth averaged velocity (vectors). For reference, the velocity key in the upper right of panel (b) show a vector with a value of 0.3 m s^{-1}. Source depth at the surface is shown in panel (c), and depth integrated primary production is show in panel (d). In panels (b) through (d) the position of the 100 m and 50 m isobaths are shown for reference.

As a result of reduced nutrient supply, primary production is lower near the narrowing shelf. Figure 4.10d shows the depth-integrated change in primary production from the initial condition. The location of the lowest level of primary production is between 20 km and 60 km downwind of the shelf width transition. Here, the reduced upwelling at the transition lowers the amount of nutrients in the bottom boundary layer, and these low-nutrient waters are then transported south by the alongshore current before it is upwelled into the euphotic zone. Because these waters are primed with lower nutrient levels upstream, and the alongshore velocities are relatively small, nutrient levels in this region are low and magnitude of primary production is reduced.

4.2.3 Origins of Upwelled Waters

I estimate the source location of upwelled waters using the passive tracers initialized with values that correspond to their original position. Figure 4.11 shows the difference between the initial value and final value of the location-based tracer after ten days of upwelling favorable wind stress, which allows us to estimate the distance water travels in the cross-shore direction, ΔX, and in the along-shore direction, ΔY. Where the shelf widens in the direction of upwelling favorable wind, waters over the 100 m isobath, ΔX is near zero, indicating that water here did not travel far from the original cross-shore position (Fig. 4.11a). Inshore of the 100 m isobath, ΔX is negative, indicating water moved with the offshore propagation of the upwelling front. Offshore of the 100 m isobath waters moved onshore, sourced from 20 to 30 km offshore of their current location. In the along-shore direction, waters are sourced from more than 200

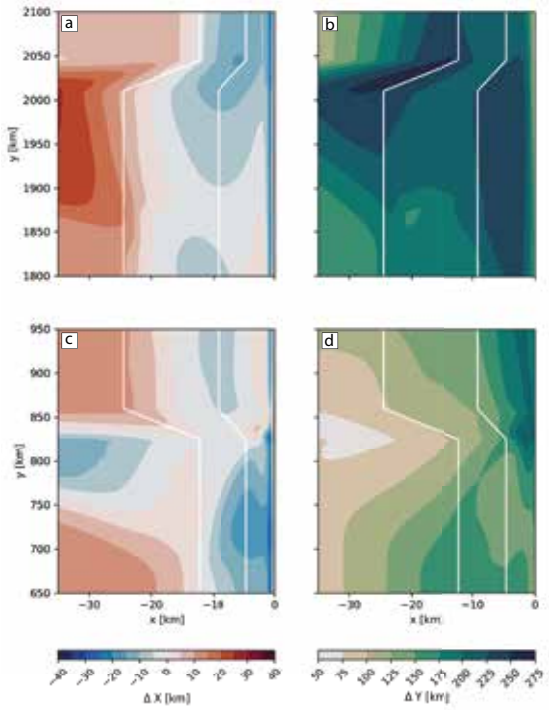

Figure 4.11: Source water location at the surface expressed as change from initial cross-shore position (a, c), and change in along-shore position (c, d) over the widening shelf (top row) and over the narrowing shelf (bottom row).

km north of where the shelf widens (Fig. 4.11b). In contrast, where the shelf narrows, waters are sourced from much closer regions. Figure 4.11c shows that at this location, ΔX is less than $\pm$10 km, which indicates cross-shelf motion is small. At the same time, ΔY is also small, indicating a low level of along-shelf transport (Fig. 4.11d). These results suggest that over a widening shelf, surface waters originate far from their initial location stimulating primary production far from the change in shelf width and regions where the shelf narrows may be locations where waters are sourced more locally from shallower depths leading to lower levels of primary production.

4.2.4 Sensitivity to Stratification

I test the effect of stronger stratification conditions on wind-driven nutrient supply over varying shelf geometry. In the three-dimensional model, I impose stronger stratification with a buoyancy frequency, N, equivalent to 0.01 s^{-1}, which corresponds to values typically found within the pycnocline [38] and results in a Burger Number (eqn. 4.2) of 0.11 and 0.43 for the wide and narrow shelf cases, respectively. In this simulation, cross-isobath Ekman transport shows a similar pattern to the case discussed above, although the maximum value nearshore is weaker, reaching a maximum of 0.05 m s^{-1} (Fig. 4.12a). Similarly, Figure 4.12b shows that the spatial pattern of source waters to the surface reflects the case discussed above, but the deepest source waters over the widening shelf originate from a depth 20 m deeper. In response, the largest depth-integrated ΔPP is 30% greater in this simulation compared to the base configuration discussed above and is highlighted by the gray contour (Fig. 4.12c). Overall, the qualitative agreement between simulations in this linear configuration show that regardless of the strength of stratification, primary production is enhanced 150 km downwind of a widening shelf reaching $y = 1850$.

4.2.5 Sensitivity to Biological Parameters

Lastly, I test the effect of an oligotrophic parameter set to the three-dimensional upwelling process. In this experiment, I follow Eppley et al., (1969) and reduce the maximum uptake rate, V_m, to 0.6 mmol N m^{-3} d^{-1} and reduce the half-saturation value to 0.1 mmol N m^{-3} d^{-1}. To further reflect oligotrophic systems the light attenuation

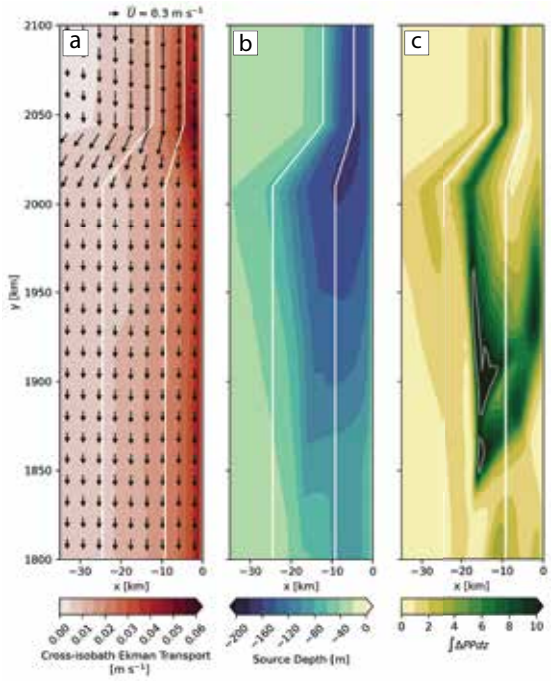

Figure 4.12: Wind driven upwelling over a widening shelf with stronger stratification ($N = 0.01$ s^{-1}). Panel (a) shows cross-isobath Ekman transport (color contours) with depth averaged velocity (vectors). Source depth at the surface is shown in panel (b), and depth integrated primary production with the values greater than 10 mmol m^{-2} d^{-1} highlighted with the gray contour show in panel (c). In each panel from left to right, the position of the 100 m and 50 m isobaths are shown for reference.

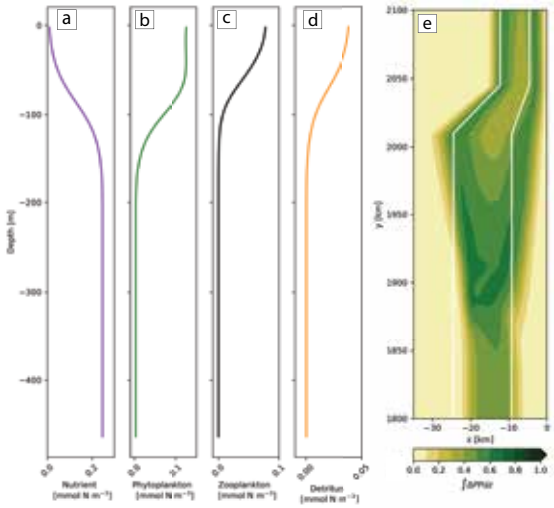

Figure 4.13: Initial conditions for the oligotrophic ecosystem parameter set for the nutrient (a), phytoplankton (b), zooplankton (c), and detritus (d). Vertically integrated primary production on model-day 10 is shown in panel (e).

coefficient, K_{ext}, phytoplankton mortality, m, zooplankton grazing rate, zooplankton mortality, M_d, and the zooplankton excretion rate, β, and detrital remineralization rate, r, are reduced to 0.035 m^{-1}, 0.01 d^{-1}, 0.6 d^{-1}, 0.01 d^{-1}, and 0.015, and 0.025 d^{-1}, respectively. This ecosystem is integrated to steady state in one dimension (depth) before coupling to the larger three-dimensional model. The initial conditions for this version of the NPZD model are shown in Figure 4.13a-d.

Figure 4.13e shows the depth-integrated change in primary production of an oligogtrophic ecosystem over a widening shelf after ten days of upwelling. The change in primary production is an order of magnitude smaller than the copiotrophic ecosystem described above. The spatial pattern of primary production enhancement is shifted inshore, and is bimodal, large over both the 100 m and the 50 m isobaths. The inshore peak likely occurs because the nutrient uptake term is large there. Similar to

the copiotrophic experiments, the peaks in primary production are separated by a local minimum over the upwelling center due to the delivery of deep water with low phytoplankton biomass. In addition, the downstream enhancement of primary production occurs nearly 165 km from the widening shelf. This sensitivity study highlights how alongshore advection physically separates the primary production response from the upwelling center, and that this downstream extent is largely unaffected by the ecosystem parameter set.

4.3 Discussion

4.3.1 Connectivity of the Bottom Boundary Layer and Euphotic Zone in Two-dimensional Simulations

Wind-driven coastal upwelling supports enhanced primary production by supplying deep, nutrient-rich waters to the euphotic zone. In two-dimensions, the depth from which these waters originate, and consequently their nutrient content, is determined by shelf geometry defined by the Burger Number, S (eqn. 4.2) [9, 50]. Steep shelves with larger S, have thinner bottom boundary layers (BBL) that source waters from a deeper depth with higher nutrient concentration, compared to wider shelves with smaller S and thicker BBL that source water from a shallower depth. Over a narrow shelf the upwelled water that is transported into the euphotic zone covers a smaller cross-shelf area compared to the wide shelf (Fig. 4.4). Although the BBL waters are lower in nutrients in the wide shelf, it is shallower, making the offshore extent of the

Inner Shelf farther from shore, creating a broad region where nutrient-rich waters are readily transported into the euphotic zone. In our experiments here, the quantity of nutrient delivery in both two-dimensional cases is large enough to saturate the nutrient uptake term (eqn. 4.3b), causing the total integrated primary production to be nearly equivalent in these two scenarios (Fig. 4.5).

4.3.2 Alongshore Transport and Primary Production in Three-dimensional Simulations

In three-dimensions, the mechanism described by Pringle, 2002 creates onshore flow upwind of the widening shelf, which enhances up-shelf transport within the BBL in the widening shelf transition region [93]. In the work presented here, I show that in both the widening and narrowing shelf regions, transport of waters within the BBL affect downstream primary production. Where the shelf widens downwind, increased friction on the landward side enhances cross-isobath flow, elevating the nutrient content of BBL parcels. Upwelling over the wide shelf then carries enriched BBL waters into the euphotic zone, enhancing primary production downstream of the shelf transition. Similarly, where the shelf narrows in the direction of upwelling favorable wind, friction on the landward side is reduced, which causes a decrease in cross-isobath bottom Ekman transport, reducing the nutrient content within the BBL. Downstream, upwelling over the narrow shelf carries lower nutrient bottom boundary waters into the euphotic zone, resulting in reduced levels of primary production.

In nature, there is substantial variation in width of continental shelves varies

in the alongshore direction. For example, from north to south along the northern and central California coast, the continental shelf narrows south of Cape Mendocino, widens near the Gulf of the Farallones, and narrows again into Monterey Bay. Based on the analysis presented here, upwelling nutrient transport into the euphotic should be enhanced downwind of the Gulf of the Farallones. Which, when combined with elevated upwelling favorable wind stress in the region, may help explain the high level of productivity in the region [34].

The spatial decoupling of upwelling centers from the surface expression has been documented in several regions. For example, realistic modeling studies of the South China Sea report that flow-topography interactions accelerate fluid up-slope where the shelf widens in the direction of the wind [15]. When alongshelf transport is strong during winter, the horizontal advection becomes a sink for nutrients on the shelf and slope [71]. In the California Current, the alongshore spatial pattern of low-pH and low-oxygen conditions is directly related to the local upwelling intensity, with the alongshore regions of coastal low-pH and low-oxygen exposure extend downstream of the upwelling centers [16]. In both of these regions, the spatial decoupling is often associated with a coastal promontory [31, 65]. Whereas in this work, I show that a submarine bank produces a similar decoupling of the upwelling center and the surface expression of deep waters near the surface.

It is worth noting that the physical model used in this study neglected the nonlinear advection of momentum. If nonlinear terms were included in this analysis, additional transport mechanisms may affect two- and three-dimensional results. In

simulations of two-dimensional upwelling, Lentz and Chapman, 2004 showed that the partition of source waters between the geostrophic interior and the bottom boundary layer partially depends on the nonlinear momentum flux divergence [62]. Similarly, in three-dimensional simulations of upwelling over an idealized submarine bank, Castelao and Barth, 2006 showed that by including nonlinear momentum advection, vorticity dynamics lead to the formation of an offshore jet, which enhances cross-isobath transport when the jet detaches from bathymetry [11]. Including nonlinear advection may increase the connectivity of the bottom boundary layer to the euphotic zone, enhancing the primary production response downstream of widening shelf-width transitions and will be interesting for future study.

4.3.3 Summary and Conclusion

The two-dimensional perspective on wind-driven coastal upwelling highlights the importance of cross-shelf exchange on nutrient transport and primary production. In particular, two-dimensional models highlight that the connectivity of the bottom boundary layer with the euphotic zone drives the integrated primary production response. In three-dimensions, however, alongshore transport influences the nutrient content of bottom boundary layer parcels before they make contact with the euphotic zone. In locations where the shelf widens in the direction of upwelling favorable wind stress, deep source waters are upwelled within the bottom boundary layer. Upslope Ekman transport is further enhanced by the CTW generation mechanism described by Pringle, 2002 [93]. Alongshore transport then moves the waters within the bottom boundary

layer, primed with elevated nutrient content, over a wider shelf. Relative to the wide shelf two-dimensional simulation, primary production is elevated downstream of the shelf transition. Similarly, where the shelf narrows in the direction of upwelling favorable wind stress, bottom boundary layer transport is less efficient, reducing the nutrient content of waters that are eventually upwelled downstream. The results presented here highlight the importance of upstream boundary layer processes on the efficiency of nutrient transport in wind-driven coastal upwelling systems.

Chapter 5

Conclusion

This dissertation investigates how baroclinic processes affect marine primary production by exploring three case studies. Chapter 2 focused on the generation of internal tides and found that the adjustment of the nutricline by an advective flux divergence was primarily responsible for the enhancement of primary production. In a different physical scenario, Chapter 3 found a similar result: elevated advective and diffusive flux divergences of the nutrient field determined the magnitude of the primary production response to an island trapped wave. However, experiments in Chapter 3 also showed that including the diel light cycle, resulted in a substantial adjustment of the spatial pattern of the primary production response. Chapter 4 shifted away from baroclinic waves and concentrated on a different type of baroclinic process, wind-driven coastal upwelling. Here, the baroclinicity arises due to stratification at the surface, which causes the fluid, forced at the surface, to respond in three distinct layers. Although the system in Chapter 4 is unmistakably different from the systems in the preceding

chapters, the nature of the advective and diffusive fluxes that result from the baroclinic process injects nutrients into the euphotic zone stimulating primary production.

5.1 Tidal Beams and Primary Production: Summary and Future Directions

Chapter 2 used idealized numerical simulations to quantify the primary production response to the generation of internal tides by tidal flow over a step change in bathymetry. Before this work, it was unclear whether baroclinic motion affected primary production by changing how an algal cell experiences light or adjusting the nutrient environment. Chapter 2 separated the light and nutrient contributions to primary production by representing algal particles as Lagrangian parcels. Displacement of algal particles through the exponentially varying light field, while positive definite, only made a minor enhancement of primary production. The primary mechanism through which the generation of internal tides affects primary production is through the advective flux divergence of the nutrient field, that causes nutrient isopleths to shoal, pumping nutrients into the euphotic zone. This elevated nutrient advective flux divergence is associated with the tidal beam. Because this process occurs over a wide range of bathymetric heights and slopes tested, the generation of internal tides should affect the baseline level of primary production in the overlaying euphotic zone wherever they occur in the global ocean.

In nature, tidal beam generation occurs wherever tidal flow is perpendicular

to changes in bathymetric height, making it relatively common throughout the global ocean. Where tidal beams exist, the lateral extent of the bathymetric feature causes the generation of a tidal sheet instead of a tidal beam, as described in this dissertation. The location where the tidal sheet passes through the nutricline varies because temporal changes in stratification adjust the slope of baroclinic energy propagation, as prescribed by the dispersion relation. In addition, there are multiple tidal constituents, such as the S_2 tide with a period of 12 hours, and the N_2 with a period 12.65 hours, that also influence the slope of baroclinic energy propagation as a tidal sheet. The combination of these processes is likely to result in a shallower nutricline across a broad region over an internal tide-generating bathymetric feature, which could increase the spatial extent of primary production enhancement.

Future work examining the role of internal tide generation on primary production should include investigations using additional idealized simulations, realistic numerical models, and observational approaches. The hydrostatic construction of the numerical model used here imposed a limitation on the estimates of diffusive flux divergence caused by the tidal beam. Nonhydrostatic effects may elevate diffusive flux divergences. Future work should use a non-hydrostatic model to more accurately compare the magnitudes of advective and diffusive flux divergences caused by internal tide beams passing through the nutricline. Future work should also include idealized or realistic numerical simulations to quantify how time-variable stratification adjusts the advective flux of nutrients and the primary production response. In addition, defining the minimum grid resolution needed to include internal tide beam generation could in-

form global simulation experiments that estimate the integrated effect of internal tides on primary production. By including a parametrization of internal tide generation in global simulations, estimates of carbon sequestration in the deep chlorophyll maximum will likely increase. Lastly, observations in known regions of internal tide generation by autonomous platforms equipped with an optical package (nitrate and chlorophyll) could provide real-world context for the role tidal beams play in stimulating primary production at locations where they occur.

5.2 Island Trapped Waves and Primary Production: Summary and Future Directions

Chapter 3 established the mechanism through which island trapped waves affect primary production. As part of the resonant response, a combination of enhanced advective and diffusive flux divergences elevated the transport of nutrients into shallower, more well-lit depths, enhancing the local primary production level. The amount of nutrients supplied by the island trapped wave determined the magnitude of the primary production response. However, a comparison of simulations with constant and diel surface irradiance with the primary production decomposition metric described in this chapter shows that the most considerable changes in primary production occur when the unrelated nutrient and light variables become correlated. The application of a Reynolds flux to the primary production model attributes the mechanism that controls the spatial distribution of the primary production due to the phasing of the island

trapped wave with the light cycle.

Chapter 3 was a pseudo-companion paper to an observational paper describing the relationship between island trapped waves and primary production around the island of Lastovo in the Adriatic Sea [66]. Future work should include a more rigorous comparison between observational and numerical modeling efforts. A realistic model of the Adriatic Sea coupled with a simple ecosystem model could examine the frequency and intensity of island trapped waves and compare the levels of primary production during times with and without an island trapped wave in an internally consistent way. Other areas of future research could explore the larger context of the influence of island trapped waves on primary production. As an island trapped wave propagates, the associated advective and diffusive fluxes will eventually erode the thermocline, pushing the system off resonance. A realistic model could examine the seasonality of the influence of island trapped waves on local primary production levels. An idealized model or a realistic process-based numerical study could examine this interaction to estimate the time scale an island trapped wave can exist, which would allow further constraint on the role island trapped waves play in affecting the ecosystem. Lastly, as mentioned in the discussion of Chapter 3, the idealized experiments presented here could provide a test bed for ecosystem model development, particularly regarding the nonlinear response to saturating light in primary production models. Each of these potential future directions would further our understanding of island trapped waves' role in adjusting the local primary production levels.

Island trapped waves in nature are ephemeral, existing only when stratification

and forcing periods lead to a resonant interaction. In the case of the Island of Lastovo in the Adriatic Sea, strong seasonal stratification prevents nutrient delivery to the euphotic zone, leading to low primary production levels throughout most of the basin. When island trapped waves are excited, the associated nutrient injection fuels a large, but local phytoplankton bloom. The temporary increase in phytoplankton biomass likely propagates up the food web and supports growth at higher trophic levels.

5.3 Coastal Upwelling and Primary Production: Summary and Future Directions

Chapter 4 explored how shelf geometry adjusts the nutrient supply by wind-driven coastal upwelling and primary production. In two-dimensions, shelf slope determined upwelling source depth, where steeper, narrower shelves supply deeper, more nutrient-rich waters to the euphotic zone relative to wider shelves. The change in primary production was similar between these cases because the quantity of nutrients was elevated above the half-saturation value ($k_s = 0.5$ mmol N m^{-3}) causing the uptake to saturation with respect to nutrients. This result highlights a clear limitation of the ecosystem model. In nature, feedback with the light field or lateral nutrient dissipation may prevent uptake to become saturated with respect to nutrients. The two-dimensional upwelling simulations provide an opportunity to test future primary production models that include shelf-shading so that we can improve estimates of primary production in realistic modeling applications.

In three-dimensions, alongshore changes in shelf width adjust upwelling source depth. At locations where a shelf widens in the direction of upwelling-favorable wind there is an additional transport of Bottom Boundary Layer (BBL) water up-slope [93]. However, the primary production response is spatially decoupled from the enhancement. Downwind, upwelling over the wide shelf transports nutrient-rich BBL water into the euphotic zone stimulating primary production over a broad region. The downwind length-scale of the enhancement is set by the magnitude of the depth-averaged current. Future work should include nonlinear advection to investigate their role in nutrient transport as well as sensitivity studies to a range of wind stress magnitudes, ratios of narrow and wide shelf slopes, and the length scale between each transition.

There are several mechanisms that contribute to the patchy distribution of phytoplankton blooms observed along eastern boundary upwelling systems. In nature, continental shelves are rarely uniform in the alongshore direction and it is common to find both widening and narrowing shelves. The decoupling of bottom boundary layer transport from delivery to euphotic zone likely contributes to the spatial variability of phytoplankton blooms that occur during and after strong upwelling events.

5.4 Primary Production Response to Baroclinic Motion

This dissertation explored three case studies of how baroclinic motion affects light and nutrient availability for primary production. Each case study highlighted how the context in which a baroclinic process is excited determines the mechanism through

which the nutrient and light environment are adjusted for phytoplankton. However, a general description of the relationship between baroclinicity and primary production was not investigated. A theoretical investigation from first principles and known analytic representations of light and nutrient profiles could unify the results presented in these chapters. Until a theoretic solution is found, the relationship between baroclinic motion and primary production remains to be assessed on a case-by-case basis.

Bibliography

[1] Matthew H Alford. Redistribution of energy available for ocean mixing by long-range propagation of internal waves. *Nature*, 423(6936):159–162, 2003.

[2] Alana M. Althaus, Eric Kunze, and Thomas B. Sanford. Internal tide radiation from mendocino escarpment. *Journal of Physical Oceanography*, 33(7):1510–1527, 2003.

[3] Jay A Austin and Steven J Lentz. The inner shelf response to wind-driven upwelling and downwelling. *Journal of Physical Oceanography*, 32(7):2171–2193, 2002.

[4] Andrew Bakun. Coastal upwelling indices, west coast of north america, 1946-71. *US Department of Commerce, National Oceanic and Atmospheric Administration, National Marine Fisheries Service*, 1973.

[5] NJ Balmforth, GR Ierley, and WR Young. Tidal conversion by subcritical topography. *Journal of Physical Oceanography*, 32(10):2900–2914, 2002.

[6] JA Barth. Stability of a coastal upwelling front: 1. model development and a

stability theorem. *Journal of Geophysical Research: Oceans*, 94(C8):10844–10856, 1989.

[7] KH Brink. Island-trapped waves, with application to observations off bermuda. *Dynamics of atmospheres and oceans*, 29(2-4):93–118, 1999.

[8] KH Brink. Cross-shelf exchange. *Annual review of marine science*, 8(1):59–78, 2016.

[9] KH Brink. *Physical Oceanography of Continental Shelves*. Princeton University Press, 2023.

[10] G. S. Carter, M. A. Merrifield, J. M. Becker, K. Katsumata, M. C. Gregg, D. S. Luther, M. D. Levine, T. J. Boyd, and Y. L. Firing. Energetics of m2 barotropic-to-baroclinic tidal conversion at the hawaiian islands. *Journal of Physical Oceanography*, 38(10):2205–2223, 2008.

[11] Renato M Castelao and John A Barth. The relative importance of wind strength and along-shelf bathymetric variations on the separation of a coastal upwelling jet. *Journal of physical oceanography*, 36(3):412–425, 2006.

[12] BT Kuebel Cervantes, JS Allen, and RM Samelson. A modeling study of eulerian and lagrangian aspects of shelf circulation off duck, north carolina. *Journal of physical oceanography*, 33(10):2070–2092, 2003.

[13] David M Checkley and John A Barth. Patterns and processes in the california current system. *Progress in Oceanography*, 83(1-4):49–64, 2009.

[14] Zhiwu Chen, Jieshuo Xie, Jiexin Xu, Yinghui He, and Shuqun Cai. Selection of internal wave beam directions by a geometric constraint provided by topography. *Physics of Fluids*, 29(6):066602, 2017.

[15] Weicong Cheng and Jianping Gan. Variability of the bottom boundary layer induced by the dynamics of the cross-isobath transport over a variable shelf. *Journal of Geophysical Research: Oceans*, 129(7):e2024JC020895, 2024.

[16] Julia Cheresh and Jerome Fiechter. Physical and biogeochemical drivers of alongshore ph and oxygen variability in the california current system. *Geophysical Research Letters*, 47(19):e2020GL089553, 2020.

[17] Sophie Clayton, Stephanie Dutkiewicz, Oliver Jahn, and Michael J Follows. Dispersal, eddies, and the diversity of marine phytoplankton. *Limnology and Oceanography: Fluids and Environments*, 3(1):182–197, 2013.

[18] S. T. Cole, D. L. Rudnick, B. A. Hodges, and J. P. Martin. Observations of tidal internal wave beams at kauai channel, hawaii. *Journal of Physical Oceanography*, 39(2):421–436, 2009.

[19] John A Colosi. *Sound propagation through the stochastic ocean*. Cambridge University Press, 2016.

[20] Marin Cornec, Hervé Claustre, Alexandre Mignot, Lionel Guidi, Leo Lacour, A Poteau, F d'Ortenzio, Bernard Gentili, and Catherine Schmechtig. Deep chloro-

phyll maxima in the global ocean: Occurrences, drivers and characteristics. *Global Biogeochemical Cycles*, 35(4):e2020GB006759, 2021.

[21] GT Csanady. Baroclinic boundary currents and long edge-waves in basins with sloping shores. *Journal of Physical Oceanography*, 1(2):92–104, 1971.

[22] John J Cullen. The deep chlorophyll maximum: comparing vertical profiles of chlorophyll a. *Canadian Journal of Fisheries and Aquatic Sciences*, 39(5):791–803, 1982.

[23] Benoit Cushman-Roisin and Jean-Marie Beckers. *Introduction to geophysical fluid dynamics: Physical and numerical aspects*. Academic press, 2011.

[24] Emanuele Di Lorenzo, William R. Young, and Stefan Llewellyn Smith. Numerical and analytical estimatese of m2 tidal conversion at steep oceanic ridges. *Journal of Physical Oceanography*, 36(6):1072–1084, 2006.

[25] Michael Dunphy and Kevin G Lamb. Focusing and vertical mode scattering of the first mode internal tide by mesoscale eddy interaction. *Journal of Geophysical Research: Oceans*, 119(1):523–536, 2014.

[26] Phil Dyke. Wave trapping and flow around an irregular near circular island in a stratified sea. *Ocean Dynamics*, 55(3-4):238–247, 2005.

[27] Vagn Walfrid Ekman. On the influence of the earth's rotation on ocean-currents. *Archive for mathematics, astronomy and physics*, (11), 1905.

[28] Richard W. Eppley, Jane N. Rogers, and James J. McCarthy. Half-saturation constants for uptake of nitrate and ammonium by marine phytoplankton. *Limnology and Oceanography*, 14(6):912–920, 1969.

[29] Philippe Estrade, Patrick Marchesiello, Alain Colin De Verdière, and Claude Roy. Cross-shelf structure of coastal upwelling: A two—dimensional extension of ekman's theory and a mechanism for inner shelf upwelling shut down. *Journal of Marine Research*, (66):589–616, 2008.

[30] Mary Anne Evans, Sally MacIntyre, and George W. Kling. Internal wave effects on photosynthesis: Experiments, theory, and modeling. *Limnology and Oceanography*, 53(1):339–353, 2008.

[31] Jerome Fiechter, Christopher A Edwards, and Andrew M Moore. Wind, circulation, and topographic effects on alongshore phytoplankton variability in the california current. *Geophysical Research Letters*, 45(7):3238–3245, 2018.

[32] P. J. S. Franks, J. S. Wroblewski, and G. R. Flierl. Behavior of a simple plankton model with food-level acclimation by herbivores. *Marine Biology*, 91(1):121–129, 1986.

[33] Mara A Freilich and Amala Mahadevan. Decomposition of vertical velocity for nutrient transport in the upper ocean. *Journal of Physical Oceanography*, 49(6):1561–1575, 2019.

[34] M García-Reyes and JL Largier. Seasonality of coastal upwelling off central and

northern california: New insights, including temporal and spatial variability. *Journal of Geophysical Research: Oceans*, 117(C3), 2012.

[35] Chris Garrett and Eric Kunze. Internal tide generation in the deep ocean. *Annual Review of Fluid Mechanics*, 39(1):57–87, 2007.

[36] Christopher Garrett and Walter Munk. Internal waves in the ocean. *Annual review of fluid mechanics*, 11(1):339–369, 1979.

[37] Jessica C. Garwood, Ruth C. Musgrave, and Andrew J. Lucas. Life in internal waves. *Oceanography*, 33(3):38–49, 2020.

[38] Adrian E Gill. *Atmosphere—ocean dynamics*. Elsevier, 2016.

[39] T. Granata, J. Wiggert, and T. Dickey. Trapped, near-inertial waves and enhanced chlorophyll distributions. *Journal of Geophysical Research*, 100(C10):20793, 1995.

[40] Semyon A Grodsky, James A Carton, and Charles R McClain. Variability of upwelling and chlorophyll in the equatorial atlantic. *Geophysical Research Letters*, 35(3), 2008.

[41] Dale V Hebel and David M Karl. Seasonal, interannual and decadal variations in particulate matter concentrations and composition in the subtropical north pacic ocean. *Deep Sea Research Part II: Topical Studies in Oceanography*, 48:1669–1695, 2001.

[42] Nelson G Hogg. Observations of internal kelvin waves trapped round bermuda. *Journal of Physical Oceanography*, 10(9):1353–1376, 1980.

[43] P M Holligan, R D Pingreet, and G T Mardellt. Oceanic solitons, nutrient pulses and phytoplankton growth. *Nature*, 314:348–350, 1985.

[44] Greg Holloway. Effects of velocity fluctuations on vertical distributions of phytoplankton. *Journal of Marine Research*, 42, 1984.

[45] Greg Holloway and Kenneth Denman. Influence of internal waves on primary production. *Journal of Plankton Research*, 11(2):409–413, 1989.

[46] Peter E. Holloway and Mark A. Merrifield. Internal tide generation by seamounts, ridges, and islands. *Journal of Geophysical Research: Oceans*, 104(C11):25937–25951, 1999.

[47] John M Huthnance. On coastal trapped waves: Analysis and numerical calculation by inverse iteration. *Journal of Physical Oceanography*, 8(1):74–92, 1978.

[48] Yosuke Igeta, Keiichi Yamazaki, and Tatsuro Watanabe. Amplification of coastal-trapped waves resonantly generated by wind around sado island, japan. *Journal of Oceanography*, 71:41–51, 2015.

[49] Jasen R Jacobsen, Christopher A Edwards, Brian S Powell, John A Colosi, and Jerome Fiechter. Nutricline adjustment by internal tidal beam generation enhances primary production in idealized numerical models. *Frontiers in Marine Science*, 2023.

[50] MG Jacox and CA Edwards. Effects of stratification and shelf slope on nutrient

supply in coastal upwelling regions. *Journal of Geophysical Research: Oceans*, 116(C3), 2011.

[51] Alexandra E Jones-Kellett and Michael J Follows. A lagrangian coherent eddy atlas for biogeochemical applications in the north pacific subtropical gyre. *Earth System Science Data*, 16(3):1475–1501, 2024.

[52] Antoni Jordi, Gotzon Basterretxea, and Dong-Ping Wang. Evidence of sediment resuspension by island trapped waves. *Geophysical Research Letters*, 36(18), 2009.

[53] David M Karl, Karin M Björkman, John E Dore, Lance Fujieki, Dale V Hebel, Terrence Houlihan, Ricardo M Letelier, and Luis M Tupas. Ecological nitrogen-to-phosphorus stoichiometry at station aloha. *Deep Sea Research Part II: Topical Studies in Oceanography*, 48(8-9):1529–1566, 2001.

[54] Samuel M Kelly and Pierre FJ Lermusiaux. Internal-tide interactions with the gulf stream and middle atlantic bight shelfbreak front. *Journal of Geophysical Research: Oceans*, 121(8):6271–6294, 2016.

[55] Colette G Kerry, Brian S Powell, and Glenn S Carter. Effects of remote generation sites on model estimates of m2 internal tides in the philippine sea. *Journal of Physical Oceanography*, 43(1):187–204, 2013.

[56] S. Khatiwala. Generation of internal tides in an ocean of finite depth: analytical and numerical calculations. *Deep Sea Research Part I: Oceanographic Research Papers*, 50(1):3–21, 2003.

[57] Zhigang Lai, Changsheng Chen, Robert C. Beardsley, Brian Rothschild, and Rucheng Tian. Impact of high-frequency nonlinear internal waves on plankton dynamics in massachusetts bay. *Journal of Marine Research*, 68(2):259–281, 2010.

[58] Kevin G Lamb. Nonlinear interaction among internal wave beams generated by tidal flow over supercritical topography. *Geophysical Research Letters*, 31(9), 2004.

[59] Russell Lande and Charles S. Yentsch. Internal waves, primary production and the compensation depth of marine phytoplankton. *Journal of Plankton Research*, 10(3):565–571, 1988.

[60] William G Large, James C McWilliams, and Scott C Doney. Oceanic vertical mixing: A review and a model with a nonlocal boundary layer parameterization. *Reviews of geophysics*, 32(4):363–403, 1994.

[61] Sonya Legg and Karin MH Huijts. Preliminary simulations of internal waves and mixing generated by finite amplitude tidal flow over isolated topography. *Deep Sea Research Part II: Topical Studies in Oceanography*, 53(1-2):140–156, 2006.

[62] Steven J Lentz and David C Chapman. The importance of nonlinear cross-shelf momentum flux during wind-driven coastal upwelling. *Journal of Physical Oceanography*, 34(11):2444–2457, 2004.

[63] Steven J Lentz and Melanie R Fewings. The wind-and wave-driven inner-shelf circulation. *Annual review of marine science*, 4(1):317–343, 2012.

[64] Ricardo M. Letelier, David M. Karl, Mark R. Abbott, and Robert R. Bidigare.

Light driven seasonal patterns of chlorophyll and nitrate in the lower euphotic zone of the north pacific subtropical gyre. *Limnology and Oceanography*, 49(2):508–519, 2004.

[65] Zhiqiang Liu and Jianping Gan. Modeling study of variable upwelling circulation in the east china sea: Response to a coastal promontory. *Journal of Physical Oceanography*, 44(4):1078–1094, 2014.

[66] Z. Ljubešić, H. Mihanović, A. Matek, M. Mucko, E.P. Ashterberg, M. Omand, B. Pestorić, D. Lučić, H. Čižmek, B. Čolić, C. Balestra, R. Casotti, I. Janeković, and M. Orlić. Marine plankton community and net primary production responding to island-trapped waves in a stratified oligotrophic ecosystem. *Heliyon*, 2024.

[67] Stefan G. Llewellyn Smith and W. R. Young. Conversion of the Barotropic Tide. *Journal of Physical Oceanography*, 32(5):1554–1566, May 2002.

[68] Alan R Longhurst. *Ecological geography of the sea*. Elsevier, 2010.

[69] MS Longuet-Higgins. On the trapping of wave energy round islands. *Journal of Fluid Mechanics*, 29(4):781–821, 1967.

[70] MS Longuet-Higgins. On the trapping of long-period waves round islands. *Journal of Fluid Mechanics*, 37(4):773–784, 1969.

[71] Zhongming Lu and Jianping Gan. A modeling study of nutrient transport and dynamics over the northern slope of the south china sea. *Journal of Geophysical Research: Oceans*, 128(5):e2022JC019225, 2023.

[72] Andrew J. Lucas, Peter J. S. Franks, and Christopher L. Dupont. Horizontal internal-tide fluxes support elevated phytoplankton productivity over the inner continental shelf: Horizontal internal-tide fluxes. *Limnology and Oceanography: Fluids and Environments*, 1(1):56–74, 2011.

[73] J.J. MacIsaac and R.C. Dugdale. The kinetics of nitrate and ammonia uptake by natural populations of marine phytoplankton. *Deep Sea Research and Oceanographic Abstracts*, 16(1):45–57, 1969.

[74] JA MacKinnon, Matthew H Alford, Oliver Sun, Rob Pinkel, Zhongxiang Zhao, and Jody Klymak. Parametric subharmonic instability of the internal tide at 29 n. *Journal of Physical Oceanography*, 43(1):17–28, 2013.

[75] Joseph P. Martin, Daniel L. Rudnick, and Robert Pinkel. Spatially broad observations of internal waves in the upper ocean at the hawaiian ridge. *Journal of Physical Oceanography*, 36(6):1085–1103, 2006.

[76] Antonija Matek, Maja Mucko, Raffaella Casotti, Anna Chiara Trano, Eric P Achterberg, Hrvoje Mihanović, Hrvoje Čižmek, Barbara Čolić, Vlado Cuculić, and Zrinka Ljubešić. Phytoplankton diversity and co-dependency in a stratified oligotrophic ecosystem in the south adriatic sea. *Water*, 15(12):2299, 2023.

[77] MA Merrifield, L Yang, and DS Luther. Numerical simulations of a storm-generated island-trapped wave event at the hawaiian islands. *Journal of Geophysical Research: Oceans*, 107(C10):33–1, 2002.

[78] Mark A Merrifield and Peter E Holloway. Model estimates of m2 internal tide energetics at the hawaiian ridge. *Journal of Geophysical Research: Oceans*, 107(C8):5–1, 2002.

[79] Monique Messié and Francisco P Chavez. Seasonal regulation of primary production in eastern boundary upwelling systems. *Progress in Oceanography*, 134:1–18, 2015.

[80] Monique Messié, Jesus Ledesma, Dorota D Kolber, Reiko P Michisaki, David G Foley, and Francisco P Chavez. Potential new production estimates in four eastern boundary upwelling ecosystems. *Progress in Oceanography*, 83(1-4):151–158, 2009.

[81] Anthony F Michaels and Anthony H Knap. Overview of the us jgofs bermuda atlantic time-series study and the hydrostation s program. *Deep Sea Research Part II: Topical Studies in Oceanography*, 43(2-3):157–198, 1996.

[82] John F Middleton and David Ramsden. The evolution of the bottom boundary layer on the sloping continental shelf: A numerical study. *Journal of Geophysical Research: Oceans*, 101(C8):18061–18077, 1996.

[83] Hrvoje Mihanović, Mirko Orlić, and Zoran Pasarić. Diurnal thermocline oscillations driven by tidal flow around an island in the middle adriatic. *Journal of Marine Systems*, 78:S157–S168, 2009.

[84] Hrvoje Mihanović, Gordana Beg Paklar, and Mirko Orlić. Resonant excitation

of island-trapped waves in a shallow, seasonally stratified sea. *Continental Shelf Research*, 77:24–37, 2014.

[85] S Muacho, JCB Da Silva, V Brotas, and PB Oliveira. Effect of internal waves on near-surface chlorophyll concentration and primary production in the nazaré canyon (west of the iberian peninsula). *Deep Sea Research Part I: Oceanographic Research Papers*, 81:89–96, 2013.

[86] Peter Müller, Greg Holloway, Frank Henyey, and Neil Pomphrey. Nonlinear interactions among internal gravity waves. *Reviews of Geophysics*, 24(3):493–536, 1986.

[87] Jonathan D Nash, Samuel M Kelly, Emily L Shroyer, James N Moum, and Timothy F Duda. The unpredictable nature of internal tides on continental shelves. *Journal of Physical Oceanography*, 42(11):1981–2000, 2012.

[88] Mirko Orlić, Gordana Beg Paklar, Vlado Dadić, Nenad Leder, Hrvoje Mihanović, Miroslava Pasarić, and Zoran Pasarić. Diurnal upwelling resonantly driven by sea breezes around an adriatic island. *Journal of Geophysical Research: Oceans*, 116(C9), 2011.

[89] Judit Padisák, Eva Hajnal, Luigi Naselli-Flores, Martin T Dokulil, Peeter Noges, and Tamar Zohary. Convergence and divergence in organization of phytoplankton communities under various regimes of physical and biological control. *Hydrobiologia*, 639:205–220, 2010.

[90] A Pichon, Y Morel, R Baraille, and LS Quaresma. Internal tide interactions in the bay of biscay: Observations and modelling. *Journal of Marine Systems*, 109:S26–S44, 2013.

[91] Oscar Pizarro and Gary Shaffer. Wind-driven, coastal-trapped waves off the island of gotland, baltic sea. *Journal of physical oceanography*, 28(11):2117–2129, 1998.

[92] B. S. Powell, I. Janeković, G. S. Carter, and M. A. Merrifield. Sensitivity of internal tide generation in hawaii. *Geophysical Research Letters*, 39(10), 2012.

[93] James M Pringle. Enhancement of wind-driven upwelling and downwelling by alongshore bathymetric variability. *Journal of Physical Oceanography*, 32(11):3101–3112, 2002.

[94] SJ Prinsenberg, WL Wilmot, and Maurice Rattray Jr. Generation and dissipation of coastal internal tides. In *Deep Sea Research and Oceanographic Abstracts*, volume 21, pages 263–281. Elsevier, 1974.

[95] François Pétrélis, Stefan Llewellyn Smith, and W. R. Young. Tidal conversion at a submarine ridge. *Journal of Physical Oceanography*, 36(6):1053–1071, 2006.

[96] Luc Rainville, TM Shaun Johnston, Glenn S Carter, Mark A Merrifield, Robert Pinkel, Peter F Worcester, and Brian D Dushaw. Interference pattern and propagation of the m2 internal tide south of the hawaiian ridge. *Journal of physical oceanography*, 40(2):311–325, 2010.

[97] Luc Rainville and Robert Pinkel. Baroclinic energy flux at the hawaiian ridge:

Observations from the R/P FLIP. *Journal of Physical Oceanography*, 36(6):1104–1122, 2006.

[98] Richard D Ray and Gary T Mitchum. Surface manifestation of internal tides generated near hawaii. *Geophysical Research Letters*, 23(16):2101–2104, 1996.

[99] Robert O Reid. Effect of coriolis force on edge waves (i) investigation of the normal modes. *Journal of Marine Research*, 16(2):109–144, 1958.

[100] Katherine Richardson and Jørgen Bendtsen. Distinct seasonal primary production patterns in the sub-polar gyre and surrounding seas. *Frontiers in Marine Science*, 8:785685, 2021.

[101] D. L. Rudnick. From tides to mixing along the hawaiian ridge. *Science*, 301(5631):355–357, 2003.

[102] Jonathan Sharples, C. Mark Moore, Anna E. Hickman, Patrick M. Holligan, Jacqueline F. Tweddle, Matthew R. Palmer, and John H. Simpson. Internal tidal mixing as a control on continental margin ecosystems. *Geophysical Research Letters*, 36(23):L23603, 2009.

[103] Jonathan Sharples, Jacqueline F. Tweddle, J. A. Mattias Green, Matthew R. Palmer, Young-Nam Kim, Anna E. Hickman, Patrick M. Holligan, C. Mark Moore, Tom P. Rippeth, John H. Simpson, and Vladimir Krivtsov. Spring-neap modulation of internal tide mixing and vertical nitrate fluxes at a shelf edge in summer. *Limnology and Oceanography*, 52(5):1735–1747, 2007.

[104] Alexander F Shchepetkin and James C McWilliams. Quasi-monotone advection schemes based on explicit locally adaptive dissipation. *Monthly weather review*, 126(6):1541–1580, 1998.

[105] Alexander F. Shchepetkin and James C. McWilliams. A method for computing horizontal pressure-gradient force in an oceanic model with a nonaligned vertical coordinate. *Journal of Geophysical Research*, 108(C3):3090, 2003.

[106] Alexander F. Shchepetkin and James C. McWilliams. The regional oceanic modeling system (ROMS): a split-explicit, free-surface, topography-following-coordinate oceanic model. *Ocean Modelling*, 9(4):347–404, 2005.

[107] DA Siegel, SC Doney, and JA Yoder. The north atlantic spring phytoplankton bloom and sverdrup's critical depth hypothesis. *science*, 296(5568):730–733, 2002.

[108] Harper L Simmons, Robert W Hallberg, and Brian K Arbic. Internal wave generation in a global baroclinic tide model. *Deep Sea Research Part II: Topical Studies in Oceanography*, 51(25-26):3043–3068, 2004.

[109] Louis St. Laurent, Steven Stringer, Chris Garrett, and Dominique Perrault-Joncas. The generation of internal tides at abrupt topography. *Deep Sea Research Part I: Oceanographic Research Papers*, 50(8):987–1003, 2003.

[110] Craig L. Stevens, Philip J. H. Sutton, and Cliff S. Law N. Internal waves downstream of norfolk ridge, western pacific, and their biophysical implications. *Limnology and Oceanography*, 57(4):897–911, July 2012.

[111] Suzanne L. Strom, Erin L. Macri, and M. Brady Olson. Microzooplankton grazing in the coastal gulf of alaska: Variations in top-down control of phytoplankton. *Limnology and Oceanography*, 52(4):1480–1494, July 2007.

[112] Suzanne L. Strom, Mb Olson, El Macri, and Cw Mord. Cross-shelf gradients in phytoplankton community structure, nutrient utilization, and growth rate in the coastal gulf of alaska. *Marine Ecology Progress Series*, 328:75–92, 2006.

[113] Harald U Sverdrup. On conditions for the vernal blooming of phytoplankton. *J. Cons. Int. Explor. Mer*, 18(3):287–295, 1953.

[114] José C. Sánchez-Garrido, C. Naranjo, D. Macías, J. García-Lafuente, and T. Oguz. Modeling the impact of tidal flows on the biological productivity of the A lboran S ea. *Journal of Geophysical Research: Oceans*, 120(11):7329–7345, 2015.

[115] Darcy AA Taniguchi, Peter JS Franks, and Francis J Poulin. Planktonic biomass size spectra: an emergent property of size-dependent physiological rates, food web dynamics, and nutrient regimes. *Marine Ecology Progress Series*, 514:13–33, 2014.

[116] Robyn E. Tuerena, Richard G. Williams, Claire Mahaffey, Clément Vic, J. A. Mattias Green, Alberto Naveira-Garabato, Alexander Forryan, and Jonathan Sharples. Internal tides drive nutrient fluxes into the deep chlorophyll maximum over mid-ocean ridges. *Global Biogeochemical Cycles*, 33(8):995–1009, 2019.

[117] Marina Villamaña, Beatriz Mouriño-Carballido, Emilio Marañón, Pedro Cermeño, Paloma Chouciño, José C. B. da Silva, Patricio A. Díaz, Bieito Fernández-Castro, Miguel Gilcoto, Rocío Graña, Mikel Latasa, Jorge M. Magalhaes, José Luis Otero-Ferrer, Beatriz Reguera, and Renate Scharek. Role of internal waves on mixing, nutrient supply and phytoplankton community structure during spring and neap tides in the upwelling ecosystem of ría de vigo (nw iberian peninsula): Role of internal waves in the ría de vigo. *Limnology and Oceanography*, 62(3):1014–1030, 2017.

[118] John C Warner, Christopher R Sherwood, Hernan G Arango, and Richard P Signell. Performance of four turbulence closure models implemented using a generic length scale method. *Ocean Modelling*, 8(1-2):81–113, 2005.

[119] Amy F Waterhouse, Samuel M Kelly, Zhongxiang Zhao, Jennifer A MacKinnon, Jonathan D Nash, Harper Simmons, Dmitry Brahznikov, Luc Rainville, Matthew Alford, and Rob Pinkel. Observations of the tasman sea internal tide beam. *Journal of Physical Oceanography*, 48(6):1283–1297, 2018.

[120] Elle Weeks, Martin Losch, and Eli Tziperman. The upwelling source depth distribution and its response to wind stress and stratification. *Journal of Physical Oceanography*, 54(4):1003–1018, 2024.

[121] C.B. Woodson. The fate and impact of internal waves in nearshore ecosystems. *Annual Review of Marine Science*, 10(1):421–441, 2018.

[122] Hui Wu and Jianrong Zhu. Advection scheme with 3rd high-order spatial interpolation at the middle temporal level and its application to saltwater intrusion in the changjiang estuary. *Ocean Modelling*, 33(1-2):33–51, 2010.

[123] Carl Wunsch. The spectrum from two years to two minutes of temperature fluctuations in the main thermocline at bermuda. In *Deep Sea Research and Oceanographic Abstracts*, volume 19, pages 577–593. Elsevier, 1972.

[124] Changjin Zhao, Ute Daewel, and Corinna Schrum. Tidal impacts on primary production in the north sea. *Earth System Dynamics*, 10(2):287–317, 2019.